

Advances in Meteorology

Land-Atmosphere Interactions

Guest Editors: Marcos Heil Costa, Michael T. Coe, and David R. Galbraith



Land-Atmosphere Interactions

Advances in Meteorology

Land-Atmosphere Interactions

Guest Editors: Marcos Heil Costa, Michael T. Coe,
and David R. Galbraith



Copyright © 2016 Hindawi Publishing Corporation. All rights reserved.

This is a special issue published in "Advances in Meteorology." All articles are open access articles distributed under the Creative Commons Attribution License, which permits unrestricted use, distribution, and reproduction in any medium, provided the original work is properly cited.

Editorial Board

José Antonio Adame, Spain
Cesar Azorin-Molina, Spain
Guillermo Baigorria, USA
Marina Baldi, Italy
Abderrahim Bentamy, France
Massimo A. Bollasina, UK
Stefania Bonafoni, Italy
Isabella Bordi, Italy
Alex Cannon, Canada
Claudio Carbone, Italy
Dominique Carrer, France
Charles Chemel, UK
Annalisa Cherchi, Italy
James Cleverly, Australia
Jill S. M. Coleman, USA
Gabriele Curci, Italy
Mladjen Ćurić, Serbia
Maher A. Dayeh, USA
Klaus Dethloff, Germany
Panuganti C. S. Devara, India
Julio Diaz, Spain
Arona Diedhiou, France
Stefano Dietrich, Italy
E. Domínguez Vilches, Spain
Antonio Donateo, Italy
Igor Esau, Norway
Stefano Federico, Italy
Enrico Ferrero, Italy
Rossella Ferretti, Italy
Roberto Fraile, Spain
Charmaine Franklin, Australia
Jan Friesen, Germany

Maria Ángeles García, Spain
Herminia García Mozo, Spain
Eduardo García-Ortega, Spain
Luis Gimeno, Spain
Jorge E. Gonzalez, USA
Ismail Gultepe, Canada
Rafiq Hamdi, Belgium
Adel Hanna, USA
Hiroyuki Hashiguchi, Japan
Tareq Hussein, Jordan
Bradley G. Illston, USA
Ivar S A Isaksen, Norway
Yasunobu Iwasaka, Japan
Pedro Jiménez-Guerrero, Spain
Kuruvilla John, USA
Charles Jones, USA
Hann-Ming H. Juang, USA
George Kallos, Greece
Harry D. Kambezidis, Greece
Nir Y. Krakauer, USA
Simon O. Krichak, Israel
Hisayuki Kubota, Japan
Haim Kutiel, Israel
Richard Leaitch, Canada
Monique Leclerc, USA
Ilan Levy, Israel
Gwo-Fong Lin, Taiwan
Anthony R. Lupo, USA
Paolo Madonia, Italy
Andreas Matzarakis, Germany
Samantha Melani, Italy
Nicholas Meskhidze, USA

Christophe Messenger, France
Mario M. Miglietta, Italy
Takashi Mochizuki, Japan
Goro Mouri, Japan
Brian R. Nelson, USA
Efthymios Nikolopoulos, USA
Sandip Pal, USA
Giulia Panegrossi, Italy
Giulia Pavese, Italy
Kyaw T. Paw, USA
Olivier P. Prat, USA
Sara C. Pryor, USA
Philippe Ricaud, France
Tomeu Rigo, Spain
Filomena Romano, Italy
Jose Antonio Ruiz-Arias, Spain
Haydee Salmun, USA
Pedro Salvador, Spain
Arturo Sanchez-Lorenzo, Spain
Andres Schmidt, USA
Shraddhanand Shukla, USA
Fiona Smith, UK
Francisco J. Tapiador, Spain
Yoshihiro Tomikawa, Japan
Tomoo Ushio, Japan
R. Van Der Velde, Netherlands
Sergio Vicente-Serrano, Spain
Francesco Viola, Italy
Alastair Williams, Australia
Olga Zolina, France

Contents

Land-Atmosphere Interactions

Marcos Heil Costa, Michael T. Coe, and David R. Galbraith
Volume 2016, Article ID 2362398, 1 page

Spatial and Temporal Soil Moisture Variations over China from Simulations and Observations

Xin Lai, Jun Wen, Sixian Cen, Xi Huang, Hui Tian, and Xiaokang Shi
Volume 2016, Article ID 4587687, 14 pages

A Critical Evaluation of the Nonparametric Approach to Estimate Terrestrial Evaporation

Yongmin Yang, Hongbo Su, and Jianwei Qi
Volume 2016, Article ID 5343718, 10 pages

A Comparison of Three Gap Filling Techniques for Eddy Covariance Net Carbon Fluxes in Short Vegetation Ecosystems

Xiaosong Zhao and Yao Huang
Volume 2015, Article ID 260580, 12 pages

Flooding Regime Impacts on Radiation, Evapotranspiration, and Latent Energy Fluxes over Groundwater-Dependent Riparian Cottonwood and Saltcedar Forests

James Cleverly, James R. Thibault, Stephen B. Teet, Paul Tashjian, Lawrence E. Hipps, Clifford N. Dahm, and Derek Eamus
Volume 2015, Article ID 935060, 14 pages

The Effects of Climate Change on Variability of the Growing Seasons in the Elbe River Lowland, Czech Republic

Vera Potopová, Pavel Zahradníček, Luboš Türkott, Petr Štěpánek, and Josef Soukup
Volume 2015, Article ID 546920, 16 pages

Editorial

Land-Atmosphere Interactions

Marcos Heil Costa,¹ Michael T. Coe,² and David R. Galbraith³

¹*Federal University of Viçosa, 36570-000 Viçosa, MG, Brazil*

²*Woods Hole Research Center, Falmouth, MA 02540-1644, USA*

³*University of Leeds, Leeds LS2 9JT, UK*

Correspondence should be addressed to Marcos Heil Costa; mhcosta@ufv.br

Received 1 October 2015; Accepted 12 October 2015

Copyright © 2016 Marcos Heil Costa et al. This is an open access article distributed under the Creative Commons Attribution License, which permits unrestricted use, distribution, and reproduction in any medium, provided the original work is properly cited.

The bidirectional interactions between the land surface and the atmosphere play important roles in determining weather and climate across multiple time scales. The influence of soil moisture on short-term weather forecasts, the role of phenology and surface radiation balance in seasonal and intraseasonal climate variability, the interaction of land cover and long-term mean climate in several regions of the world, and the emissions of greenhouse gases due to changes in land cover or agricultural practices are well-known examples of these interactions.

This special issue deals with different aspects of the interactions between land and atmosphere, using observations and modeling.

Y. Yang et al. provide a critical evaluation of the nonparametric approach to estimate terrestrial evapotranspiration, one of the most challenging problems for hydrometeorologists. They concluded that the nonparametric approach is very close to the equilibrium evaporation equation under wet conditions and that its applications in dry conditions should be avoided.

Missing data is an inevitable problem when measuring CO₂, water, and energy fluxes between biosphere and atmosphere with eddy covariance systems. X. Zhao and Y. Huang (this issue) compared three gap-filling methods for eddy covariance net carbon fluxes in three short vegetation sites. They found that the performance of the filling techniques depended on the time scale, gap length, and time of day (day or night), concluding that a combination of the available methods reduced cumulative bias and deviation for gap-filled net ecosystem exchange fluxes.

J. Cleverly et al. used ten years of eddy covariance measurements to evaluate the role of drought and flooding on radiation, evapotranspiration, and latent heat fluxes over groundwater-dependent riparian forests. A very interesting result is that, during flooding periods, annual values of evapotranspiration exceed annual precipitation by 250–600%, whereas it is greatly reduced during periods of severe drought.

Finally, two papers presented results from a combination of modeling and observations. V. Potopová et al. discussed the effects of climate change on the duration of the agricultural growing season in the Elbe River lowland, Czech Republic, during the 21st Century, while X. Lai et al. compared soil moisture variations over China from simulations with the Community Climate Model 4.0 with observations from a microwave multisatellite soil moisture dataset.

*Marcos Heil Costa
Michael T. Coe
David R. Galbraith*

Research Article

Spatial and Temporal Soil Moisture Variations over China from Simulations and Observations

Xin Lai,^{1,2} Jun Wen,² Sixian Cen,³ Xi Huang,⁴ Hui Tian,² and Xiaokang Shi⁵

¹College of Atmospheric Sciences, Plateau Atmosphere and Environment Key Laboratory of Sichuan Province, Chengdu University of Information Technology, Chengdu, Sichuan 610225, China

²Key Laboratory of Land Surface Process and Climate Change in Cold and Arid Regions, Cold and Arid Regions Environmental and Engineering Research Institute, Chinese Academy of Sciences, Lanzhou, Gansu 730000, China

³Chengdu Institute of Plateau Meteorology, China Meteorology Administration, Chengdu, Sichuan 610071, China

⁴Lijiang Airport Meteorological Station, Lijiang, Yunnan 674100, China

⁵Institute of Aeronautical Meteorology and Chemical Deference, Air Force Academy of Equipment, Beijing 100085, China

Correspondence should be addressed to Jun Wen; jwen@lzb.ac.cn

Received 16 November 2014; Revised 25 May 2015; Accepted 26 May 2015

Academic Editor: Eduardo García-Ortega

Copyright © 2016 Xin Lai et al. This is an open access article distributed under the Creative Commons Attribution License, which permits unrestricted use, distribution, and reproduction in any medium, provided the original work is properly cited.

The Community Land Model version 4.0 (CLM4.0) driven by the forcing data of Princeton University was used to simulate soil moisture (SM) from 1961 to 2010 over China. The simulated SM was compared to the in situ SM measurements from International Soil Moisture Network over China, National Centers for Environmental Prediction (NCEP) Reanalysis data, a new microwave based multiple-satellite surface SM dataset (SM-MW), and European Centre for Medium-Range Weather Forecasts Interim Reanalysis (ERA Interim/Land) SM data. The results showed that CLM4.0 simulation is capable of capturing characteristics of the spatial and temporal variations of SM. The simulated, NCEP, SM-MW, and ERA Interim/Land SM products are reasonably consistent with each other; based on the simulated SM of summer, it can be concluded that the spatial distribution in every layer was characterized by a gradually increasing pattern from the northwest to southeast. The SM increased from surface layer to deeper layer in general. The variation trends basically showed consistencies at all depths. The simulated SM of summer demonstrated different responses to the precipitation variation. The variation distribution of SM and measured precipitation had consistencies. The humid region significantly responded to precipitation, while the semiarid and arid regions were ranked second.

1. Introduction

Soil moisture (SM) is one of the most important geophysical variables for characterizing the status of the land surface, and it is also an important variable that controls the land-atmosphere interaction. By altering underlying surface variables like soil albedo and soil thermal capacity, changes in SM control the partition of net radiation to sensible heat and latent heat, leading to changes in the water and thermal balances between the lower atmosphere and the land surface. These changes in SM then influence regional climate change [1]. SM spatial and temporal distribution and variations have not only important weather and climate theoretical

importance, but also practical importance in the research fields of agriculture, ecology, and economy.

Despite the greater focus being directed to the effects of SM on weather forecasts and climate predictions, the lack of observations with long temporal continuity and high spatial resolution hinders the research on SM characteristics and climatic effects [2]. There are few SM datasets available in the International Soil Moisture Network at present [3–5]. Although the simulation ability of land surface model (LSM) suffers from gaps and uncertainties in forcing data and from model assumptions and generalizations, SM obtained through LSM simulation has good temporal frequency and spatial distribution. Land model especially has very good

physical conception of moisture transport, so it is widely used in research of surface variables like SM [1, 6–9].

Qian et al. [10] evaluated historical simulations of Community Land Model version 3.0 (CLM3) using available observations of SM. The results showed that observed SM variations over Illinois (USA) and parts of Eurasia are generally simulated well, with the dominant influence coming from precipitation. By running the Community Land Model (CLM3.5) over China from 1993 to 2002 using the reanalysis-based precipitation and air temperature and in situ observations in the meteorological forcing dataset, Wang and Zeng [6] discussed the effects of the quality of meteorological forcing data (such as precipitation and temperature) on the simulations of variables in the land surface water cycle. Compared to the in situ measured SM data, the CLM3.5 simulation can generally capture the spatial and seasonal variations of SM but overestimate SM in northeast and east China and underestimate SM in northwest China. Li et al. [1] generated an atmospheric field (ObsFC) for the Community Land Model version 3.5 (CLM3.5) with the support from ground station observations, and SM was simulated over China from 1951 to 2008. The resulting SM indicated that CLM3.5/ObsFC is capable of reproducing the spatial-temporal characteristics and long-term variation trends of SM over China. Using an in situ observation-based forcing field improves the simulation of SM. Guo et al. [11] applied the Variable Infiltration Capacity (VIC) distributed hydrological model [12] with $9 \times 9 \text{ km}^2$ grid resolution and calibrated in the Hanjiang basin. Validation results show that the VIC model can simulate runoff hydrograph with high model efficiency and low relative error. Decharme et al. [13] study the evaluation of a new land surface hydrology within the Noah-WRF land-atmosphere-coupled mesoscale model over the Sahel. An appreciable improvement of the model results is found when the new hydrology is used. The ECMWF Interim Reanalysis (ERA-Interim) [14] and the National Aeronautics and Space Administration (NASA) Modern-Era Retrospective Analysis for Research and Applications (MERRA) [15] provide global reanalyses for the past three decades (from 1979 onward) at high spatial resolution and with modern data assimilation and modeling systems. ECMWF recently developed ERA-Interim/Land simulations, where the ERA-Interim near-surface meteorological forcing is used with the latest version of the ECMWF land surface model [7]. An enhanced MERRA data product, MERRA-Land, has recently been released [9]. Albergel et al. [16, 17] evaluate reanalyses SM products from ERA-Interim, ERA-Interim/Land, and MERRA-Land with global ground-based in situ observations. The three analyses show good skills in capturing surface SM variability.

Besides using modeling approaches, global SM can be estimated through active and passive satellite microwave remote sensing with adequate spatial-temporal resolution and accuracy. Several quasiglobal SM datasets have been generated during the last decade based on either active or passive microwave satellite observations from Advanced Microwave Scanning Radiometer-EOS (AMSR-E) [18, 19], European Remote Sensing Satellite (ERS-1 and ERS-2),

MetOp Advanced Scatterometer (ASCAT) [20], Scanning Multichannel Microwave Radiometer (SMMR), Special Sensor Microwave Imager (SSM/I), Tropical Rainfall Measuring Mission (TRMM) Microwave Imager (TMI), WindSat [21, 22], and Soil Moisture and Ocean Salinity mission (SMOS) [23, 24]. The combination/ensemble of these sensors opens up the possibility of studying the global behavior of SM from 1979 onward using only observations [25]. Recently, the first multidecadal satellite-based global SM record has been available [26]. The new consistent global SM data record based on active and passive microwave sensors (SM-MW) has been generated by homogenizing different existing SM products [26–28].

The above research showed that the LSM can reasonably reflect the temporal and spatial distribution of surface variables like SM and soil temperature. As the limitation of available observation datasets, the previous investigations of CLM based on the observation have focused on a single site or small scale, and the simulating period is short. So it is difficult to fully reflect the ability of CLM simulation, and the SM datasets of CLM simulation could not be used in the research of regional SM climatology under the background of climate change. Furthermore, the researches on discussing the response of SM to climate change over China are not well presented. As one of the well-developed land models in the world, the newly released CLM4.0 improves the hydrology scheme of CLM3.5 and depicts the SM dynamic scheme more accurate, it is potential in SM simulation at a continental scale.

In this paper, the CLM4.0 driven by the atmospheric forcing data of Princeton University was deployed to simulate SM spatial distribution and temporal spatial variation from 1961 to 2010 over China. The simulated SM was compared to the ground observations, NCEP Reanalysis data, and SM-MW and ERA Interim/Land SM data. It is expected that all these aspects will provide a full realization of CLM simulation ability over China. Furthermore, the spatial and temporal variations of SM and its response to climate change over China during 1961–2010 will be explored, the shortage of CLM4.0 simulation over China will be summarized and discussed, and the future improvements of the scheme will be prospected.

2. Model and Data

2.1. Introduction of CLM4.0. Community land model (CLM) is one of the most well-developed land surface process models and has the biggest potential development in the world [29]. It integrates advantages of the relative mature process description of Biosphere-Atmosphere Transfer Scheme (BATS), LSM which was established at the Institute of Atmospheric Physics, Chinese Academy of Sciences in 1994 (IAP94), LSM of NCAR, and so forth. It also includes hydrology scheme and parameterization of physical scheme. The CLM is the land model of the Community Earth System Model (CESM) and Community Atmosphere Model (CAM), coupled with many climate models. The model represents several aspects of the land surface including surface heterogeneity and consists of

components or submodels related to land biogeophysics, the hydrologic cycle, biogeochemistry, human dimensions, and ecosystem dynamics. Excessively wet and less variation in SM simulations were recognized as a deficiency of CLM3.5 [30, 31]. The newly released CLM4.0 improved the hydrology scheme of CLM3.5, adopted a modified resolution of the Richards equation, and improved the definition of the lower boundary condition to directly couple the soil water and ground water [31, 32]; CLM4.0 revised soil evaporation parameterization, accounting for the effects of canopy litter and within canopy stability on evaporation [33]. The snow module was significantly improved in CLM4.0 [34–36]. The soil column has been extended to 50 m depth by adding five additional hydrological inactive soil layers [37]. An urban module has been added [38]. The albedo biases were reduced by improving dynamic vegetation functions and patterns [39, 40]. By all above measures, CLM4.0 improved soil water dynamic process in CLM3.5 and leads to reducing the simulated SM and enlarging SM variability. The snow coverage simulated by revised model increased, soil temperatures decreased in organic-rich soils, albedo over the forests and grasslands decreased, and albedo during the transition-season over the snow covered regions increased, all of which are improvements compared to CLM3.5. So, CLM4.0 is selected for this research.

2.2. Data Description

2.2.1. Forcing Data and Land Surface Data in CLM4.0. CLM4.0 was driven by the atmospheric forcing data of Princeton University from 1961 to 2010, with temporal resolution of 3 hours and horizontal resolution of $1^\circ \times 1^\circ$ degrees [41]. The forcing data includes 7 meteorological variables: precipitation, air temperature at 2 m above ground, downward short- and long-wave radiation at surface, surface pressure, specific humidity, and wind speed. The original forcing data is a global, from 1948 to 2010 dataset of meteorological forcing that can be used to drive models of land surface hydrology. The forcing data is a hybrid of data from the NCEP-National Center for Atmospheric Research (NCAR) reanalysis [42] and a suite of global observation based datasets of precipitation, temperature, and radiation. The observation based datasets include Climatic Research Unit (CRU) monthly climate variables, Global Precipitation Climatology Project (GPCP) daily precipitation, TRMM 3-hourly precipitation, and the National Aeronautics and Space Administration (NASA) Langley monthly surface radiation budget. More details of the dataset are described in [41]. The dataset has been used to evaluate the global terrestrial water budget [43] and also to drive the VIC model for exploring global drought characteristics [44]. The land surface datasets released with CLM4.0 were used in this study, which includes topography, soil properties, plant functional types, and land use.

2.2.2. In Situ Measured SM. 30 stations selected from International Soil Moisture Network over China are used to validate CLM4.0 simulation [3–5]. Li et al. [45] used these datasets to

verify the ECMWF 40-year Reanalysis (ERA-40) and NCEP Reanalysis data of SM. The datasets were successfully used to verify and explore models [46]. The datasets were converted into volumetric SM and can be conveniently used to evaluate and improve simulations.

2.2.3. NCEP Reanalysis Data. The NCEP Climate Forecast System Reanalysis (CFSR) was completed over the 31-year period of 1979 to 2009 in January 2010. The CFSR was designed and executed as a global, high resolution, coupled atmosphere-ocean-land surface-sea ice system to provide the best estimate of the state of these coupled domains over this period. The CFSR includes (1) coupling of atmosphere and ocean, (2) an interactive sea-ice model, and (3) assimilation of satellite radiances by the gridpoint statistical interpolation scheme over the entire period. The global land surface model has 4 soil levels. Most available in situ and satellite observations were included in the CFSR. Satellite observations were used in radiance form [47]. CFSR land surface output products will serve many purposes, including providing estimates and diagnoses of the earth's climate state, over the satellite data period, for community climate research [47]. The data is distributed via <http://rda.ucar.edu/datasets/ds093.2/>. In this study, surface SM from CFSR is from the first soil layer (0–10 cm) and has a spatial resolution of 0.5° . The SM data are provided in volumetric units (m^3/m^3).

2.2.4. Remotely Sensed Data. In response to the Global Climate Observing System (GCOS) endorsement of SM as an Essential Climate Variable (ECV), the European Space Agency (ESA) Water Cycle Multi-Mission Observation Strategy (WACMOS) project and Climate Change Initiative (CCI, <http://www.esa-soilmoisture-cci.org/>) have supported the generation of a SM product based on multiple microwave sources. The first version of the combined product, SM-MW, was released in June 2012 by the Vienna University of Technology. The merged product is the output of blending the active and passive SM products, which are derived from SMMR, SSM/I, TMI, and AMSR-E for the passive datasets and Active Microwave Instrument-Windscat (AMIWS) and MetOp (ASCAT) for the active datasets. This data has been produced following the method described by [26–28]. The homogenized and merged product presents surface SM with a global coverage and a spatial resolution of 0.25° , and the temporal resolution is 1 day with its reference time at 0:00 UTC. The SM data are provided in volumetric units (m^3/m^3). SM-MW was used to evaluate SM products [17, 48].

2.2.5. ERA Interim/Land Reanalysis. ERA-Interim/Land is a global land surface reanalysis dataset covering the period 1979–2010. It describes the evolution of SM, soil temperature, and snowpack. ERA-Interim/Land is the result of a single 32-year simulation with the latest ECMWF land surface model driven by meteorological forcing from the ERA-Interim atmospheric reanalysis. The horizontal resolution is about 80 km and the time frequency is 3 hours. ERA-Interim/Land includes a number of parameterization improvements in

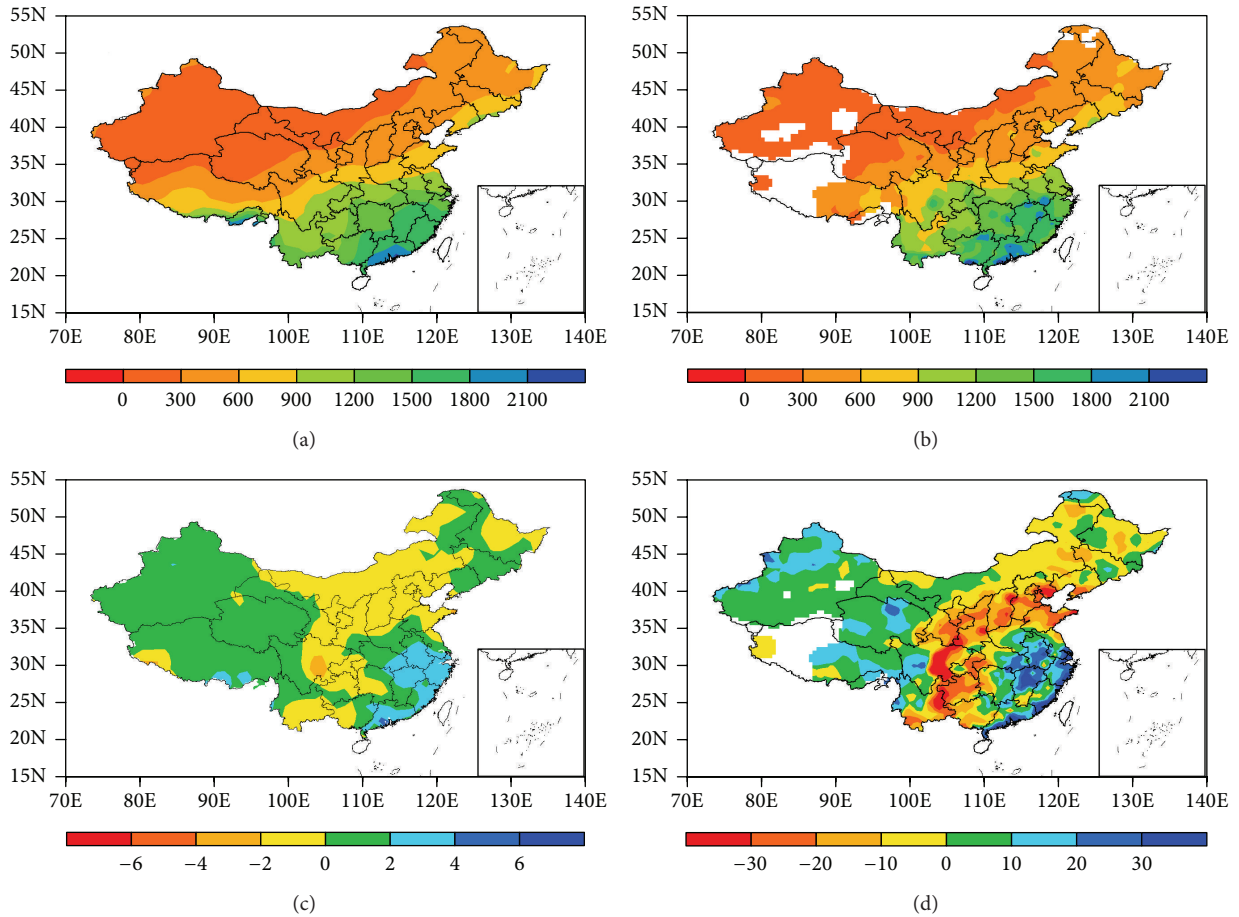


FIGURE 1: The intercomparison between Princeton precipitation and measured precipitation of 1961–2010. (a) Princeton annual mean precipitation (unit: mm); (b) ground measured annual mean precipitation (unit: mm); (c) Princeton annual precipitation variation linear trend (unit: mm/10 a); and (d) ground measured annual precipitation variation linear trend (unit: mm/10 a).

the land surface scheme with respect to the original ERA-Interim dataset, which makes it more suitable for climate studies involving land water resources. The quality of ERA-Interim/Land is assessed by comparing with ground-based and remote sensing observations [7]. The SM data of ERA-Land product was used to analyze the skill and global trend of SM [17]. In this study, surface SM from ERA Interim/Land is from the first soil layer (0–7 cm).

3. Validation of Simulations

The simulation region of this study is domain of 70°–135°E, 15°–55°N. To stabilize the hydrology process and spin-up CLM model, CLM4.0 was firstly run twice for 1961–2010 simulation years with Princeton forcing data, and, consequently, the simulations of soil water variables were output at a time scale of 1961 to 2010 and horizontal resolution of $0.5^\circ \times 0.5^\circ$. Firstly, the Princeton forcing data was verified with measured data, and then the simulated SM was compared to the ground observations, NCEP Reanalysis data, and SM-MW and ERA Interim/Land SM data.

3.1. Validation of Forcing Data. Precipitation and temperature are two important variables which influence SM variation. In this paper, precipitation and temperature in Princeton forcing data were validated with ground measured data. The ground measured data is downloaded from China Meteorological Data Sharing Service System of China Meteorological Administration (CMA). Not all stations have long enough time series for climate studies. After screening out unqualified stations, 584 stations for precipitation and 599 stations for temperature from 1961 to 2010 were selected for this study. The precipitation and temperature data were recorded one or several times per day, and they were all converted to daily data. It is to be seen from Figure 1 that Princeton precipitation basically reflects spatial distribution of ground measured precipitation, and precipitation decreased from northwest to southeast. Princeton precipitation also basically reflects spatial distribution of ground measured precipitation variation trends. Precipitation decreased in north of northeast, north China, Inner Mongolia, and parts of the southwest, while precipitation increased in the southeast and south China. But compared to measured precipitation, the absolute value of Princeton precipitation linear trends was small.

From the results of intercomparison between Princeton and ground measured data, it is concluded that the Princeton precipitation and temperature basically reflect spatial distribution and variation trends of measured data. As a result it could be used to drive CLM4.0 to simulate SM over China.

3.2. Comparison of Spatial Distribution between Simulated and Measured SM. The spatial distributions of the simulated and measured SM for April to November were compared because the observations were suspended during frozen period. The spatial distributions of simulated and measured SM were basically consistent with each other as shown in Figure 2. The humid regions were located over the northeast China and Jianghuai basin, and the SM was around 0.25 in the northeast China. Dry region was located over Hetao region, and SM was around 0.15 (Figure 2(b)). The simulated SM reasonably reflected spatial distribution characteristics of measured SM. The spatial distribution of the simulated SM was characterized by a gradually increasing pattern from the northwest to southeast. The spatial pattern of measured SM at 0–50 cm depth was basically consistent with 0–10 cm depth (Figure 2(d)). The measured SM in most stations over northeast China was larger than that at 0–10 cm depth. This result implied that SM in most stations over northeast China increased from shallow depth (0–10 cm) to deep depth (0–50 cm). The spatial distributions of simulated SM in 0–50 cm depth (Figure 2(c)) and measured SM were basically consistent with each other. Simulated SM in 0–50 cm depth is larger than 0–10 cm depth over northwestern, southern area of Yangtze River, and partial areas of southwest China. The spatial distributions of the simulated SM by CLM4.0 were generally consistent with the results of previous studies in China [1]. But the simulated SM was systematically larger than measured SM at two depths. The bias percent (Figures 2(e) and 2(f)) showed that simulated SM was larger than the measured SM at 0–10 cm layer in most stations throughout China. The simulated SM was larger than the measured SM by 60% over Hetao region. Simulated SM was larger than the measured SM in most stations at 0–50 cm layer. Simulated SM was larger than the measured SM in most stations over northeast China. But the stations where simulated SM was larger than measured SM decreased, and bias decreased in most stations. The reason is that measured SM in most stations over northeast China increased from shallow depth (0–10 cm) to deep depth (0–50 cm), simulated SM did not have obvious variations, and bias decreased in most stations.

3.3. Comparison of Temporal Variation between Simulated and Measured SM. Figure 3 showed the linear trends (linear regression coefficient) and bias percent (the percent of bias and in situ, and bias is simulations minus in situ) of simulated SM and measured SM at two different layers (0–10 cm, 0–50 cm) during 1981–1999. The variation trends of measured SM (Figures 3(b) and 3(d)) showed that measured SM mainly decreased in northeast China and Hetao region. Simulated SM (Figures 3(a) and 3(c)) basically reflected variation trends of measured SM. The simulated SM decreased in

TABLE 1: The correlation coefficients between simulated monthly mean and measured SM of each layer over the subregions.

Regions	0–10 cm	10–20 cm	20–30 cm	30–50 cm	0–50 cm
R1	0.18*	-0.09	-0.26	-0.34	-0.2
R2	0.43**	0.35**	0.34**	0.3**	0.35**
R3	0.23**	0.23**	0.29**	0.32**	0.3**

*Significant at the 0.05 level; **Significant at the 0.01 level.

the northeast China and Hetao region and mainly decreased in the northwest China.

With the landscape and referring to Nie et al. [49], the study area is divided into 3 parts (Figure 4) in this study. Region 1 is the subhumid northeast zone. Region 2 is the semiarid Loess Plateau of mountains and hills covered by scrubland and steppe. Region 3 is a main agricultural area of China, with a typical subhumid and temperate climate. The variations of SM were separately discussed in the following parts. Figure 4 showed the interannual variations of simulated monthly mean and measured SM. The left figures represented SM at 0–10 cm depth; the right figures represented SM at 0–50 cm depth. More statistic figures in Figure 4 were listed in Tables 1, 2, and 3. SM values are first averaged across the regions before computing the statistics. Table 1 showed the correlation coefficients between simulated monthly mean and measured SM at each layer over the subregions. Figure 4 showed that simulated SM basically reflected interannual and yearly variations of measured SM except region 1 at 0–50 cm depth; the humid and arid points were matching. Figure 4 together with Table 1 showed that correlation between simulated and measured SM was significant in region 2 and region 3; correlation coefficients of region 2 were most significant. Correlation coefficient of region 1 was significant only at 0–10 cm depth. The interannual variations at 0–50 cm depth of region 1 showed that the simulated SM reflected yearly variations of measured SM, but there was a phase shift compared to measured SM, and this caused the correlation coefficient to be negative. Correlation between simulated and measured SM of region 1 and region 2 decreased when depth increased; this may relate to imperfect hydrological process in CLM4.0. The simulation of SM in surface is better than in deep layer over some regions. The in situ SM measurements are credible. The simulation of CLM4.0 is imperfect, even though it can capture trends of temporal variation. The land surface in northwest China (region 1) is complex, including forest, river, mountain; the simulation in region 1 is not reasonable. So the correlations in region 1 are lowest or negative. Correlations in south China (region 3) are relatively low. SM in region 3 is always humid; variations of simulated SM caused by forcing data could not be perfect. Simulation ability in region 3 could not reach the variation range. Correlations between CLM4.0 and in situ observations are not good in some stations. But the result is acceptable.

Table 2 presented root mean squared errors (RMSE) and bias between simulated monthly mean and measured SM at each layer over the subregions. The results of RMSE and bias showed that simulated SM was systematically larger than

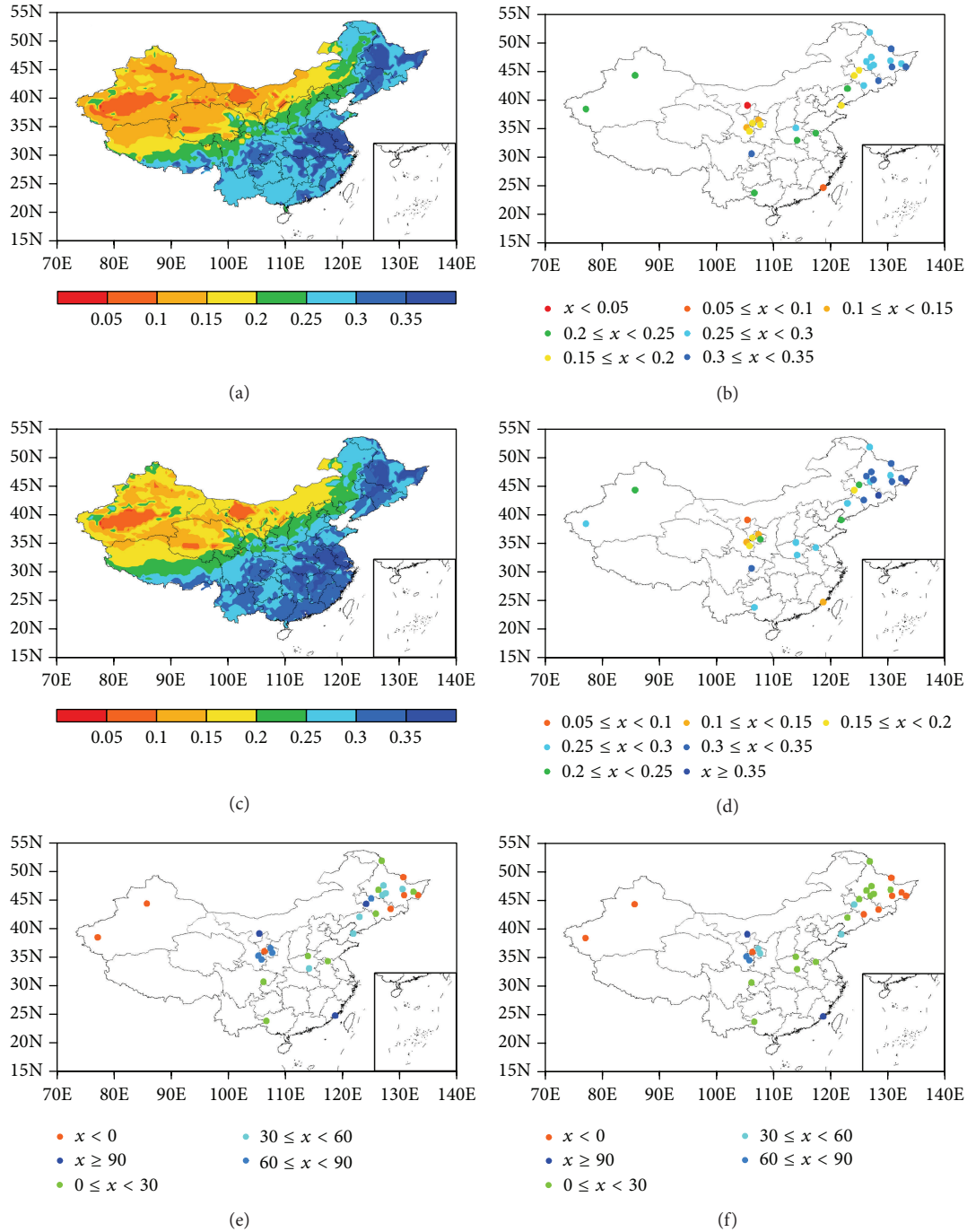


FIGURE 2: Spatial distribution of the simulated mean and measured SM for April to November of 1981-1999 (unit: m^3/m^3). (a) CLM4.0 simulated SM (0-9.06 cm); (b) measured SM (0-10 cm); (c) CLM4.0 simulated SM (0-49.3 cm); (d) measured SM (0-50 cm); (e) bias percent between CLM4.0 simulated (0-9.06 cm) and measured (0-10 cm) SM; and (f) bias percent between CLM4.0 simulated (0-49.3 cm) and measured (0-50 cm) SM.

TABLE 2: The RMSE and bias between simulated monthly mean and measured SM of each layer over the subregions (unit: m^3/m^3).

Regions	0-10 cm		10-20 cm		20-30 cm		30-50 cm		0-50 cm	
	RMSE	Bias	RMSE	Bias	RMSE	Bias	RMSE	Bias	RMSE	Bias
R1	0.067	0.062	0.039	0.028	0.032	0.013	0.03	0.004	0.035	0.022
R2	0.09	0.084	0.088	0.081	0.093	0.088	0.1	0.095	0.094	0.09
R3	0.094	0.083	0.068	0.054	0.059	0.045	0.041	0.022	0.057	0.044

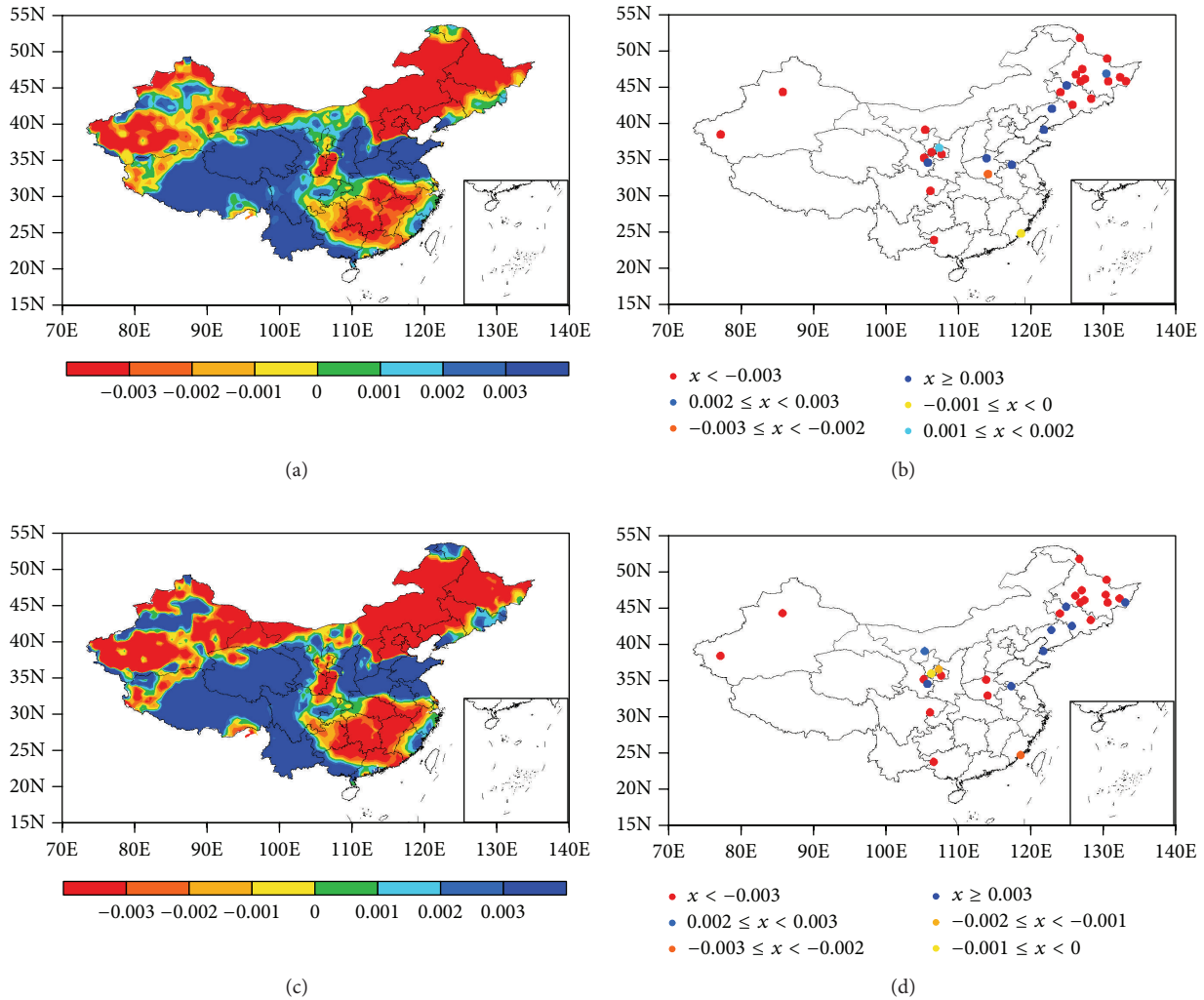


FIGURE 3: Spatial distribution of variation linear trends of simulated mean and measured SM for April to November of 1981–1999 (unit: $(\text{m}^3/\text{m}^3)/10 \text{ a}$). (a) CLM4.0 simulated SM (0–9.06 cm); (b) measured SM (0–10 cm); (c) CLM4.0 simulated SM (0–49.3 cm); and (d) measured SM (0–50 cm).

the ground measured SM at each layer over the three subregions. The RMSE and bias decreased when soil depth increased in region 1 and region 3. In region 1 the measured SM increased when soil depth increased, but variations of simulated SM were not obvious; this made the bias decrease when depth increased. In region 3, the measured SM increased when depth increased, but simulated SM decreased when depth increased; this also made the bias decrease when depth increased.

Table 3 shows the linear trends of simulated and measured SM over the subregions. The linear trends of simulated and measured SM over the three subregions at 0–10 cm depth and 0–50 cm depth were basically consistent at daily, monthly, and yearly time scales. The simulated and measured SM showed decreasing trends of two layers in region 1 and region 2; the simulated and measured SM mostly showed increasing trends of two layers in region 3. The table showed that CLM

had good ability to simulate linear trends of different depth and time scales. Simulation of linear trends at 0–10 cm depth was better than 0–50 cm depth; bias was less than that at 0–50 cm depth.

3.4. Comparison between Measured, CLM4.0, NCEP Reanalysis, ERA Interim/Land, and Microwave SM. Figure 5 showed spatial distributions of three kinds of SM products. The spatial distributions of four SM products (CLM4.0, NCEP, ERA Interim/Land, and SM-MW) and measured SM were basically consistent with each other. In general, the four SM products reasonably reflected spatial distribution characteristics of measured SM. The four SM products gradually increased from northwest to southeast. From distribution difference it was revealed that humid regions of CLM4.0 SM were located over northeast China and Jianghuai region

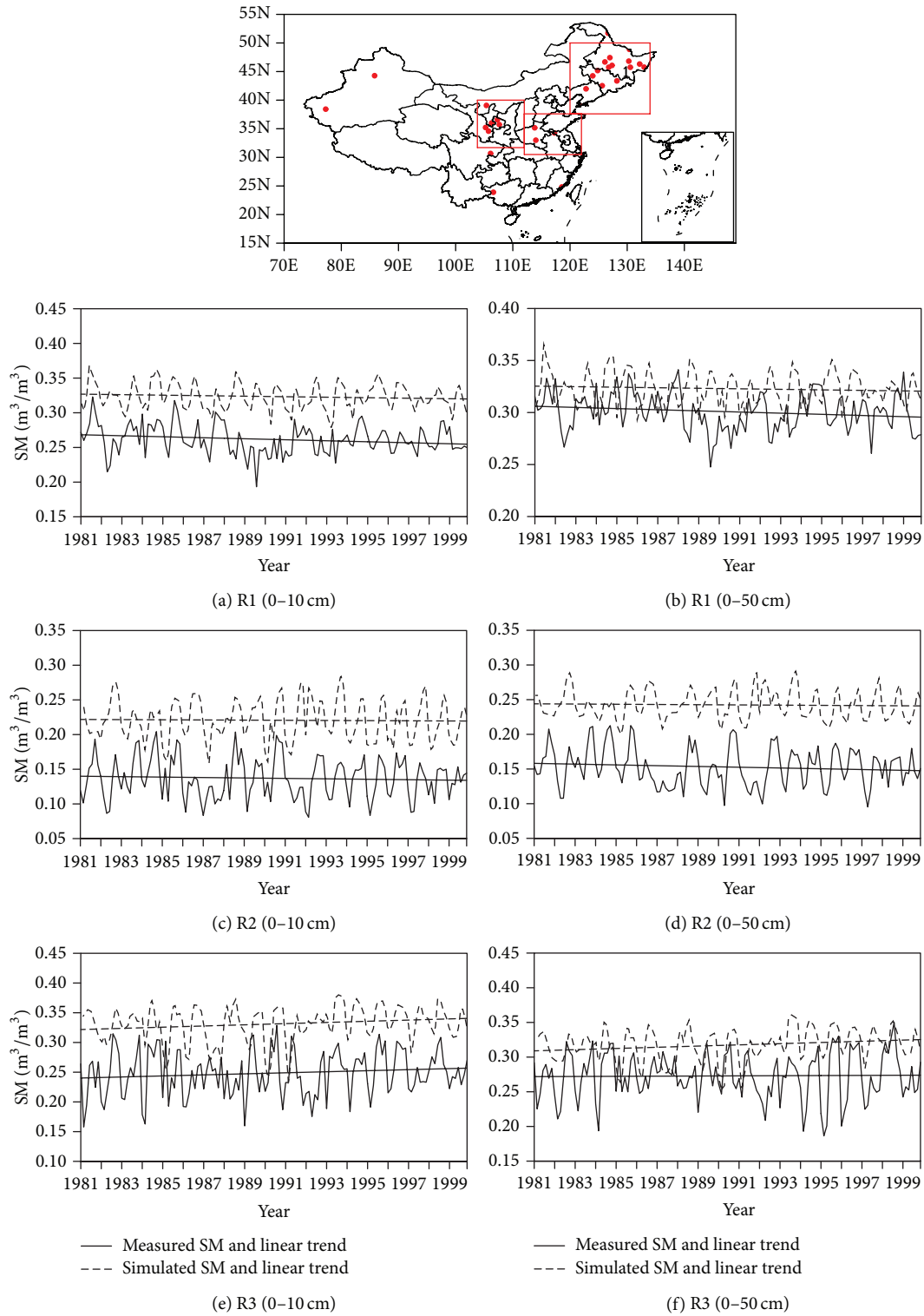


FIGURE 4: The interannual variations of CLM4.0 simulated monthly mean and the ground measured SM for 1, 2, and 3 regions (a, c, and e) 0–10 cm depth; (b, d, and f) 0–50 cm depth.

(Figure 2(a)). The humid regions of NCEP SM were located over the east of the Tibetan Plateau, the middle and lower reaches of Yangtze River, and south China. Humid regions of SM-MW were located over southern area of 30°N. Extent of arid regions in northwest China, of the four SM products was different from each other.

The humid regions of NCEP SM were located over the east of the Tibetan Plateau, the middle and lower reaches of Yangtze River, and south China. Humid regions of SM-MW were located over southern area of 30°N. Extent of arid regions in northwest China, of the four SM products was different from each other.

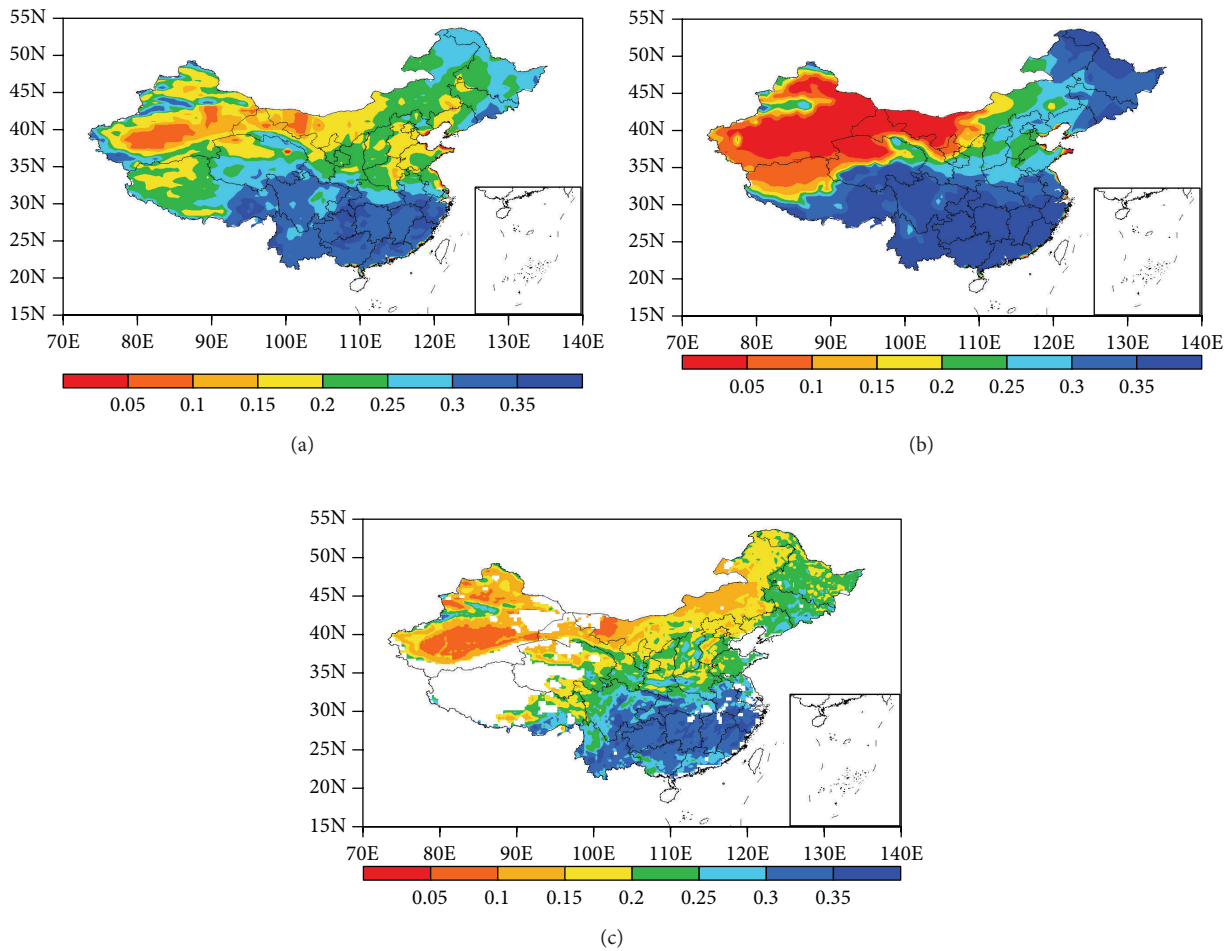


FIGURE 5: Spatial distribution of SM for April to November of 1981–1999 (unit: m^3/m^3). (a) NCEP SM (0–10 cm); (b) ERA Interim/Land (0–7 cm); and (c) SM-MW.

TABLE 3: The linear trends of simulated and measured SM over the subregions (unit: $(m^3/m^3)/10 a$).

Regions	0–10 cm		0–50 cm	
	Obs.	Simu.	Obs.	Simu.
Daily				
R1	-0.0072**	-0.0056*	-0.0055**	-0.0032
R2	-0.0031	-0.0015	-0.0055*	-0.0015
R3	0.0088*	0.0096**	0.0012	0.0096**
Monthly				
R1	-0.0072*	-0.0037	-0.0055	-0.0026
R2	-0.0031	-0.0012	-0.0056	-0.0016
R3	0.0088	0.0099	0.0011	0.0086*
Yearly				
R1	-0.0077	-0.0045	-0.0052	-0.0035
R2	-0.0048	-0.0032	-0.0069	-0.003
R3	0.0072	0.0087	-0.0005	0.0076

* Significant at the 0.05 level; ** Significant at the 0.01 level, *F*-test.

4. Temporal Spatial Variation of SM in China and Its Possible Response to Climate Change

Because soil was frozen in the autumn, winter, and early spring of northern areas of China, the summer was chosen as the representative season to investigate the spatial distribution, temporal variation of SM, and its possible response to climate change. The SM spatial distributions of different layers (0–9.06 cm, 9.06–16.56 cm, 16.56–28.92 cm, 28.92–49.3 cm, and 0–49.3 cm) in summer of 1961–2010 were simulated by CLM4.0. In general, the spatial distributions of every soil layer were characterized by a gradually increasing pattern from the northwest to the southeast. Dry regions were located over the Xinjiang, Qinghai, Gansu Province, and the western Inner Mongolia. There are low precipitation and strong radiation in these regions, and average SM was below 0.20 (0–49.3 cm). The most humid regions were located over the Northeast Plain, Jianghuai region, and the Yangtze River

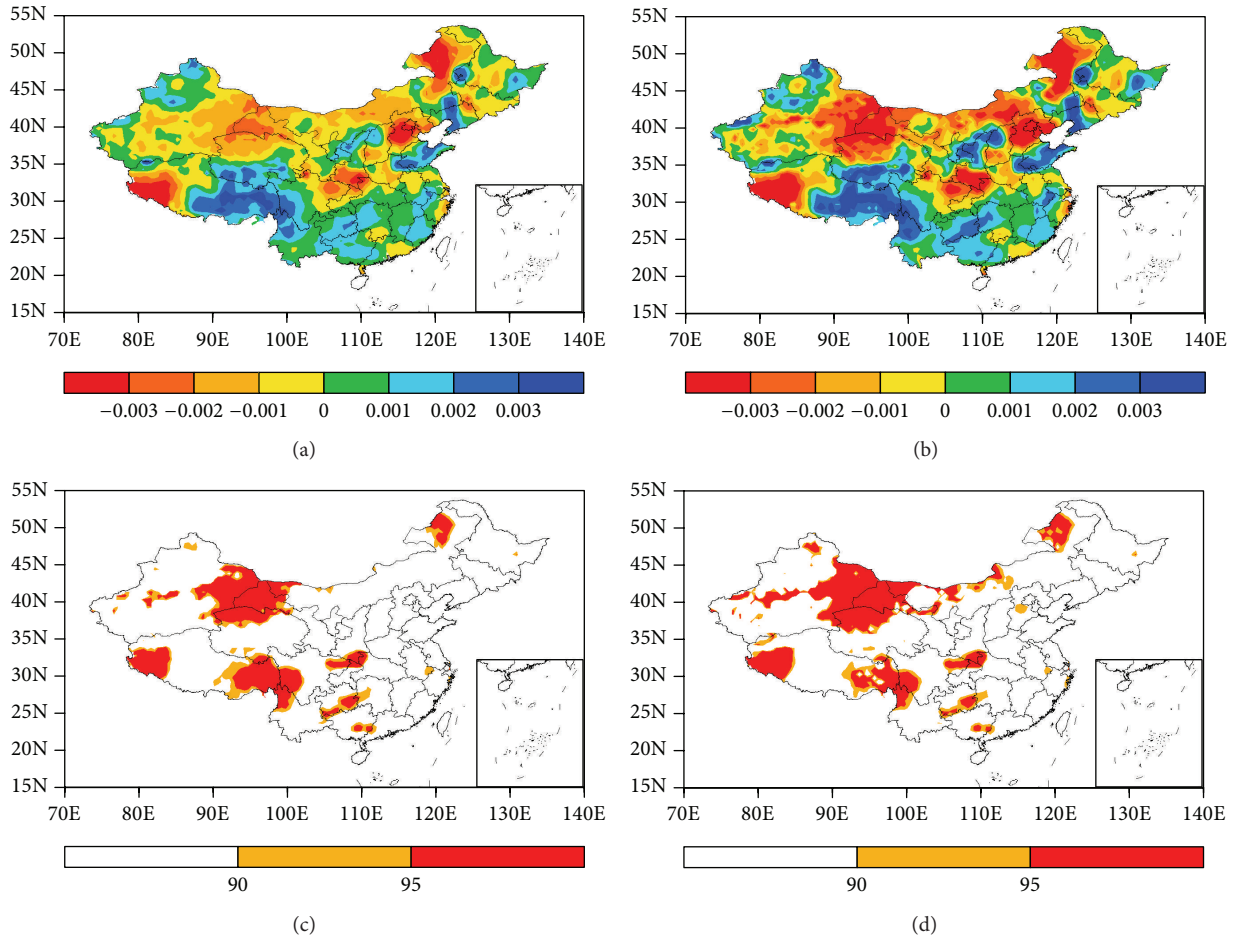


FIGURE 6: Spatial distribution of simulated mean SM variation linear trends for the summer (June–August) of 1961–2010 (unit: $(\text{m}^3/\text{m}^3)/10$): (a) 0–9.06 cm; (b) 0–49.3 cm and significant level for variation linear trends (unit: %; orange, significant at the 90% level; red, significant at the 95% level; F -test): (c) 0–9.06 cm; (d) 0–49.3 cm.

basin. Precipitation in these regions was relatively larger, and average SM exceeded 0.35 (0–49.3 cm). SM increased when soil depth increased in the northwest, southwest, and south China. The increase trend was most obvious at 28.92–49.3 cm depth, and the SM in most areas exceeded 0.30 except part of northwest. The SM increased from surface layer to deeper layer in general. The spatial distributions of simulated SM by CLM4.0 were basically consistent with other works [1].

Figure 6 showed spatial distribution of simulated mean SM variation linear trends for the summer (June–August) of 1961–2010 in two layers. The variation trends basically showed consistencies in all layers. The SM mainly decreased in the northern area of 35°N besides the western Xinjiang Province and partial regions of northeast China, and SM mainly increased in Yangtze River basin, south and southwest China to the southern area of 30°N . Variations were significant in partial region of northwest China in 0–49.3 cm layer, and variations in part region of southwest were significant. The decreasing trends were more significant with soil depth increase in domain north of 35°N arid and semiarid regions, showed arid trends in north regions, and were more severe with soil depth increase. The SM appreciably increased

with soil depth increase in south regions, and trends were not significant. Compared to variation trends of Princeton precipitation and temperature of the same time period (1961–2010), it is shown that temperature increased in most regions of China. In northern areas of 35°N , the precipitation increased in Xinjiang province and partial regions of northeast China and decreased in other regions. In southern areas of 35°N , the precipitation increased in Jianghua region, Yangtze River basin, south China, and partial region of southwest China. The variations were basically consistent with measured temperature and precipitation [50]. Under the global warming background, the simulated SM basically demonstrated responses to the precipitation variation. The simulated SM decreased in most regions of north China, the simulated SM increased in Jianghua region, Yangtze River basin, and south China, and the variations were more obvious in deep layer.

Because of the regional heterogeneity of SM variation and its trends to climate change [1] and the fact that SM is very sensitive to precipitation in the forcing datasets [10], the arid region of the northwest, semiarid region of north China, and humid region of the middle and lower reaches of Yangtze

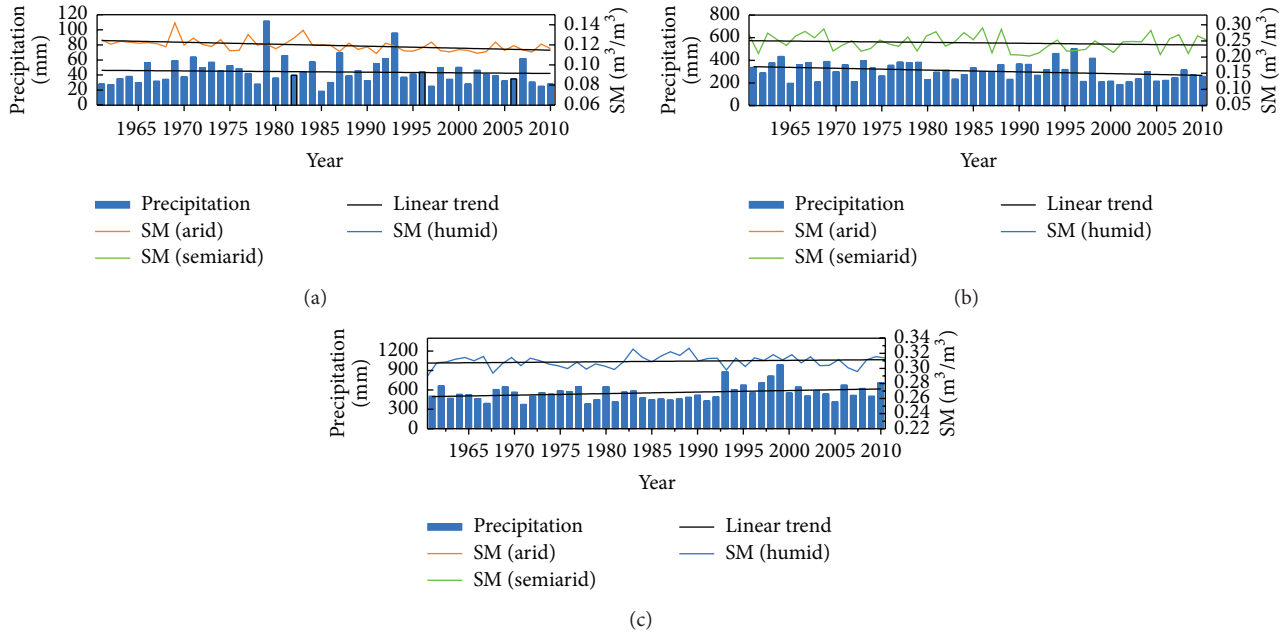


FIGURE 7: Intercomparison of the variation trends between the simulated SM and forcing precipitation in summer (June–August) in typical regions for the period 1961–2010. (a) Arid region; (b) semiarid region; and (c) humid region.

River and the south China were chosen as typical regions in this study to discuss SM variation and regional heterogeneity of its response to precipitation during 1961–2010. Variations in the three regions were somewhat significant. Figure 7 showed intercomparison of variation trends between the simulated SM and forcing precipitation of the summer (June–August) in typical regions for the period 1961–2010. SM in arid region significantly decreased (statistically significant at $\alpha = 0.01$ level, F -test), and precipitation decreased too. SM and precipitation in semiarid region slightly decreased. SM and precipitation in humid region slightly increased. Temperature increased in all the three regions, and increase trends were significant in arid and semiarid regions (figures were not provided). Correlation coefficient of monthly mean SM and precipitation in humid region was 0.47, 0.36 in semiarid region, all were statistically significant at $\alpha = 0.01$ level. Correlation coefficient of monthly mean SM and precipitation in arid region was 0.16 and was statistically significant at $\alpha = 0.05$ level. Precipitation in humid region was large; the influences of evapotranspiration on SM were small because of the high SM in the region. Precipitation was the principal variable that controlled SM in the humid region. SM in semiarid and arid regions is relatively lower; the influence of precipitation was weakened in these regions. The combined actions of climatological factor, surface properties, and additional factors controlled and complicated the variations in SM [1]. To sum up, the simulated SM basically demonstrated responses to the precipitation variation under the global warming background, and correlation coefficients between SM and precipitation were significant positive values; this conclusion was similar to that included in other researches [51]. Precipitation decreased in the arid region of

the northwest, semiarid region of the north China, and precipitation increased in humid region of south. The variations were basically consistent with measured precipitation. The simulated SM of summer demonstrated different responses to the precipitation variation. The simulated SM decreased in the arid region of the northwest, semiarid region of the north China, and increased in humid region of south. Response to precipitation was most significant in humid region, while the semiarid and arid regions were ranked second.

5. Discussion

In general, CLM4.0 simulations captured the temporal spatial variation of the measured SM. The spatial distribution of simulated SM is basically consistent with NCEP Reanalysis, SM-MW, and ERA Interim/Land SM data.

5.1. SM Range. The SM numerical simulations are still challengeable at this stage; the simulated results are only potential in actual applications. Results presented in the previous section show that CLM4.0 simulations tend to overestimate SM over China. There are several causes for these discrepancies between simulated and measured SM. The measured SM is taken at a given site, but the spatial distribution of SM is heterogeneous. There is uncertainty in the measured SM at a given depth to represent SM of whole layer. The simulated SM denoted SM at given node to represent SM of whole layer; it also induced uncertainty. Layer depth difference of measurement and simulation also causes errors. Moreover, the simulated SM is average value of grid, the measured SM is value at a given site, and the intercomparisons

have uncertainty. Mismatch between the point measurement and model grid result is not well processed; an up-scaling processing is also needed for ground measurements. At the same time, difference between land surface datasets of CLM4.0 and practical surface datasets of China, imperfect description of hydrological scheme in CLM4.0, and accuracy of atmospheric forcing datasets of the model can make simulation bias. The vertical SM transport is governed by infiltration, surface and subsurface runoff, gradient diffusion, gravity, canopy transpiration through root extraction, and interactions with groundwater, but description of transport of soil heat and SM is not perfect in CLM4.0.

The global land surface datasets of CLM4.0 might not be fully applicable in China. The implementation of new datasets such as the new soil texture, soil color, and plant functional types could lead to better results. A China dataset of soil properties for land surface modeling could be used [52], which is from <http://westdc.westgis.ac.cn/data/11573187-fd64-47b1-81a6-0c7c224112a0>. Satellite remote sensing can provide high spatial-temporal SM product; its regional distribution is reliable, but the absolute values are still questionable; this is also the case for other reanalysis datasets. In order to overcome these shortages in our future investigations, the improvement of hydrological process modeling, atmospheric forcing datasets, and land surface data is important direction for further development of CLM4.0.

5.2. SM Variability. In this study observations at specific sites are compared with CLM4.0 output at resolution of 0.5° . Spatial variability of SM is very high and can vary from centimeters to meters. Precipitation, evapotranspiration, soil texture, topography, vegetation, and land use could either enhance or reduce the spatial variability of SM depending on how it is distributed and combined with other factors [53]. While comparisons between CLM4.0 simulations and in situ data provide good correlations, they still have high RMSEs as discussed above. These results are in agreement with the suggestion that the true information content of modeled SM does not necessarily rely on their absolute magnitudes but instead on their time variation [54–57]. And their time variation represents the time-integrated impacts of antecedent meteorological forcing on the hydrological state of the soil system with the model [54].

6. Conclusion

The CLM4.0 driven by the atmospheric forcing data of Princeton University was deployed to simulate SM from 1961 to 2010 over China. The simulated SM was compared to the ground observations, NCEP Reanalysis, SM-MW, and ERA Interim/Land SM data. The characteristics of the spatial distribution and temporal spatial variation of SM and its response to climate change were discussed. The following conclusions are drawn.

CLM4.0 simulation was capable of capturing characteristics of the spatial distribution and temporal spatial variation. The simulated SM reasonably reflects spatial distribution characteristics of measure SM, where the humid regions were

located over northeast China and Jianghuai basin and dry region was located over Hetao region. But the simulated SM was systematically higher than the observations in each layer over these regions; the simulated SM revealed the measured variation trends of the different layers at different time scales. Correlation between measured and simulated SM was not significant below 10 cm depth in northeast China, and correlation was significant in the other two regions of each layer. The simulated, NCEP, SM-MW, and ERA Interim/Land SM products were reasonably consistent with each other.

Based on the simulated SM of summer (June to August) in 1961–2010, it was concluded that the spatial distribution in every layer was characterized by a gradually increasing pattern from the northwest to southeast. Dry regions were located over the Xinjiang, Qinghai, and Gansu Provinces and the western Inner Mongolia, while the most humid regions were located over the Northeast Plain, Jianghuai region, and the Yangtze River basin. The SM increased from surface layer to deeper layer in general; the variation trends basically showed consistencies in all layers. SM mainly decreased in the northern area of 35°N besides western Xinjiang Province and partial regions of northeast China, and SM mainly increased in Yangtze River basin, south and southwest China in the southern area of 30°N . The decreasing trends were more significant with soil depth increase in domain north of 35°N arid and semiarid regions; in the global warming background, the simulated SM of summer demonstrated different responses to the precipitation variation. SM decreased in typical arid and semiarid regions, while SM increased in humid region. The variation distribution of SM and measured precipitation had consistencies. The humid region significant responded to precipitation, and the correlation coefficient was 0.47. While the semiarid and arid regions were ranked second.

This study showed that CLM4.0 driven by Princeton forcing data is potential in characterizing the spatial distribution and temporal spatial variation of SM in China, but the simulated SM had large systematic biases. This was relevant to land data, quality of forcing data, imperfect physical processes, and so forth. At the same time, intercomparison between measured and simulated SM at each depth and geographical location has inconsistency. All of these may cause simulation bias. So our future investigation will highly account for the high quality land and forcing data; the physical process of SM transport and parameterization of hydrological scheme will be further explored. Realistic initial states for the SM variables are required from many applications and from forecasts of weather and seasonal climate variations to models of plant growth and carbon fluxes.

Conflict of Interests

The authors declare that there is no conflict of interests regarding the publication of this paper.

Acknowledgments

This study is supported by the China Special Fund for Meteorological Research in the Public Interest (Major projects)

(Grant no. GYHY201506001-6), National Science Foundation of China (Grant nos. 41375022, 41275079, 41305077, and 41405069), Key Research Program of the Chinese Academy of Sciences (Grant no. KZZD-EW-13), and Research fund of Chengdu University of Information Technology (Grant nos. J201516 and J201518). The authors would like to thank Zhao Guohui in Cold and Arid Regions Environmental and Engineering Research Institute of Chinese Academy of Sciences. The authors also would like to thank all reviewers for their constructive comments.

References

- [1] M. X. Li, Z. G. Ma, and G.-Y. Niu, "Modeling spatial and temporal variations in soil moisture in China," *Chinese Science Bulletin*, vol. 56, no. 17, pp. 1809–1820, 2011.
- [2] S. I. Seneviratne, T. Corti, E. L. Davin et al., "Investigating soil moisture-climate interactions in a changing climate: a review," *Earth-Science Reviews*, vol. 99, no. 3-4, pp. 125–161, 2010.
- [3] W. Dorigo, P. van Oevelen, W. Wagner et al., "A new international network for in situ soil moisture data," *Eos*, vol. 92, no. 17, pp. 141–142, 2011.
- [4] W. A. Dorigo, W. Wagner, R. Hohensinn et al., "The International Soil Moisture Network: a data hosting facility for global in situ soil moisture measurements," *Hydrology and Earth System Sciences*, vol. 15, no. 5, pp. 1675–1698, 2011.
- [5] W. A. Dorigo, A. Xaver, M. Vreugdenhil et al., "Global automated quality control of in situ soil moisture data from the International Soil Moisture Network," *Vadose Zone Journal*, vol. 12, no. 3, 2013.
- [6] A. Wang and X. B. Zeng, "Sensitivities of terrestrial water cycle simulations to the variations of precipitation and air temperature in China," *Journal of Geophysical Research D: Atmospheres*, vol. 116, 2011.
- [7] G. Balsamo, C. Albergel, A. Beljaars et al., "ERA-Interim/Land: a global land surface reanalysis data set," *Hydrology and Earth System Sciences*, vol. 19, no. 1, pp. 389–407, 2015.
- [8] M. Rodell, P. R. Houser, U. Jambor et al., "The global land data assimilation system," *Bulletin of the American Meteorological Society*, vol. 85, no. 3, pp. 381–394, 2004.
- [9] R. H. Reichle, "The MERRA-land data product," GMAO Office Note 3, Global Modeling and Assimilation Office, 2012, <http://gmao.gsfc.nasa.gov/pubs/docs/Reichle541.pdf>.
- [10] T. T. Qian, A. G. Dai, K. E. Trenberth, and K. W. Oleson, "Simulation of global land surface conditions from 1948 to 2004. Part I: forcing data and evaluations," *Journal of Hydrometeorology*, vol. 7, no. 5, pp. 953–975, 2006.
- [11] S. L. Guo, J. Guo, J. Zhang, and C. Hua, "VIC distributed hydrological model to predict climate change impact in the Hanjiang basin," *Science in China, Series E: Technological Sciences*, vol. 52, no. 11, pp. 3234–3239, 2009.
- [12] X. Liang, D. P. Lettenmaier, E. F. Wood, and S. J. Burges, "A simple hydrologically based model of land surface water and energy fluxes for GSMs," *Journal of Geophysical Research: Atmospheres*, vol. 99, no. D7, pp. 14,415–14,428, 1994.
- [13] B. Decharme, C. Ottl , S. Saux-Picart et al., "A new land surface hydrology within the Noah-WRF land-atmosphere mesoscale model applied to semiarid environment: evaluation over the dantiandou kori (Niger)," *Advances in Meteorology*, vol. 2009, Article ID 731874, 13 pages, 2009.
- [14] D. P. Dee, S. M. Uppala, A. J. Simmons et al., "The ERA-Interim reanalysis: configuration and performance of the data assimilation system," *Quarterly Journal of the Royal Meteorological Society*, vol. 137, no. 656, pp. 553–597, 2011.
- [15] M. M. Rienecker, M. J. Suarez, R. Gelaro et al., "MERRA: NASA's modern-era retrospective analysis for research and applications," *Journal of Climate*, vol. 24, no. 14, pp. 3624–3648, 2011.
- [16] C. Albergel, P. de Rosnay, C. Gruhier et al., "Evaluation of remotely sensed and modelled soil moisture products using global ground-based in situ observations," *Remote Sensing of Environment*, vol. 118, pp. 215–226, 2012.
- [17] C. Albergel, W. Dorigo, R. H. Reichle et al., "Skill and global trend analysis of soil moisture from reanalyses and microwave remote sensing," *Journal of Hydrometeorology*, vol. 14, no. 4, pp. 1259–1277, 2013.
- [18] M. Owe, R. de Jeu, and T. Holmes, "Multisensor historical climatology of satellite-derived global land surface moisture," *Journal of Geophysical Research F: Earth Surface*, vol. 113, no. 1, Article ID F01002, 2008.
- [19] E. G. Njoku, T. J. Jackson, V. Lakshmi, T. K. Chan, and S. V. Nghiem, "Soil moisture retrieval from AMSR-E," *IEEE Transactions on Geoscience and Remote Sensing*, vol. 41, no. 2, pp. 215–229, 2003.
- [20] Z. Bartalis, W. Wagner, V. Naeimi et al., "Initial soil moisture retrievals from the METOP-A Advanced Scatterometer (ASCAT)," *Geophysical Research Letters*, vol. 34, no. 20, Article ID L20401, 2007.
- [21] L. Li, P. W. Gaiser, B.-C. Gao et al., "WindSat global soil moisture retrieval and validation," *IEEE Transactions on Geoscience and Remote Sensing*, vol. 48, no. 5, pp. 2224–2241, 2010.
- [22] R. M. Parinussa, T. R. H. Holmes, and R. A. M. de Jeu, "Soil moisture retrievals from the windSat spaceborne polarimetric microwave radiometer," *IEEE Transactions on Geoscience and Remote Sensing*, vol. 50, no. 7, pp. 2683–2694, 2012.
- [23] Y. H. Kerr, P. Waldteufel, J.-P. Wigneron et al., "The SMOS mission: new tool for monitoring key elements of the global water cycle," *Proceedings of the IEEE*, vol. 98, no. 5, pp. 666–687, 2010.
- [24] S. Mecklenburg, M. Drusch, Y. H. Kerr et al., "ESA's soil moisture and ocean salinity mission: mission performance and operations," *IEEE Transactions on Geoscience and Remote Sensing*, vol. 50, no. 5, pp. 1354–1366, 2012.
- [25] W. Dorigo, R. de Jeu, D. Chung et al., "Evaluating global trends (1988–2010) in harmonized multi-satellite surface soil moisture," *Geophysical Research Letters*, vol. 39, no. 17, Article ID L18405, 2012.
- [26] Y. Y. Liu, W. A. Dorigo, R. M. Parinussa et al., "Trend-preserving blending of passive and active microwave soil moisture retrievals," *Remote Sensing of Environment*, vol. 123, pp. 280–297, 2012.
- [27] Y. Y. Liu, R. M. Parinussa, W. A. Dorigo et al., "Developing an improved soil moisture dataset by blending passive and active microwave satellite-based retrievals," *Hydrology and Earth System Sciences*, vol. 15, no. 2, pp. 425–436, 2011.
- [28] W. Wagner, W. Dorigo, R. de Jeu et al., "Fusion of active and passive microwave observations to create an Essential Climate Variable data record on soil moisture," in *Proceedings of the 22nd ISPRS Congress*, Melbourne, Australia, 2012.
- [29] R. E. Dickinson, K. W. Oleson, G. Bonan et al., "The community land model and its climate statistics as a component of the

- community climate system model," *Journal of Climate*, vol. 19, no. 11, pp. 2302–2324, 2006.
- [30] K. W. Oleson, G.-Y. Niu, Z.-L. Yang et al., "Improvements to the community land model and their impact on the hydrological cycle," *Journal of Geophysical Research G: Biogeosciences*, vol. 113, no. 1, Article ID G01021, 2008.
- [31] M. Decker and X. Zeng, "Impact of modified Richards equation on global soil moisture simulation in the community land model (CLM3.5)," *Journal of Advances in Modeling Earth Systems*, 2009.
- [32] X. Zeng and M. Decker, "Improving the numerical solution of soil moisture-based Richards equation for land models with a deep or shallow water table," *Journal of Hydrometeorology*, vol. 10, no. 1, pp. 308–319, 2009.
- [33] K. Sakaguchi and X. Zeng, "Effects of soil wetness, plant litter, and under-canopy atmospheric stability on ground evaporation in the Community Land Model (CLM3.5)," *Journal of Geophysical Research D: Atmospheres*, vol. 114, no. 1, Article ID D01107, 2009.
- [34] M. G. Flanner and C. S. Zender, "Snowpack radiative heating: influence on Tibetan Plateau climate," *Geophysical Research Letters*, vol. 32, no. 6, pp. 1–5, 2005.
- [35] M. G. Flanner and C. S. Zender, "Linking snowpack microphysics and albedo evolution," *Journal of Geophysical Research D: Atmospheres*, vol. 111, no. 12, 2006.
- [36] M. G. Flanner, C. S. Zender, J. T. Randerson, and P. J. Rasch, "Present-day climate forcing and response from black carbon in snow," *Journal of Geophysical Research D: Atmospheres*, vol. 112, no. 11, Article ID D11202, 2007.
- [37] D. M. Lawrence, A. G. Slater, V. E. Romanovsky, and D. J. Nicolsky, "Sensitivity of a model projection of near-surface permafrost degradation to soil column depth and representation of soil organic matter," *Journal of Geophysical Research F: Earth Surface*, vol. 113, no. 2, Article ID F02011, 2008.
- [38] K. W. Oleson, G. B. Bonan, J. Feddema, and M. Vertenstein, "An urban parameterization for a global climate model. 1. Formulation and evaluation for two cities," *Journal of Applied Meteorology and Climatology*, vol. 47, pp. 1038–1060, 2008.
- [39] N. Ramankutty, A. T. Evan, C. Monfreda, and J. A. Foley, "Farming the planet: 1. Geographic distribution of global agricultural lands in the year 2000," *Global Biogeochemical Cycles*, vol. 22, no. 1, Article ID GB1003, 2008.
- [40] G. P. Asner, C. A. Wessman, D. S. Schimel, and S. Archer, "Variability in leaf and litter optical properties: Implications for BRDF model inversions using AVHRR, MODIS, and MISR," *Remote Sensing of Environment*, vol. 63, no. 3, pp. 243–257, 1998.
- [41] J. Sheffield, G. Goteti, and E. F. Wood, "Development of a 50-year high-resolution global dataset of meteorological forcings for land surface modeling," *Journal of Climate*, vol. 19, no. 13, pp. 3088–3111, 2006.
- [42] E. Kalnay, M. Kanamitsu, R. Kistler et al., "The NCEP/NCAR 40-year reanalysis project," *Bulletin of the American Meteorological Society*, vol. 77, no. 3, pp. 437–471, 1996.
- [43] J. Sheffield and E. F. Wood, "Characteristics of global and regional drought, 1950–2000: analysis of soil moisture data from off-line simulation of the terrestrial hydrologic cycle," *Journal of Geophysical Research D: Atmospheres*, vol. 112, no. 17, 2007.
- [44] J. Sheffield, K. M. Andreadis, E. F. Wood, and D. P. Lettenmaier, "Global and continental drought in the second half of the twentieth century: severity-area-duration analysis and temporal variability of large-scale events," *Journal of Climate*, vol. 22, no. 8, pp. 1962–1981, 2009.
- [45] H. B. Li, A. Robock, S. X. Liu, X. G. Mo, and P. Viterbo, "Evaluation of reanalysis soil moisture simulations using updated Chinese soil moisture observations," *Journal of Hydrometeorology*, vol. 6, no. 2, pp. 180–193, 2005.
- [46] S. Levis, C. Wiedinmyer, G. B. Bonan, and A. Guenther, "Simulating biogenic volatile organic compound emissions in the Community Climate System Model," *Journal of Geophysical Research D: Atmospheres*, vol. 108, no. 21, p. 4659, 2003.
- [47] S. H. Suranjana, S. Moorthi, H. L. Pan et al., "The NCEP climate forecast system reanalysis," *Bulletin of the American Meteorological Society*, vol. 91, no. 8, pp. 1015–1057, 2010.
- [48] A. Loew, T. Stacke, W. Dorigo, R. de Jeu, and S. Hagemann, "Potential and limitations of multidecadal satellite soil moisture observations for selected climate model evaluation studies," *Hydrology and Earth System Sciences*, vol. 17, no. 9, pp. 3523–3542, 2013.
- [49] S. Nie, Y. Luo, and J. Zhu, "Trends and scales of observed soil moisture variations in China," *Advances in Atmospheric Sciences*, vol. 25, no. 1, pp. 43–58, 2008.
- [50] P. Zhai, X. Zhang, H. Wan, and X. Pan, "Trends in total precipitation and frequency of daily precipitation extremes over China," *Journal of Climate*, vol. 18, no. 7, pp. 1096–1108, 2005.
- [51] Y. Z. Luo, Z. G. Wang, X. M. Liu, and M. H. Zhang, "Spatial and temporal variability of precipitation in Haihe River Basin, China: characterization and management implications," *Advances in Meteorology*, vol. 2014, Article ID 143246, 9 pages, 2014.
- [52] W. Shangguan, Y. Dai, B. Liu et al., "A China data set of soil properties for land surface modeling," *Journal of Advances in Modeling Earth Systems*, 2013.
- [53] J. S. Famiglietti, D. Ryu, A. A. Berg, M. Rodell, and T. J. Jackson, "Field observations of soil moisture variability across scales," *Water Resources Research*, vol. 44, no. 1, Article ID W01423, 2008.
- [54] C. Albergel, P. de Rosnay, G. Balsamo, L. Isaksen, and J. Muñoz-Sabater, "Soil moisture analyses at ECMWF: evaluation using global ground-based in situ observations," *Journal of Hydrometeorology*, vol. 13, no. 5, pp. 1442–1460, 2012.
- [55] J. A. Saleem and G. D. Salvucci, "Comparison of soil wetness indices for inducing functional similarity of hydrologic response across sites in Illinois," *Journal of Hydrometeorology*, vol. 3, no. 1, pp. 80–91, 2002.
- [56] W. A. Dorigo, W. Wagner, R. Hohensinn et al., "The international soil moisture network: a data hosting facility for global in situ soil moisture measurements," *Hydrology and Earth System Sciences*, vol. 15, pp. 1675–1698, 2011.
- [57] R. D. Koster, Z. Guo, R. Yang, P. A. Dirmeyer, K. Mitchell, and M. J. Puma, "On the nature of soil moisture in land surface models," *Journal of Climate*, vol. 22, no. 16, pp. 4322–4335, 2009.

Research Article

A Critical Evaluation of the Nonparametric Approach to Estimate Terrestrial Evaporation

Yongmin Yang,^{1,2} Hongbo Su,³ and Jianwei Qi⁴

¹State Key Laboratory of Simulation and Regulation of Water Cycle in River Basin, Beijing 100038, China

²Research Center on Flood and Drought Disaster Reduction of the Ministry of Water Resources, China Institute of Water Resources and Hydropower Research, Beijing 100038, China

³Department of Civil, Environmental and Geomatic Engineering, Florida Atlantic University, Boca Raton, FL 33431, USA

⁴China Aero Geophysics Survey and Remote Sensing Center for Land and Resources, Beijing 100083, China

Correspondence should be addressed to Hongbo Su; hongbo@ieee.org

Received 7 April 2015; Accepted 13 May 2015

Academic Editor: Marcos Heil Costa

Copyright © 2016 Yongmin Yang et al. This is an open access article distributed under the Creative Commons Attribution License, which permits unrestricted use, distribution, and reproduction in any medium, provided the original work is properly cited.

Evapotranspiration (ET) estimation has been one of the most challenging problems in recent decades for hydrometeorologists. In this study, a nonparametric approach to estimate terrestrial evaporation was evaluated using both model simulation and measurements from three sites. Both the model simulation and the in situ evaluation at the Tiger Bush Site revealed that this approach would greatly overestimate ET under dry conditions (evaporative fraction smaller than 0.4). For the evaluation at the Tiger Bush Site, the difference between ET estimates and site observations could be as large as 130 W/m^2 . However, this approach provided good estimates over the two crop sites. The Nash-Sutcliffe coefficient (E) was 0.9 and 0.94, respectively, for WC06 and Yingke. A further theoretical analysis indicates the nonparametric approach is very close to the equilibrium evaporation equation under wet conditions, and this can explain the good performance of this approach at the two crop sites in this study. The evaluation indicates that this approach needs more careful appraisal and that its application in dry conditions should be avoided.

1. Introduction

Water is fundamental to the coupled human-environment systems [1, 2]. The role of the land surface in partitioning available water between evaporation and runoff and in partitioning available energy between sensible and latent heat fluxes is significant and affects the state of the atmosphere directly [3, 4]. Evapotranspiration is a very important process that relates to energy and water exchange between the hydrosphere, atmosphere, and biosphere [5, 6]. Accurate estimate of ET will benefit water planning and management in arid and semiarid areas. Many methods have been proposed to measure ET at various scales [7]. Sap-flow and porometer readings are often used to measure ET from individual plants. The Bowen ratio and lysimeter and scintillometer readings are used to measure ET from fields. Eddy covariance (EC) and catchment water balance are often used to measure ET on a landscape scale. Remote sensing-based ET models are suitable for estimating ET on a regional scale.

Hydrometeorologists have striven for decades to estimate natural evaporation from land surfaces. Dalton [8] related evaporation to a wind function and vapor pressure deficit. Fick [9] proposed a one-dimensional form of diffusion equation, which greatly contributed to the understanding of evaporation. Bowen [10] presented the ratio of heat loss by conduction to that by evaporation (known as the Bowen ratio) as a function of vertical temperature and humidity gradients. Later, the Bowen ratio method is widely used for measuring ET. Penman [11] advanced the evaporation theory and proposed the combination method to estimate evaporation from an open water surface. Monteith [12] developed the Penman equation and extended it to cropped surfaces by introducing the surface and aerodynamic resistance. In the past few years, the FAO Penman-Monteith equation was recommended to estimate reference ET (ET_0), and the “Kc- ET_0 ” approach has been widely used for computing crop water requirements [13]. Comprehensive reviews of the historical study of the natural evaporation from land can

be found in numerous papers [3, 14, 15]. However, large discrepancies in latent and sensible heat fluxes were reported between field observations and general circulation model (GCM) simulations based on the above ET methods [16]. In the abovementioned methods, transfer coefficients such as surface resistance, conductance, or bulk coefficient are semiempirically or empirically parameterized and lead to different results and uncertainties in ET estimates [7, 17] because most of them could not be measured directly [15].

Recently, a nonparametric approach was proposed by Liu et al. [18] to estimate terrestrial evaporation. The nonparametric approach is derived from the thermodynamic process following Hamilton's principle. This approach requires measurements of air temperature, surface temperature, net radiation, and soil heat flux. The solution is simple and no parameterization of a transfer coefficient is needed. Liu et al. [18] evaluated this approach with observations from 26 eddy covariance sites, and they found that this approach showed a good performance at 23 sites. They further found that the nonparametric approach could achieve a compatible performance to the Penman-Monteith approach at two observation sites. However, careful appraisal is needed, and a more critical evaluation of the nonparametric approach is necessary. The purpose of this paper is to evaluate the capability of the nonparametric approach to predict ET at various soil moisture conditions. Section 2 presents a brief description of the nonparametric approach, the Penman-Monteith approach, and the Bowen ratio approach. Section 3 describes the datasets used in this study. Section 4 offers some insights into the nonparametric approach and compares the estimates with the site observations. Section 5 discusses issues related to the nonparametric approach, and Section 6 provides a conclusion.

2. Methodology

For a simple lumped system, when effects of unsteadiness, ice melt, photosynthesis, and advection can be neglected, the land surface energy balance equation can be written as [3]

$$(R_n - G) = H + LE, \quad (1)$$

where R_n is the net radiation, G is the soil heat flux, H is the sensible heat flux, and LE is the latent heat flux; $(R_n - G)$ is often called the available energy. For one dimension, sensible and latent heat fluxes are described in terms of flux-gradient relationships [19]:

$$H = \rho C_p \frac{T_s - T_a}{r_a}, \quad (2)$$

$$LE = \frac{\rho C_p e_s^* - e_a}{\gamma r_a + r_s}, \quad (3)$$

where ρ is the air density (kg/m^3), C_p is the specific heat of air at constant pressure ($1,013 \text{ Jkg}^{-1}\text{ }^\circ\text{C}^{-1}$), γ is the psychrometric constant ($\text{kPa } ^\circ\text{C}^{-1}$), T_s and T_a are the aerodynamic surface and air temperatures ($^\circ\text{C}$), e_s^* and e_a are the water vapor pressure at the evaporating surface and in the air (kPa),

r_a is the aerodynamic resistance (s/m), and r_s is the surface resistance (s/m).

Bowen [10] expressed the Bowen ratio (β) as

$$\beta = \frac{H}{LE}. \quad (4)$$

The Bowen ratio can be determined from the profile data of water vapor pressure and air temperature:

$$\beta = \gamma \frac{\Delta T}{\Delta e}, \quad (5)$$

where ΔT and Δe are air temperature and water vapor pressure differences at two heights within the boundary layer. If the available energy is known, the combination of (1) and (4) produces

$$LE = \frac{(R_n - G)}{1 + \beta}, \quad (6)$$

$$H = \frac{\beta (R_n - G)}{1 + \beta}.$$

The Penman-Monteith equation [11, 12] eliminates the aerodynamic surface temperature and yields the following equation:

$$LE = \frac{\Delta (R_n - G) + \rho_a C_p ((e_s - e_a) / r_a)}{\Delta + \gamma (1 + r_s / r_a)}, \quad (7)$$

where Δ is the slope of the saturation vapor pressure curve at air temperature ($\text{kPa } ^\circ\text{C}^{-1}$) and e_s is the saturation water vapor pressure at air temperature (kPa). The main feature of the Penman-Monteith equation is that it requires water vapor pressure, wind speed, and air temperature only at one level. All the parameters have been defined except for the surface resistance, which is to account for the evaporation deficit from unsaturated surfaces. Combining (1), (2), and (7), an expression for the aerodynamic surface temperature can be derived as follows [20]:

$$T_s = T_a + \frac{\gamma (1 + r_s / r_a) (r_a / \rho_a C_p) (R_n - G) - (e_s - e_a)}{\Delta + \gamma (1 + r_s / r_a)}. \quad (8)$$

This equation will be applied to the simulation analysis in the next section.

Liu et al. [18] proposed a nonparametric approach to estimate the actual ET. The derived equations are as follows:

$$LE = \frac{\Delta}{\Delta + \gamma} (R_n - G) - \epsilon \sigma (T_g^4 - T_a^4) + G \ln \left(\frac{T_g}{T_a} \right), \quad (9)$$

$$H = \frac{\gamma}{\Delta + \gamma} (R_n - G) + \epsilon \sigma (T_g^4 - T_a^4) - G \ln \left(\frac{T_g}{T_a} \right), \quad (10)$$

where T_g is the ground surface temperature (K), which is different from the aerodynamic surface temperature, ϵ is the surface emissivity, and σ is the Stefan-Boltzmann constant. The latent and sensible heat fluxes are functions of air temperature, soil heat flux, and net radiation. More importantly,

TABLE 1: Characteristics of the reference sites.

Site name	Country	Location	Köppen climate	Dominant land cover	ET observation systems
WC06	USA	41.93N, 93.75W	Hot wet summer/cold wet winter	Cropland (corn)	Eddy covariance
Yingke	China	38.85N, 100.41E	Hot summer/cold winter/dry year-round	Cropland (corn)	Eddy covariance
Tiger Bush Site	Niger	13.19N, 2.24E	Hot and dry year-round	Bare soil	Bowen system

this approach is relatively simple and all the parameters are measurable. The derivation and more details of this approach can be found in the paper by Liu et al. [18]. There are three terms in (9) and (10) where the first term is generally called equilibrium evaporation (denominated as E_{eq} in the following), the second term (in (10)) is denominated as N-P_{ST}, and the third term (in (9)) is denominated as N-P_{TT} in the following.

3. Data Description

Three experiment datasets were collected to evaluate the non-parametric approach. Specifically, data from the SMACEX (Soil Moisture-Atmosphere Coupling Experiment; [21]), WATER (Watershed Allied Telemetry Experimental Research; [22]) and HAPEX-Sahel (Hydrological and Atmospheric Pilot Experiment in the Sahel; [23]) experiments were used in this study. Table 1 lists the characteristics of the reference sites.

3.1. SMACEX. The Soil Moisture-Atmosphere Coupling Experiment was conducted in Iowa, USA, from June 19 through July 9 in 2002 and was designed to provide multiscale dataset of vegetation, soil, and atmospheric states [21, 24]. The primary objectives were to extend microwave soil moisture observations and retrieval algorithms to changing crop biomass conditions and to provide validation data for the Advanced Microwave Scanning Radiometer (AMSR) brightness temperature and soil moisture retrieval algorithms. The land cover in Walnut Creek watershed is primarily composed of corn and soybean. Twelve field sites with eddy covariance (EC) were deployed in the center of the study area. There were 6 corn sites and 6 soybean sites.

The data used in this study were obtained from the WC06 site. The tower was instrumented with sensors for measuring turbulent fluxes of water vapor and sensible heat, as well as net radiation and soil heat flux at 30 min intervals. Additional hydrometeorological observations included wind speed and direction, air temperature, vapor pressure, near-surface soil temperature, and moisture at 10 min intervals. In this study, the hydrometeorological data were resampled to 30 min to be compatible with heat flux measurements. Sensible and latent heat fluxes were adjusted by forcing the energy balance closure using the measured net solar radiation, soil heat flux, and Bowen ratio based on the approach suggested by Twine et al. [25]. The tower-based composite radiometric surface temperature was measured by Apogee infrared thermometers. Su et al. [24] corrected the data and applied them to evaluate the SEBS model. In this

study, the correction method proposed by Su et al. [24] was employed.

3.2. WATER. The Watershed Allied Telemetry Experimental Research (WATER) is a simultaneous airborne, satellite-borne, and ground-based remote sensing experiment taking place in the Heihe River Basin, the second largest inland river basin in the arid regions of northwest China. The mission of this experiment was to improve the observability, understanding, and predictability of hydrological and related ecological processes at a catchment scale. A detailed introduction to WATER can be found at <http://water.westgis.ac.cn/> or from the paper by Li et al. [22].

The observations from the Yingke station were collected in this study. The site is located in an oasis where the underlying cover is typical irrigated farmland. An Automatic Meteorological Station (AMS), a Soil Moisture and Temperature Measuring System (SMTMS), and an EC system were deployed at this site. Data from July 1 to July 15 in 2008 were collected in this study. Soil heat fluxes were estimated using the Thermal Diffusion Equation and Correction (TDEC) method proposed by Yang and Wang [26]. Surface temperature was estimated from the incoming and outgoing long-wave radiation measured with four component net radiometers. The surface emissivity was assumed to be 0.98 for the corn field. More detailed descriptions of the field observations can be found in the papers by Li et al. [22] and Song et al. [27].

3.3. HAPEX-Sahel. The HAPEX-Sahel experiment was undertaken in Niger, during 1991 and 1992. It aimed at improving the parameterization of land-surface-atmosphere interactions at the Global Circulation Model grid box scale [23]. Three supersites with detailed hydrometeorological studies were deployed in the 1° square experimental domain.

In this study, the bare soil evaporation data collected from the Southern Supersite during the intensive observation period (IOP) in 1992 were used. The latent and sensible heat fluxes were measured with a Bowen ratio system that was very close to the soil surface (0.05 m and 0.20 m). The area was completely bare soil. The system also had a net radiometer and two soil heat plates deployed in the same place. The surface temperature was measured by infrared thermometers operating in the range of 8 to 14 micrometers. Air temperature, wet bulb temperature, wind speed, rainfall, incoming long-wave radiation, incoming shortwave radiation, and reflected solar radiation over bare soil were observed by an automatic weather station. Detailed information on this dataset can be found in the paper by Wallace and Holwill

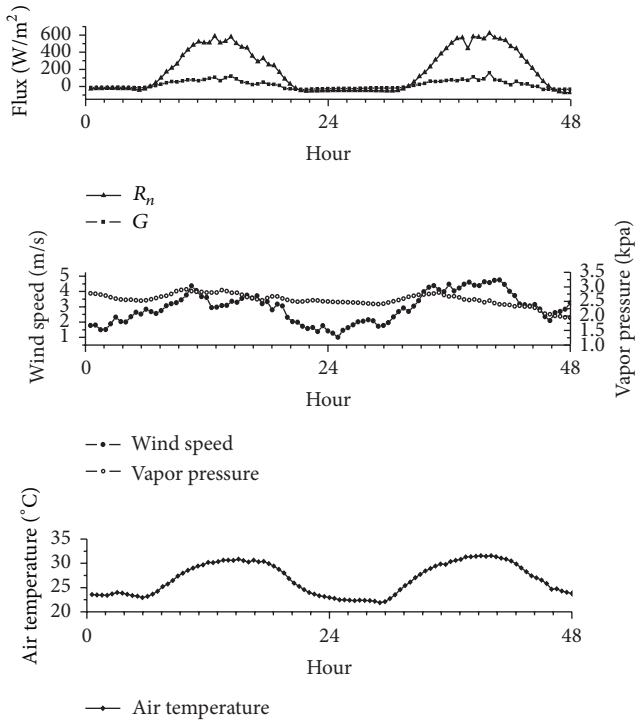


FIGURE 1: The diurnal variation of net radiation, soil heat flux, wind speed, vapor pressure, and air temperature for WC06 from DOY 172-173.

[28]. The period from DOY 260 to 280 of 1992 was chosen in this study. During this time, there was no rainfall and it was the dry season in this area. The surface temperature was corrected with incoming long-wave radiation, and the bare soil emissivity was assumed to be 0.98. The data were obtained from the HAPEX-Sahel information system (<http://www.cesbio.ups-tlse.fr/hapex/>).

4. Results

4.1. Simulation Analysis. Before the sites evaluation was undertaken, simulation analyses were carried out to compare the results derived from the nonparametric approach, the Penman-Monteith equation, and the Bowen ratio approach. Generally, two kinds of simulation were employed in this study. For the first one, the Penman-Monteith equation was compared with the nonparametric approach. To conduct this analysis, two days' (DOY 172 and 173) measurements from WC06 were selected. Figure 1 shows the diurnal variation of net radiation, soil heat flux, wind speed, vapor pressure, and air temperature for these two days. The observations included most parameters for the Penman-Monteith equation, except for surface resistance and aerodynamic resistance. To facilitate this analysis, the aerodynamic resistance was estimated using $r_a = 208/u$, where u represents the wind speed in m/s and r_a is in s/m. This simple equation is often used to estimate the aerodynamic resistance for the reference grass surface [13]. The simulation process is as follows: at

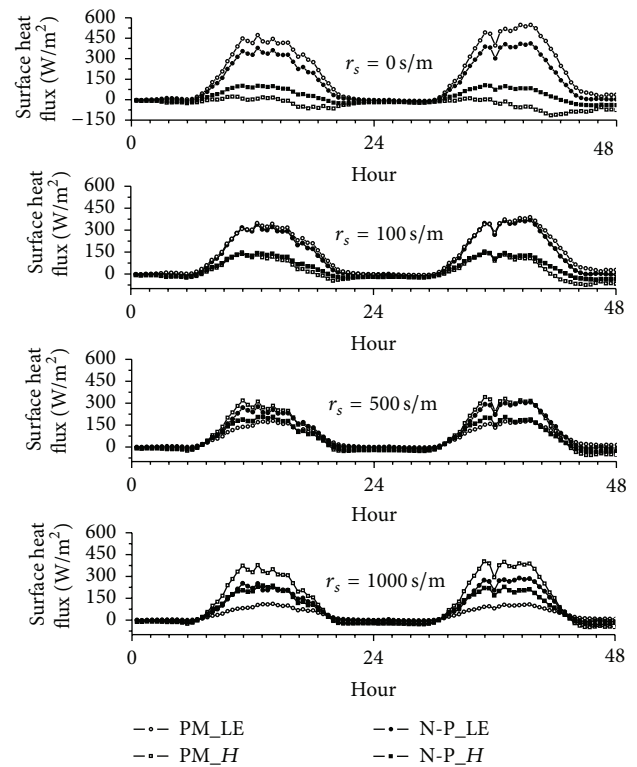


FIGURE 2: Comparison of surface heat fluxes derived from Penman-Monteith equation and the nonparametric approach.

first, the surface resistance was set as a constant value; then the latent and sensible heat fluxes can be estimated with the Penman-Monteith equation; subsequently, the aerodynamic surface temperature can be derived from (8); finally, assuming the ground surface temperature was equal to the aerodynamic surface temperature and the surface emissivity is equal to 0.98, the latent and sensible heat fluxes can be estimated based on the nonparametric approach. It is worth noting that the aerodynamic surface temperature is actually different from the ground surface temperature. The difference between the aerodynamic surface temperature and the ground surface temperature is significant over the sparse vegetation area [29, 30]. In this study, it was assumed that this simulation was carried out over dense grassland; therefore, the difference between the two can be neglected. Four scenario analyses were undertaken with the surface resistance set as 0, 100, 500, and 1000 s/m, respectively. Figure 2 presents the comparison between the estimates from Penman-Monteith equation and the surface heat fluxes based on the nonparametric approach. For $r_s = 0$ s/m, which is for the dense grassland after a rainfall event, the grassland evaporates at the potential rate. The latent heat flux estimated by the Penman-Monteith equation is greater than the nonparametric approach. At the same time, the sensible heat flux estimated with Penman-Monteith is lower than the nonparametric approach. The largest difference between the estimates from the two approaches is about 100 W/m^2 . For

$r_s = 100 \text{ s/m}$, this is generally the case for a well-irrigated grassland. The latent and sensible heat fluxes estimated with the two approaches show a good agreement. The surface heat fluxes estimated from two approaches are nearly equal under such conditions, for $r_s = 500 \text{ s/m}$, which represents a water-stressed grassland. The latent heat flux estimated by the nonparametric approach is shown to be greater than that from the Penman-Monteith equation. The largest difference is about 120 W/m^2 . On the contrary, the sensible heat flux based on the nonparametric approach is smaller than the Penman-Monteith-based estimates. For $r_s = 1000 \text{ s/m}$, which stands for a grassland under a severe drought, the estimates of latent heat flux from the nonparametric approach are shown to be significantly greater than Penman-Monteith-based estimates. Meanwhile, the estimates of sensible heat flux from the nonparametric approach are shown to be much lower than the Penman-Monteith-based estimates. The difference of the latent heat flux derived from the two methods is as large as 160 W/m^2 . The analyses above indicated the nonparametric approach and the Penman-Monteith equation may have great differences under dry circumstances. For the second one, the Bowen approach was compared with the nonparametric approach. The net radiation, air temperature, soil heat flux, and aerodynamic resistance need to be set at first. The values for net radiation, air temperature, and soil heat flux were set as 450 W/m^2 , 25°C , and 135 W/m^2 based on the measurements at 11:00 am from the WC06 site. The aerodynamic resistance was set as 70 s/m , which is a typical value for grassland. Zhang et al. [31] pointed out that soil moisture availability and the Bowen ratio have a certain relationship. Under the same conditions of net radiation and soil heat flux, high soil moisture availability corresponds to a low Bowen ratio (see Figure 1 in their paper). Assuming the Bowen ratio ranged from 0 to 10 with the step of 0.2, this may represent grasslands under different soil moisture conditions under the same radiation environment. The latent and sensible heat fluxes can be derived based on (6). Similar to the first simulation, the aerodynamic surface temperature was estimated using (8). It is still assumed that the aerodynamic surface temperature is an approximation to the ground surface temperature and the emissivity was set as 0.98, and then the latent and sensible heat fluxes can be derived from the nonparametric approach. Figure 3 presents the comparison of latent heat flux and sensible heat flux derived from the Bowen ratio approach and the nonparametric approach. For a Bowen ratio smaller than 0.6, the latent heat flux derived from the Bowen ratio approach is shown to be greater than that derived from the nonparametric approach. When the Bowen ratio is greater than 0.8, the nonparametric approach-based latent heat flux is continuously larger than the estimates based on the Bowen ratio approach. For the sensible heat flux, the results are completely opposite. When the Bowen ratio is equal to 0.6, the estimates from both approaches are nearly equal. The difference between the two approaches is about 100 W/m^2 for the Bowen ratio with 10. Through the two types of simulations above, the results indicates that the nonparametric approach may greatly overestimate latent heat flux under dry conditions.

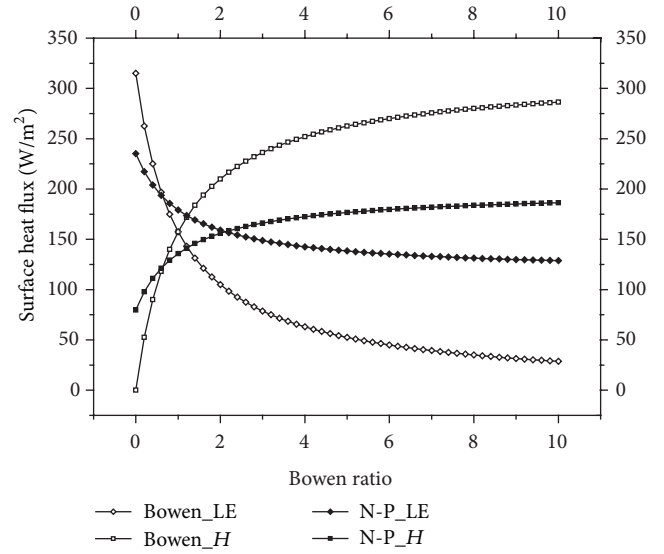


FIGURE 3: Comparison of latent heat flux and sensible heat flux derived from the Bowen ratio approach and the nonparametric approach.

TABLE 2: Quantitative computations of model performance with observations from three sites.

Experiments	SMACEX		WATER		HAPEX-Sahel	
	WC06	Yingke station	Tiger Bush Site	LE	H	LE
N	844	844	344	343	1441	1441
MAD	50.17	50.17	35.17	30.49	47.07	47.07
RMSD	58.26	58.26	51.11	42.45	67.54	67.54
E	0.9	-0.419	0.94	0.58	-9.43	0.59
Slope	0.896	0.844	0.799	0.869	2.004	0.547
Intercept	-30.46	49.17	10.41	21.54	30.64	-9.352
R-Square	0.979	0.645	0.989	0.71	0.447	0.921

4.2. Site Evaluation. In this section, the nonparametric approach was evaluated with site observations. The Nash-Sutcliffe coefficient (E) was used in this study to qualify the model performance. Nash-Sutcliffe coefficient ranges from $-\infty$ to 1. Essentially, the closer to 1 it is, the more accurate the model is. Table 2 lists the statistical computations for the estimates based on the nonparametric approach at three different sites. Figure 4 presents the time series comparison of the surface heat fluxes estimated by the nonparametric approach with the measurements from the eddy covariance system at the WC06 site. The WC06 site, located in the central part of the United States, has a climate with a hot, wet summer. The estimates of the latent heat flux were found to have a good agreement with the observations at this site. The nonparametric approach shows a slightly underestimated latent heat flux. There were 844 samples in the comparison; the slope and the intercept of the linear regression between the two were 0.896 and -30.46 W/m^2 . The mean absolute deviation (MAD) and the root mean

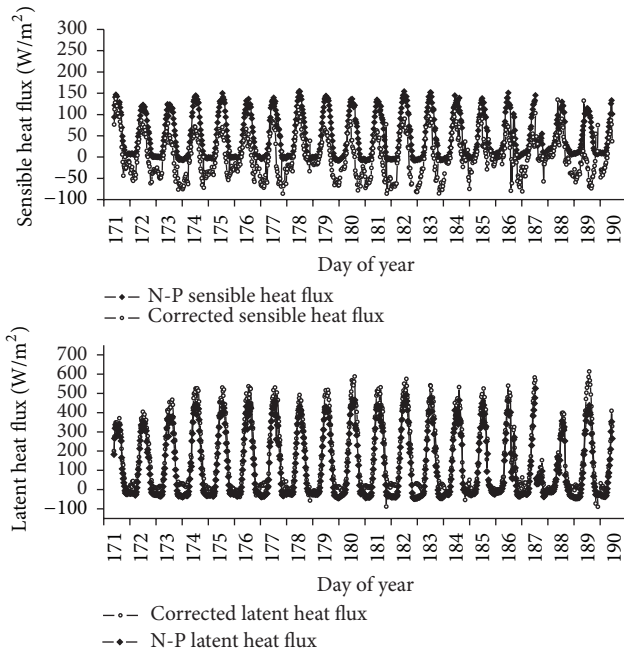


FIGURE 4: Time series comparison of the surface heat fluxes estimated by the nonparametric approach with the measurements from the eddy covariance system at the WC06 site. (The gap in the figure was due to lack of observations.)

square deviation (RMSD) were 50.17 W/m^2 and 58.26 W/m^2 , respectively. The Nash-Sutcliffe coefficient (E) was 0.9. However, the approach seems to overestimate the sensible heat flux for about 60 W/m^2 . The E was -0.419 . The MAD and the RMSD were the same as those for the latent heat flux due to the complementary relationship with the sensible and latent heat fluxes. The corresponding slope and the intercept were 0.844 and 49.17 W/m^2 .

A further evaluation was undertaken at the Yingke station. The Yingke station is located in the northwest part of China and the climate is dry year-round, with a hot summer and a cold winter. Figure 5 shows a comparison of the surface heat fluxes estimated by the nonparametric approach with the eddy covariance observations at this site. The results indicated that the nonparametric approach can effectively characterize the diurnal variations of the latent and sensible heat fluxes at this site. For the latent heat flux estimates, the slope and intercept of the regression line are 0.799 and 10.41 W/m^2 . This comparison included 344 samples. The E was 0.94. The MAD and RMSD were 35.17 W/m^2 and 51.11 W/m^2 , respectively. For the sensible heat flux estimates, the corresponding slope and the intercept were 0.869 and 21.54 W/m^2 . The E was 0.58. The MAD and RMSD were 30.49 W/m^2 and 42.45 W/m^2 , respectively.

The evaluations above were both carried out in cropland and the evaluations indicated that the nonparametric approach can provide a good estimate of latent heat flux for these conditions. In this part, a further evaluation was undertaken at the Tiger Bush Site, which is covered by bare soil and has a hot and dry climate year-round. Figure 6

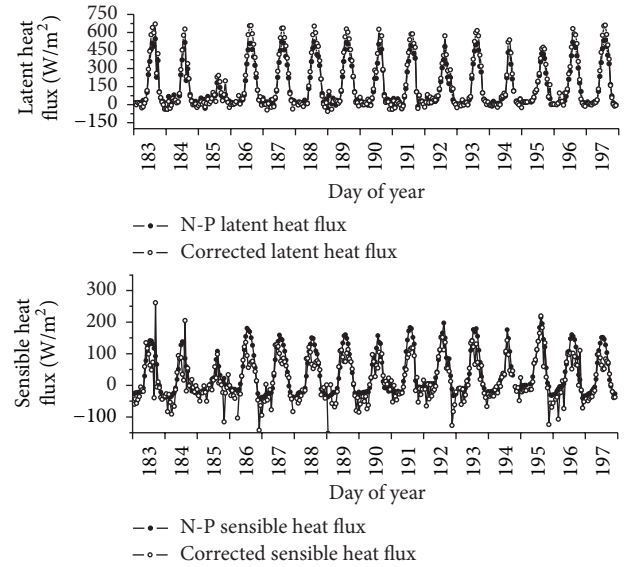


FIGURE 5: Comparison of the surface heat fluxes estimated by the nonparametric approach with the measurements from the eddy covariance system at Yingke site.

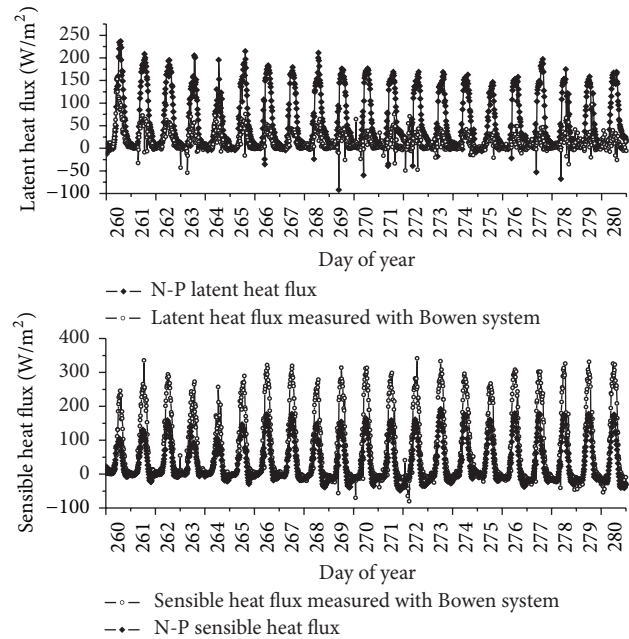


FIGURE 6: Comparison of the surface heat fluxes estimated by the nonparametric approach with the measurements from the Bowen system at the Tiger Bush Site.

presents the time series comparison of the surface heat flux estimates and the observations at this site. It was found that the nonparametric approach would greatly overestimate the latent heat flux. The difference between the estimates and the observations can be as large as 130 W/m^2 . On the contrary, the nonparametric approach greatly underestimated the sensible heat flux. The statistical computations were listed in Table 2. There were 1441 samples in the comparison. The MAD and

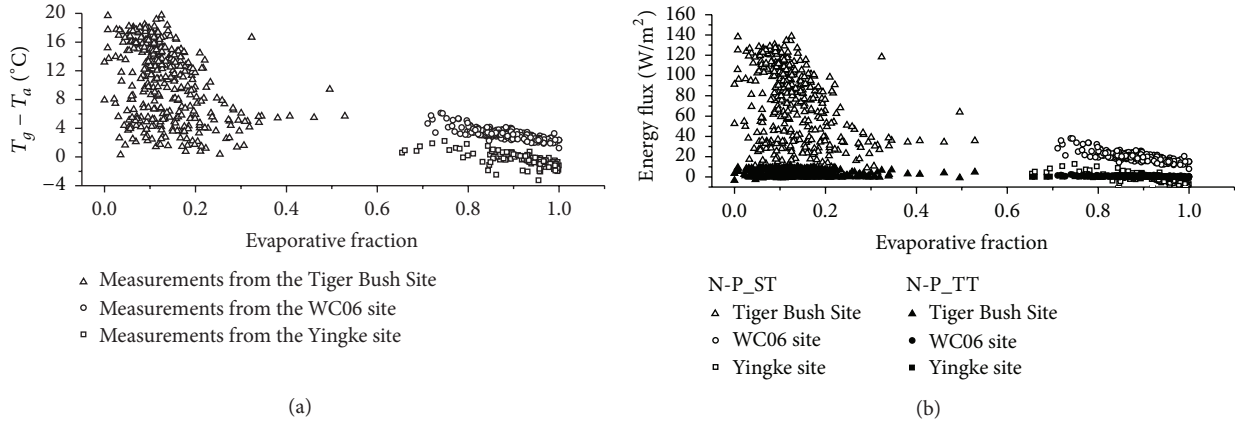


FIGURE 7: (a) Evaporative fraction versus $(T_g - T_a)$; (b) evaporative fraction versus two terms (N-P_ST and N-P_TT) of the nonparametric approach.

the RMSD were $47.07 W/m^2$ and $67.54 W/m^2$, respectively. For the LE estimates, the E was -9.43 . The slope and the intercept of the fitted line were 2.0 and $30.64 W/m^2$. For the sensible heat flux, the E was 0.59 ; the slope and the intercept were 0.547 and $-9.35 W/m^2$. The statistical computations quantitatively indicated that the nonparametric approach would greatly overestimate LE and underestimate H at this site. The simulations in Section 4.1 compared the nonparametric approach with the Penman-Monteith equation and the Bowen ratio approach. The results demonstrated that the nonparametric approach has greater estimates than the Penman-Monteith equation and the Bowen ratio approach under dry conditions. The evaluation at the Tiger Bush Site further confirmed that this approach would greatly overestimate the latent heat flux under dry conditions.

4.3. Comparison between the Equilibrium Evaporation and the Nonparametric Approach. Sections 4.1 and 4.2 evaluated the nonparametric approach with a model simulation and site observations. The results firmly indicated that the nonparametric approach would greatly overestimate ET under dry conditions. Liu et al. [18] evaluated this approach with observations collected from 26 eddy covariance sites and they found an absolute difference of 10.3 ± 20.2 (mean \pm standard deviation) W/m^2 for latent heat flux. In this study, we also found this approach to provide promising LE estimates for two crop sites, namely, Yingke and WC06 station. Soil moisture may be one of the most important factors that influence the performance of this approach. In this section, the nonparametric approach will be further analyzed. The evaporative fraction, the ratio between LE and available energy ($R_n - G$), is a good indicator of water availability for evaporation and will be used in the following analysis. To eliminate uneven measurements at night time, the observations between 10:00 and 16:00 (in local time) from all three sites were selected. The difference between ground surface temperature and air temperature ($T_g - T_a$), evaporative fraction, and the three terms (E_{eq} , N-P_ST, and N-P_TT) of the nonparametric approach were computed for

every measurement record. Figure 7 shows the scatter plot of evaporative fraction versus $(T_g - T_a)$ and evaporative fraction versus two terms of the nonparametric approach. There are generally three point clusters in Figure 7(a), which correspond to the measurements from the three sites. For the Tiger Bush Site, the evaporative fraction is smaller than 0.4 , and most points located in the range of $0-0.3$, indicating low soil moisture availability for evaporation. For the other two sites, the evaporative fraction is greater than 0.65 , which indicates ample water for evaporation. $(T_g - T_a)$ is quiet large in the Tiger Bush Site with small evaporative fraction values, while it shows small values (lower than $4^\circ C$) at the Yingke and the WC06 sites with large evaporative fraction values. Figure 7(b) shows N-P_ST and N-P_TT with varying evaporative fraction values. It was found that N-P_ST shows similar point clusters as that in Figure 7(a). For the Tiger Bush Site, N-P_ST ranged from 20 to $140 W/m^2$. For the Yingke and WC06 sites, N-P_ST was generally smaller than $40 W/m^2$. N-P_TT, the third term in (9), is smaller than $15 W/m^2$ at all three sites. This indicates that this term has little function in the nonparametric approach. From the analysis above, it is found that N-P_TT and N-P_ST have relatively small values for wet conditions with high evaporative fraction values. In addition, N-P_TT and N-P_ST have the different signs in (9). This may imply that the nonparametric approach is very close to the equilibrium evaporation equation under wet conditions. The results shown in Figure 8 support this deduction. For the Yingke and WC06 sites, the difference between the estimates from nonparametric approach and the estimates from the equilibrium evaporation was relatively small. However, the difference is relatively large at the Tiger Bush Site which has small evaporative fraction values. Figure 8 provides two other differences, namely, the difference between the estimates from the nonparametric approach and the site observations, as well as the difference between the estimates from the equilibrium evaporation and the site observations. Figure 9 provides the comparison between observed latent heat fluxes with the estimates from the equilibrium evaporation. For the measurements from the Yingke and WC06 sites, most of

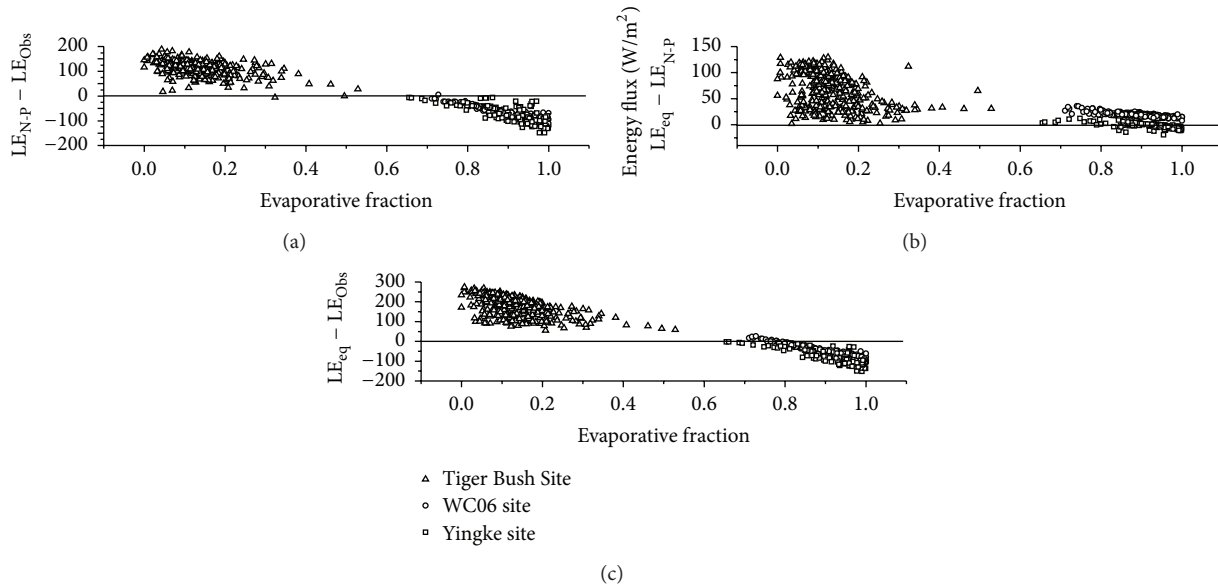


FIGURE 8: (a) The difference between the estimates from the nonparametric approach and the site observations; (b) the difference between the estimates from the nonparametric approach and the estimates from the equilibrium evaporation; (c) the difference between the estimates from the equilibrium evaporation and the site observations.

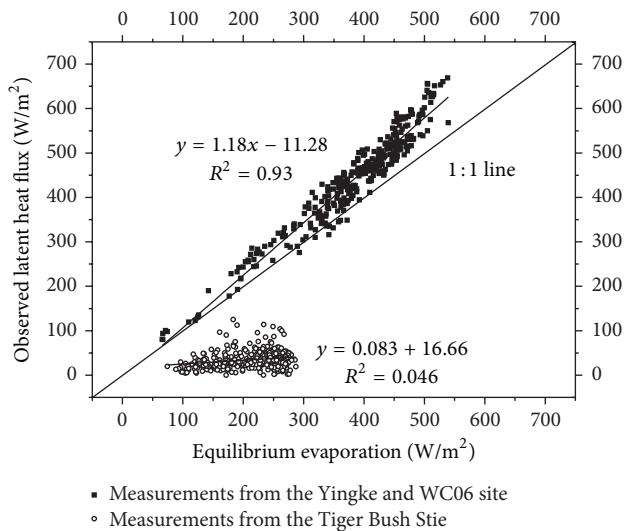


FIGURE 9: Estimates from the equilibrium evaporation versus the sites observations.

the points were close to the 1:1 line; the slope and the intercept of the fitted line were 1.18 and -11.28 W/m^2 . This indicated that the equilibrium evaporation is a good approximate for the latent heat flux for the Yingke and WC06 sites with high evaporative fraction values. However, this does not hold for the Tiger Bush Site, which has relatively small evaporative fraction values. The slope and the intercept of the fitted line were 0.083 and 16.66 W/m^2 . This corresponded to the study by Denmead and McIlroy [32], who suggested that the equilibrium evaporation might be closely approximate to the actual crop evaporation.

5. Discussion

Actual ET estimation has long been a difficult problem for hydrometeorologists. The nonparametric approach proposed by Liu et al. [18] is attractive, because the solution is simple and without parameterization of a transfer coefficient. In our study, the nonparametric approach was evaluated using both model simulation and site observations. The simulation indicated that this approach would greatly overestimate ET under dry conditions. It is worthwhile to note that the simulation analysis may present two minor problems. First, the aerodynamic surface temperature and the ground surface temperature are not equal; this has already been reported by many researchers [29, 30]. However, the difference is not significant over dense cropland. Secondly, the soil heat flux in the simulation analysis was used as a constant value in comparison with the Bowen ratio approach. This may not be realistic in real conditions. The overestimation of the nonparametric approach under dry conditions indicated by the simulation analysis was quite clear, and this was further confirmed by the Tiger Bush Site observations in Section 4.2.

The site evaluations indicated that the nonparametric approach could provide promising estimates for the Yingke and WC06 sites, but it would fail for the Tiger Bush Site, which was relatively dry. Liu et al. [18] evaluated the nonparametric approach with observations from 26 sites and found that this approach worked well at most sites. In 3 of 26 sites, they found that the performance of the nonparametric approach was relatively poor (see Table 2 in their paper). In the analysis of the reason for the bad performance for three sites, they pointed out that these sites had no common features in climate conditions. In this study, both model simulation and in situ evaluation at the Tiger Bush Site reveal that the nonparametric approach would greatly overestimate

ET under dry conditions. In addition, Liu et al. [18] pointed out that the performance of the nonparametric approach is comparable to the Penman-Monteith approach and the Bowen ratio approach with 2 site observations. However, the evaluation at the Tiger Bush Site (actual ET observed with the Bowen approach) in this study does not support this statement.

Every term in the nonparametric approach was further analyzed in Section 4.3. It was found that the nonparametric approach is very close to the equilibrium evaporation equation at the Yingke and WC06 sites, as the second term and the third term are relatively small and have different signs to offset each other. However, this is not the case for the Tiger Bush Site, as the actual ET is mainly controlled by limited soil moisture under dry circumstances. In fact, Denmead and McIlroy [32] have suggested that the equilibrium evaporation may serve as a simple measure for actual ET. This suggestion is further supported by many field experiments [3, 33, 34]. A clearer description of this problem can be found in the book by Monteith [20], as cropland usually has moderate surface resistance, and the equilibrium evaporation would be a close approximation of the actual crop evaporation. The scatter plot in Figure 9 also provides a solid support. This may be an implication of the good performance of the nonparametric approach at the 23 sites in Liu's paper and 2 sites in this paper. The application of the nonparametric approach needs more caution under dry conditions. In addition, it is worthwhile to point out that the deviation of the nonparametric approach needs more thorough investigation, for the third term in the equation has little function.

Soil moisture plays an important role in drylands ecosystems [35]. In drylands, soil moisture plays a dominant role in hydrological processes. Drylands cover more than 40 percent of Earth's land surface and are inhabited by nearly 40 percent of the world's population [36]. However, there have still been insufficient observation sites in sparsely vegetated areas. Further research on the drylands hydrological process is imperative.

6. Conclusion

In this study, a critical evaluation of the nonparametric approach was undertaken. Both the model simulation and the site evaluation at Tiger Bush Site indicated that this approach would greatly overestimate ET under dry conditions. However, two crop site evaluations have shown that this approach can achieve good performance. Further analysis revealed that the nonparametric approach is very close to the equilibrium evaporation equation, which approaches the actual ET under wet conditions. In addition, it has been found that the third term has little influence on the results. The evaluations indicate that the application of this approach needs to be cautious and avoided in dry conditions.

Conflict of Interests

The authors declare no conflict of interests.

Authors' Contribution

Yongmin Yang proposed and developed the research design, paper writing, and results interpretation. Hongbo Su supervised all the work that has been done by the first author and revised the paper extensively. Jianwei Qi did part of the data analysis and revised the paper.

Acknowledgments

The authors are very thankful to the researchers in SMACEX, WATER, and HAPEX-Sahel for the data acquisition and sharing. This work is supported jointly by the Project of National Natural Science Foundation of China (41171286) and the High Resolution Earth Observation System Program of China (no. 08-Y30B07-9001-13/15).

References

- [1] C. Folke, S. Carpenter, T. Elmqvist, L. Gunderson, C. S. Holling, and B. Walker, "Resilience and sustainable development: building adaptive capacity in a world of transformations," *Ambio*, vol. 31, no. 5, pp. 437–440, 2002.
- [2] J. G. Liu, T. Dietz, S. R. Carpenter et al., "Complexity of coupled human and natural systems," *Science*, vol. 317, no. 5844, pp. 1513–1516, 2007.
- [3] W. Brutsaert, *Evaporation into the Atmosphere: Theory, History, and Applications*, Springer, New York, NY, USA, 1982.
- [4] D. M. Lawrence, P. E. Thornton, K. W. Oleson, and G. B. Bonan, "The partitioning of evapotranspiration into transpiration, soil evaporation, and canopy evaporation in a GCM: impacts on land-atmosphere interaction," *Journal of Hydrometeorology*, vol. 8, no. 4, pp. 862–880, 2007.
- [5] W. Brutsaert, *Hydrology: An Introduction*, Cambridge University Press, 2005.
- [6] C. H. Priestley and R. J. Taylor, "On the assessment of surface heat flux and evaporation using large-scale parameters," *Monthly Weather Review*, vol. 100, no. 2, pp. 81–92, 1972.
- [7] W. J. Shuttleworth, "Putting the 'vap' into evaporation," *Hydrology and Earth System Sciences*, vol. 11, no. 1, pp. 210–244, 2007.
- [8] J. Dalton, "Experimental essays on the constitution of mixed gases. On evaporation and the expansion of gases by heat," *Memoirs and Proceedings of the Manchester Literary & Philosophical Society*, vol. 5, pp. 535–602, 1802.
- [9] A. Fick, "Ueber diffusion," *Annalen der Physik und Chemie*, vol. 170, no. 1, pp. 59–86, 1855.
- [10] I. S. Bowen, "The ratio of heat losses by conduction and by evaporation from any water surface," *Physical Review*, vol. 27, no. 6, pp. 779–787, 1926.
- [11] H. L. Penman, "Natural evaporation from open water, bare soil and grass," *Proceedings of the Royal Society of London Series A: Mathematical, Physical and Engineering Sciences*, vol. 193, no. 1032, pp. 120–145, 1948.
- [12] J. L. Monteith, "Evaporation and environment," in *The State and Movement of Water in Living Organisms, Proceedings of the 19th Symposia of the Society for Experimental Biology*, Swansea, UK, Cambridge University Press, 1965.
- [13] R. G. Allen, L. Pereira, D. Raes, and M. Smith, *FAO Irrigation and Drainage Paper No. 56. Crop Evapotranspiration (Guidelines for Computing Crop Water Requirements)*, FAO, Rome, Italy, 1998.

- [14] F. I. Morton, "Evaporation research—a critical review and its lessons for the environmental sciences," *Critical Reviews in Environmental Science and Technology*, vol. 24, no. 3, pp. 237–280, 1994.
- [15] K. C. Wang and R. E. Dickinson, "A review of global terrestrial evapotranspiration: observation, modeling, climatology, and climatic variability," *Reviews of Geophysics*, vol. 50, no. 2, 2012.
- [16] K. Yang, M. Rasmy, S. Rauniyar et al., "Initial CEOP-based review of the prediction skill of operational general circulation models and land surface models," *Journal of the Meteorological Society of Japan*, vol. 85, pp. 99–116, 2007.
- [17] M. R. Raupach, "Influences of local feedbacks on land-air exchanges of energy and carbon," *Global Change Biology*, vol. 4, no. 5, pp. 477–494, 1998.
- [18] Y. B. Liu, T. Hiyama, T. Yasunari, and H. Tanaka, "A non-parametric approach to estimating terrestrial evaporation: validation in eddy covariance sites," *Agricultural and Forest Meteorology*, vol. 157, pp. 49–59, 2012.
- [19] B. D. Tanner, "Use requirements for Bowen ratio and eddy correlation determination of evapotranspiration," in *Planning Now for Irrigation and Drainage in the 21st Century*, R. DeLynnHay, Ed., p. 782, ASCE, 1988.
- [20] J. L. Monteith, *Vegetation and the Atmosphere, Volume 1 Principles*, Academic Press, New York, NY, USA, 1975.
- [21] W. P. Kustas, J. L. Hatfield, and J. H. Prueger, "The soil moisture-atmosphere coupling experiment (SMACEX): background, hydrometeorological conditions, and preliminary findings," *Journal of Hydrometeorology*, vol. 6, no. 6, pp. 791–804, 2005.
- [22] X. Li, Z. Li, M. Ma et al., "Watershed allied telemetry experimental research," *Journal of Geophysical Research D: Atmospheres*, vol. 114, no. 22, Article ID D22103, 2009.
- [23] J. P. Goutorbe and J. P. Goutorbe, "Hapex-Sahel - a Large-Scale Study of Land-Atmosphere Interactions in the Semiarid Tropics," *Annales Geophysicae-Atmospheres Hydrospheres and Space Sciences*, vol. 12, no. 1, pp. 53–64, 1994.
- [24] H. Su, M. F. McCabe, E. F. Wood, Z. Su, and J. H. Prueger, "Modeling evapotranspiration during SMACEX: comparing two approaches for local- and regional-scale prediction," *Journal of Hydrometeorology*, vol. 6, no. 6, pp. 910–922, 2005.
- [25] T. E. Twine, W. P. Kustas, J. M. Norman et al., "Correcting eddy-covariance flux underestimates over a grassland," *Agricultural and Forest Meteorology*, vol. 103, no. 3, pp. 279–300, 2000.
- [26] K. Yang and J. M. Wang, "A temperature prediction-correction method for estimating surface soil heat flux from soil temperature and moisture data," *Science in China, Series D: Earth Sciences*, vol. 51, no. 5, pp. 721–729, 2008.
- [27] Y. Song, J. Wang, K. Yang et al., "A revised surface resistance parameterisation for estimating latent heat flux from remotely sensed data," *International Journal of Applied Earth Observation and Geoinformation*, vol. 17, no. 1, pp. 76–84, 2012.
- [28] J. S. Wallace and C. J. Holwill, "Soil evaporation from tiger-bush in south-west Niger," *Journal of Hydrology*, vol. 188–189, no. 1–4, pp. 426–442, 1997.
- [29] W. P. Kustas, B. J. Choudhury, M. S. Moran et al., "Determination of sensible heat flux over sparse canopy using thermal infrared data," *Agricultural and Forest Meteorology*, vol. 44, no. 3–4, pp. 197–216, 1989.
- [30] J. B. Stewart, W. P. Kustas, K. S. Humes, W. D. Nichols, M. S. Moran, and H. A. de Bruin, "Sensible heat flux-radiometric surface temperature relationship for eight semiarid areas," *Journal of Applied Meteorology*, vol. 33, no. 9, pp. 1110–1117, 1994.
- [31] R. Zhang, X. Sun, Z. Zhu, H. Su, and X. Tang, "A remote sensing model for monitoring soil evaporation based on differential thermal inertia and its validation," *Science in China, Series D: Earth Sciences*, vol. 46, no. 4, pp. 342–355, 2003.
- [32] O. T. Denmead and I. C. McIlroy, "Measurements of non-potential evaporation from wheat," *Agricultural Meteorology*, vol. 7, no. 4, pp. 285–302, 1970.
- [33] J. A. Davies, "Actual, potential and equilibrium evaporation for a beanfield in southern Ontario," *Agricultural Meteorology*, vol. 10, no. 4–5, pp. 331–348, 1972.
- [34] R. G. Wilson and W. R. Rouse, "Moisture and temperature limits of the equilibrium evapotranspiration model," *Journal of Applied Meteorology*, vol. 11, no. 3, pp. 436–442, 1972.
- [35] L. Wang, P. D'Odorico, J. P. Evans et al., "Dryland ecohydrology and climate change: critical issues and technical advances," *Hydrology and Earth System Sciences*, vol. 16, no. 8, pp. 2585–2603, 2012.
- [36] UNEP, *World Atlas of Desertification*, United Nations Environment Programme (UNEP), Nairobi, Kenya, 1992.

Research Article

A Comparison of Three Gap Filling Techniques for Eddy Covariance Net Carbon Fluxes in Short Vegetation Ecosystems

Xiaosong Zhao¹ and Yao Huang²

¹Key Laboratory of Watershed Geographic Sciences, Nanjing Institute of Geography and Limnology, Chinese Academy of Sciences, Nanjing 210008, China

²State Key Laboratory of Vegetation and Environmental Change, Institute of Botany, Chinese Academy of Sciences, Beijing 100093, China

Correspondence should be addressed to Yao Huang; huangyao@ibcas.ac.cn

Received 9 March 2015; Accepted 17 May 2015

Academic Editor: Marcos Heil Costa

Copyright © 2015 X. Zhao and Y. Huang. This is an open access article distributed under the Creative Commons Attribution License, which permits unrestricted use, distribution, and reproduction in any medium, provided the original work is properly cited.

Missing data is an inevitable problem when measuring CO₂, water, and energy fluxes between biosphere and atmosphere by eddy covariance systems. To find the optimum gap-filling method for short vegetations, we review three-methods mean diurnal variation (MDV), look-up tables (LUT), and nonlinear regression (NLR) for estimating missing values of net ecosystem CO₂ exchange (NEE) in eddy covariance time series and evaluate their performance for different artificial gap scenarios based on benchmark datasets from marsh and cropland sites in China. The cumulative errors for three methods have no consistent bias trends, which ranged between -30 and +30 mgCO₂ m⁻² from May to October at three sites. To reduce sum bias in maximum, combined gap-filling methods were selected for short vegetation. The NLR or LUT method was selected after plant rapidly increasing in spring and before the end of plant growing, and MDV method was used to the other stage. The sum relative error (SRE) of optimum method ranged between -2 and +4% for four-gap level at three sites, except for 55% gaps at soybean site, which also obviously reduced standard deviation of error.

1. Introduction

Eddy covariance technique to measure CO₂, water, and energy fluxes between biosphere and atmosphere is widely spread and used in various regional networks [1]. At present, over 600 tower sites are operating on a long-term and continuous basis around the world, covering different climate conditions and land use and land cover changes, some of them running continuously for more than 10 years (<http://fluxnet.ornl.gov/>). However, missing or rejected data in these measurements is a unavoidable problem due to equipment failures (system/sensor breakdown), maintenance and calibration, spikes in the raw data, and physical and biological constraints (e.g., storms, hurricanes, and nonoptimal wind directions) [2]. In general, about 17–50% of the observations in net ecosystem CO₂ exchange (NEE) are reported as missing or rejected at FluxNet sites [3]. The gaps in observed data cause at least three problems: (1) difficulty in

annual estimation of NEE, (2) biased relationships between NEE with climatic variables, and (3) low quality data for modeling validation [2].

To accurately calculate annual values of NEE at sites, gap-filling to account for the missing data is imperative. The commonly used methods for filling missing data include mean diurnal variation (MDV) [3], look-up table (LUT) [3], nonlinear regression (NLR) [3–5], marginal distribution sampling [6], multiple imputation model [7], artificial neural network [8–11], and terrestrial biosphere model [12]. This diversity hinders synthesis activities because the biases and uncertainties associated with each technique are unknown [13, 14].

In a comprehensive study, Falge et al. [3] compared three methods including MDV, LUT, and NLR on the annual sum of NEE for 28 datasets from 18 FluxNet sites and found that the differences in annual NEE estimation by different gap-filling methods ranged from -45 to 200 gC m⁻² per year.

Their study also emphasized the importance of the method of standardization during the data postprocessing phase, so comparable data can be obtained to address intercomparisons across different ecosystems, climatic conditions, and multiple years. Richardson and Hollinger [15] quantified the uncertainties in annual NEE with a simple model using data assimilation techniques that are due both to random measurement error and to gap filling, including the additional uncertainty that can be attributed to long gaps and the relationship between gap length and uncertainty in NEE. The CO₂ flux data come from a coniferous, two deciduous, two mixed species, and two mediterranean sites. Moffat et al. [9] reviewed 15 techniques for estimating missing values of NEE in eddy covariance time series and evaluate their performance for different artificial gap scenarios based on a set of 10 benchmark datasets from six forested sites in Europe which is the same with Richardson and Hollinger [15]. Papale et al. [2] introduced a new standardized set of corrections and assessed the uncertainties associated with these corrections for eight different forest sites in Europe with a total of 12 yearly datasets.

However, most comparison works about gap-filling methods were objected to tall vegetation, that is, forests. Less research focused on short vegetation, that is, croplands or marshlands. The vegetation structure for short vegetation changes more rapidly in the growing season, which may affect ability of gap-filling methods. So, it is important to evaluate the performance of gap-filling methods and search the optimum methods for short vegetation.

In this study, we reviewed three methods (MDV, LUT, and NLR) and applied the techniques to a set of benchmark datasets from marshland and croplands (rice and soybean) in China. Artificial gaps were added to observed NEE time series based on Falge et al. [3], and the ability of different gap-filling techniques to replicate the missing data was evaluated using statistical analysis. The objective of this paper is to find the optimum method for short vegetation.

2. Methods

2.1. Data Basis. For this analysis, we used half-hourly eddy flux measurements of the net ecosystem exchange of CO₂ from three different ecosystem types. As case studies, we chose CO₂ flux data from May to October in 2005 from marshland and agriculture (rice and soybean cropland) sites in the Sanjiang Plain. The marshland site locates at (47°35′N, 133°31′E), the field areas are approximately 105 ha. The rice and soybean site locate approximately 1.5 km west and 500 m north to the marshland, respectively. The field areas are approximately thousands of hectares for rice site and 25 ha for soybean site. The altitude is 55.4–57.9 m. The more detailed information is available in Zhao et al. [16].

The EC system consisted of a triaxial sonic anemometer (CAST3, Campbell Scientific, USA) and a fast response open-path CO₂/H₂O infrared gas analyzer (Li-7500, LiCor Inc., USA). The meteorological parameters including air humidity and air temperature, wind speed, precipitation, soil temperature, and water content were measured [16]. Raw data acquired at 10 Hz were processed using the postprocessing,

TABLE 1: Percentages of original gaps in NEE measurements.

Flux site	Daytime		Nighttime		All time	
	<i>N</i>	Gap (<i>P</i> %)	<i>N</i>	Gap (<i>P</i> %)	<i>N</i>	Gap (<i>P</i> %)
Marsh site	4583	18.4%	2953	36.2%	7536	25.4%
Rice site	4804	12.4%	3212	26.7%	8016	18.2%
Soybean site	4804	15.0%	3212	28.7%	8016	20.5%

The *N* is the total number of data for daytime, nighttime, and all the time. The *P*% is the percentage of gaps for daytime, nighttime, or all the time.

TABLE 2: The number and percentage of friction velocity (u^*) filtered data in artificial datasets.

Flux site	u^* correction			
	35% gap	45% gap	55% gap	65% gap
Marsh site	—	3.3%	6.6%	10.7%
Rice site	2.9%	7.0%	10.8%	13.5%
Soybean site	2.1%	5.6%	8.6%	13.5%

including spike removal, frequency response correction [17], sonic virtual temperature correction [18], the performance of the planar fit coordinate rotation [19], and corrections for density fluctuation (WPL correction) [20].

The quality control of the half-hourly flux data was carried out as follows: (i) data from periods of sensor malfunction were rejected (e.g., when there was a faulty diagnostic signal), (ii) data within 1 h before or after precipitation were rejected, (iii) incomplete 30 min data were rejected when the missing data constituted more than 3% of the 30 min raw record, and (iv) data were rejected when the value was larger than mean \pm 3 standard deviation. The information of original gaps in NEE measurements is showed in Table 1. The gap percentages in all time were 25.4%, 18.2%, and 20.5% at the marsh, rice, and soybean site, respectively. Gap percentages at nighttime (ranging from 26.7% to 36.2%) were slightly higher than at daytime (ranging from 12.4% to 18.4%) (Table 1).

For this comparison, four artificial datasets were created, containing 35%, 45%, 55%, and 65% of gaps [3]. Based on random function RAND, sets of data with random distribution were generated. The random dataset corresponded to the dataset of NEE measurements except for original gaps. According to the difference from the number of artificial gaps to original gap, a range of certain numbers were selected from a set of random data, then a new gap was generated by deleting corresponding the NEE dataset. Starting from the original gap percentage, artificial gaps were created separately for daytime and nighttime, until the dataset contained a given percentage of gaps at both daytime and nighttime [3]. To avoid underestimation of CO₂ flux during calm conditions at night, the friction velocity (u^*) was applied at nighttime [21, 22]. The data were rejected at night when the u^* was below 0.10 ms⁻¹. Due to the percentage of u^* filtered data was about 10% at three sites, which caused high percentage of original gaps at nighttime. Therefore, the u^* correction was applied to artificial data instead of original data. The percentage of u^* filtered data ranged from 2.1% to 13.5% in different percentages of artificial datasets (Table 2).

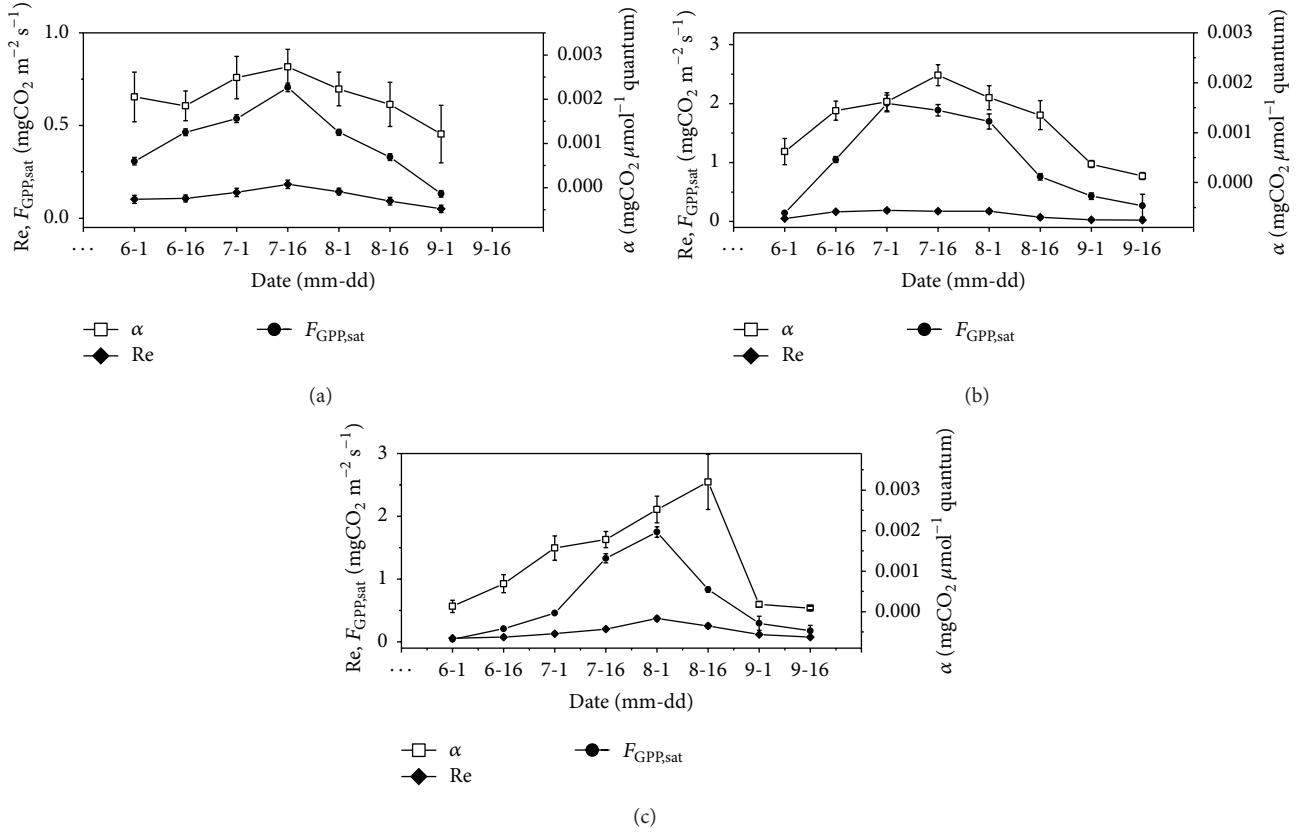


FIGURE 1: Seasonal variation of the parameters in *Michaelis–Menten* functions at (a) marsh, (b) rice, and (c) soybean sites.

After introducing artificial gaps for each of the four datasets, the respective gap-filling methods were parameterized with the remaining data and applied to fill the artificial datasets. The gap-filling error was calculated using the observed fluxes in these artificial gaps to validate the predictions of each filling technique.

2.2. Filling Methods. Three gap-filling methods were applied here, including mean diurnal variation (MDV), look-up tables (LUT), and nonlinear regression (NLR) methods.

2.2.1. Mean Diurnal Variation. MDV is an interpolation technique where the missing NEE value for a certain time period (half-hour) is replaced with the averaged value of the adjacent days at exactly that time of day. Data windows of 7 days during daytime and 14 days during nighttime were chosen for averaging in the application.

2.2.2. Look-Up Tables. In a look-up table, the NEE data are binned by variables such as light and temperature presenting similar meteorological conditions, so that a missing NEE value with similar meteorological conditions can be “looked up” [3]. Tables were created to represent changing environmental conditions based on monthly period, using the photosynthetic photon flux density- (PPFD-) air temperature- (Ta-) sort during day, and the relative humidity- (RH-) Ta-sort during night. For look-up tables the average NEE was compiled for six monthly periods * 11 PPFD-class * 36

Ta-classes. The PPFD-classes consisted of 200 μ mol m⁻² s⁻¹ intervals from 0 to 2000 μ mol m⁻² s⁻¹. Similarly, Ta-classes were defined through 1°C intervals ranging from -5°C to 31°C. For night day, average NEE was compiled for six monthly periods * 8 RH-classes * 19 Ta-classes. RH-classes range from 20% to 100% with 10% intervals, and Ta-classes were the same as the daytime.

2.2.3. Nonlinear Regression Methods. The nonlinear regressions are based on parameterized nonlinear equations which express (semi-)empirical relationships between the CO₂ flux and environmental variables such as temperature and light.

For filling daytime gaps, the light response function of *Michaelis–Menten* [3, 23] was selected as follows:

$$NEE = Re - \frac{\alpha \cdot PPFD \cdot F_{GPP,sat}}{F_{GPP,sat} + \alpha \cdot PPFD}, \quad (1)$$

where NEE is the net ecosystem exchange (mgCO₂ m⁻² s⁻¹) and Re is the ecosystem respiration rate (mgCO₂ m⁻² s⁻¹) during the day. PPFD is the photosynthetic photon flux density (μ mol m⁻² s⁻¹), and α is the ecosystem quantum yield (mgCO₂ μ mol⁻¹ quantum). $F_{GPP,sat}$ is the gross primary productivity at “saturating” light (mgCO₂ m⁻² s⁻¹). The light response function was fitted with window sizes of 15 days from June to middle September, and the seasonal variation of parameters was showed in Figure 1. The parameters in Figure 1 were calculated according to original NEE datasets

before artificial gap introduction. The $F_{\text{GPP,sat}}$ at the rice and soybean sites ranged from 0.17 to 2.0 $\text{mgCO}_2 \text{ m}^{-2} \text{ s}^{-1}$, which were larger than that at the marsh site (from 0.04 to 0.7 $\text{mgCO}_2 \text{ m}^{-2} \text{ s}^{-1}$). The R_e ranged from 0.05 to 0.37 $\text{mgCO}_2 \text{ m}^{-2} \text{ s}^{-1}$ at all three sites, which were lower than the $F_{\text{GPP,sat}}$. The correlation coefficients (R^2) of observed and simulation value during this period were 0.69, 0.83, and 0.81 ($P < 0.01$) at the marsh, rice, and soybean sites, respectively. For each artificial dataset, the parameters in *Michaelis–Menten* function were recalculated and applied to artificial gaps.

The net ecosystem CO_2 exchange (NEE) at nighttime represents the ecosystem respiration (R_{eco}) because of no photosynthesis. The ecosystem respiration (R_{eco}) is conceptualized to consist of soil respiration, R_s , and above-ground component attributed to the respiration by various plant components, R_p . For nighttime NEE, the temperature response function was selected based on Wohlfahrt et al. [24]:

$$\begin{aligned} R_{\text{eco}} &= R_s + R_p \\ &= R_{s,T_{\text{ref}}} \cdot \exp \left[\frac{E_s}{R \cdot T_{\text{ref}}} \left(1 - \frac{T_{\text{ref}}}{T_a} \right) \right] + L \cdot R_{p,T_{\text{ref}}} \\ &\quad \cdot \exp \left[\frac{E_p}{R \cdot T_{\text{ref}}} \left(1 - \frac{T_{\text{ref}}}{T_a} \right) \right], \end{aligned} \quad (2)$$

where R_{eco} is ecosystem respiration at nighttime ($\text{mgCO}_2 \text{ m}^{-2} \text{ s}^{-1}$), which includes soil respiration (R_s) and plant respiration (R_p). $R_{x,T_{\text{ref}}}$ is the respiration rate ($\text{mgCO}_2 \text{ m}^{-2} \text{ s}^{-1}$) at a reference temperature (T_{ref}), the reference temperature is 10°C, and E_x denotes an activation energy (J mol^{-1}), the subscript of x as s represent to the soil components, and the subscript of x as p represent to the plant components. R is the universal gas constant, 8.314 $\text{J mol}^{-1} \text{ K}^{-1}$. T_a is air temperature (°C), and L denotes leaf area index. The respiration function was fitted for the whole growing season, whose parameters were showed in Table 3. The parameters in Table 3 were calculated according to original NEE datasets before artificial gap introduction. For each artificial dataset, the parameters in temperature response function were recalculated and applied to artificial gaps.

2.3. Error Assessment. To assess the applicability of a standard data filling method at three sites, we examined the potential bias error associated with each method. The bias errors for different methods were calculated as the observed value minus the predicted value for each gap level. For daytime carbon uptake, a positive error therefore indicates an over-estimation and a negative error in underestimation by the respective method.

The statistical sums were calculated using the individual observed NEE data o_i and the predicted value p_i , mean bias

error (MBE), mean absolute error (MAE), and sum relative error (SRE) were as follows:

$$\begin{aligned} \text{MBE} &= \frac{1}{N} \sum (o_i - p_i), \\ \text{MAE} &= \frac{1}{N} \sum |o_i - p_i|, \\ \text{SRE} &= \frac{\sum o_i - \sum p_i}{\sum o_i}. \end{aligned} \quad (3)$$

3. Results

3.1. Frequency of Gaps. The gap distribution for benchmark sets showed the number of gaps decreased with gap length (Figure 2). However, the majority of 35% artificial gaps consisted of short gaps (less than 10 half-hours), and very short gaps (less than 2 half-hours) were more than other 3 benchmark sets. Though gap numbers of long gaps (more than 20 half-hours) for 65% gaps of artificial data sets were similar to benchmark sets, gap numbers of short and medium gaps were higher than benchmark sets.

3.2. Error Analysis in Half-Hourly Scale. The most frequent distribution of error for gap-filling methods in half-hourly scale was nearly normal distribution (Figure 3), which indicated an unbiased estimate for gap-filling error. The mean and standard deviation of bias error for gap-filling methods were showed in three sites (Table 4). The count for nighttime data was less than daytime data because of u^* -correction. They were not consistent with negative or positive error for three methods or four gap percentage levels. No trends were found that MBE was larger than gap percent levels during day and nighttime at three sites; moreover, the error for high gap level was small inversely, that is, error of 65% gaps with MDV and LUT methods at marsh site at daytime and error of 65% gaps with three methods at rice site at nighttime. For daytime data, standard deviation for LUT method was the largest and for NLR method was the lowest among three methods for each gap level. For nighttime data, standard deviation for MDV method was the largest, especially at soybean site.

3.3. Seasonal Variation of Error. The seasonal patterns of daily MBE, taking 65% gaps level as an example, showed the difference in each site (Figure 4). These patterns were affected by different methods and stage of growth. In general, all methods have good performance before germination or sawing stage and after entirely wilting or harvesting; in these stages, daily MBE for each method was around zero and MDV method with less fluctuation. The daily MBE was large in the peak of growing season because of strong assimilated CO_2 ability, and spikes often occurred for MDV and LUT methods in this stage at three sites. This result was agreed with large standard deviation for MDV and LUT in Table 4. The significant difference among the methods in fast growth stage of spring (LAI was rapid increase), that is, late May at marshland site, early June at rice site, and middle June at soybean site (Figure 4). However, MDV method has good performance in this stage.

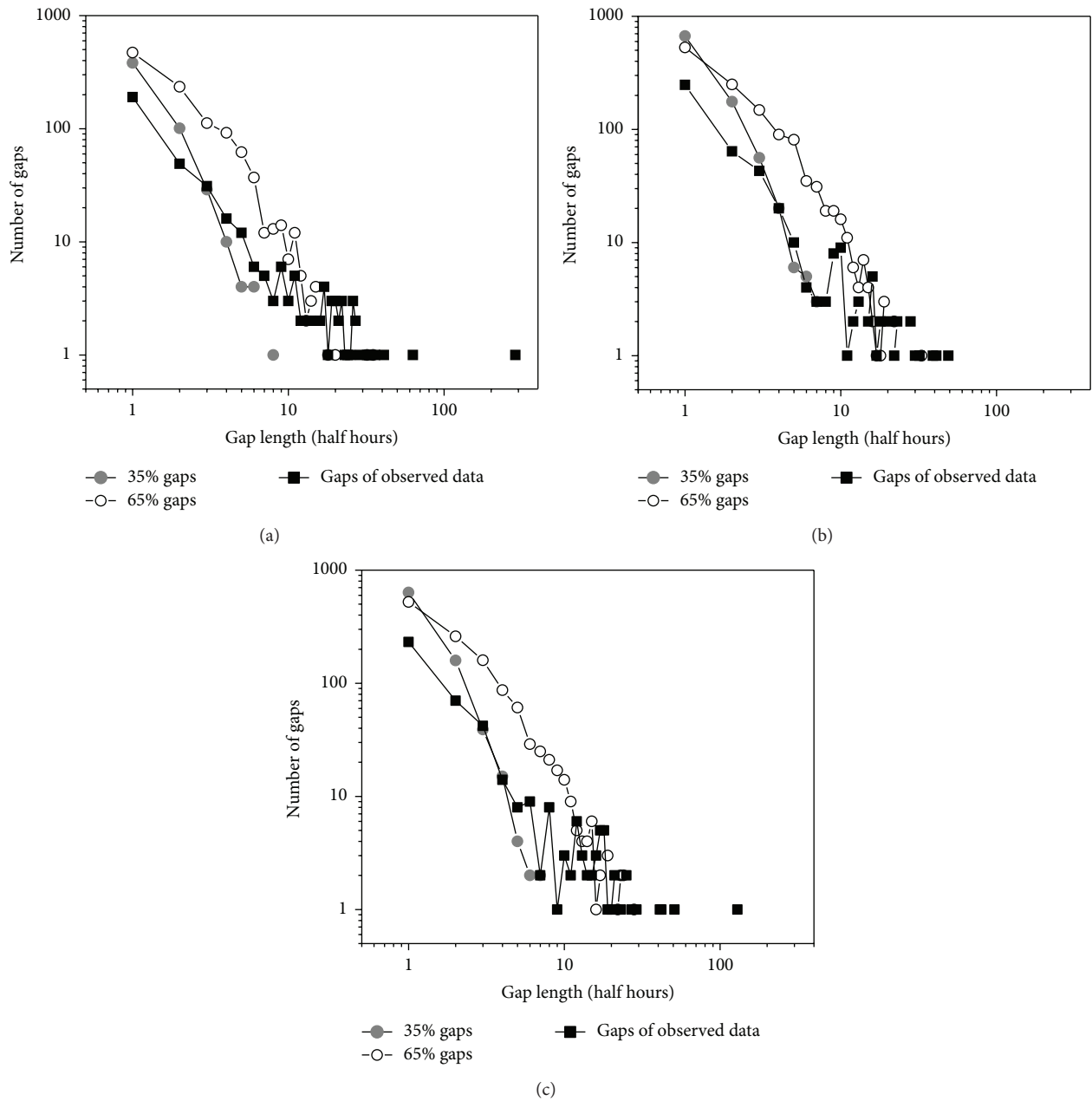


FIGURE 2: Frequency of gap lengths at (a) marsh, (b) rice, and (c) soybean sites. To show clearly, only frequencies of 35% and 65% gaps were plotted. The frequencies of 45% and 55% gaps were distributed between them.

TABLE 3: The parameters in temperature response function for nighttime data.

Sites	$R_{s,T_{ref}}^{(a)}$ $\text{mgCO}_2 \text{ m}^{-2} \text{ s}^{-1}$	E_s KJ mol^{-1}	$R_{p,T_{ref}}^{(b)}$ $\text{mgCO}_2 \text{ m}^{-2} \text{ s}^{-1}$	E_p KJ mol^{-1}	R^2	P
Marsh site	0.035	55.3	0.022	2.8	0.54	<0.01
Rice site	0.033	85.2	0.0013	79.8	0.62	<0.01
Soybean site	0.068	52.8	0.0026	148.4	0.47	<0.01

^(a) $R_{s,T_{ref}}$: soil respiration at reference temperature of 10°C.

^(b) $R_{p,T_{ref}}$: plant respiration at reference temperature of 10°C and unit leaf area.

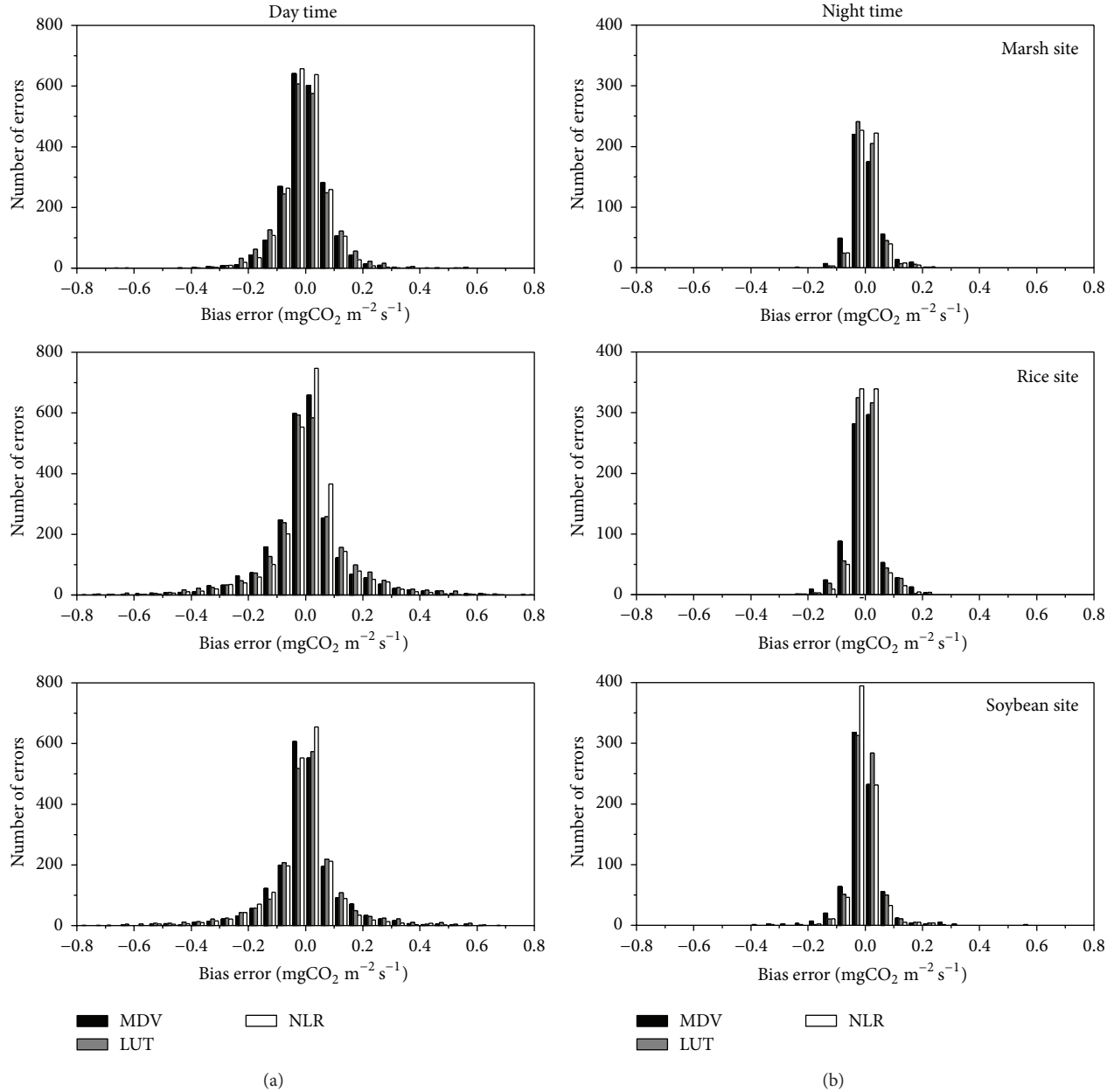


FIGURE 3: Frequency distribution of bias error with different methods for 65% artificial gaps at three sites, separated into daytime (a) and nighttime (b) data.

The variation of cumulative error was shown in Figure 5, taking 65% gaps level as an example. The cumulative error at daytime has stronger fluctuation than at nighttime at three sites, as the results of a little data and small error at nighttime. The cumulative error for three methods has no consistent bias at marsh site (Figure 5). However, positive bias errors were observed for three methods during the day at rice site, and negative bias errors were observed at soybean site. This suggests different methods may cause complicated effects at three sites. The huge bias error for LUT method was observed at each site, especially, in spring of rapid growth stage. The large bias error for NLR method was also observed after August at soybean site, whereas this phenomenon has not

occurred in 35% and 45% gaps. Based on cumulative error from May to October, it indicates that MDV method has good performance, especially smooth trend in the end of growing season at three sites. Overall, the cumulative error at three sites ranged between -30 and $+30$ $\text{mgCO}_2 \text{m}^{-2}$.

The SRE was showed in Table 5, and it is convenient to evaluate the performance of gap-filling methods and compare it with other sites. In general, the SRE for 35% and 45% artificial gaps filled by three methods was smaller than 55% and 65% gaps at daytime, while these patterns were not marked at nighttime. The gap-filling methods have distinct different performances at three sites; for example, MDV method showed small SRE at daytime over the rice site, while

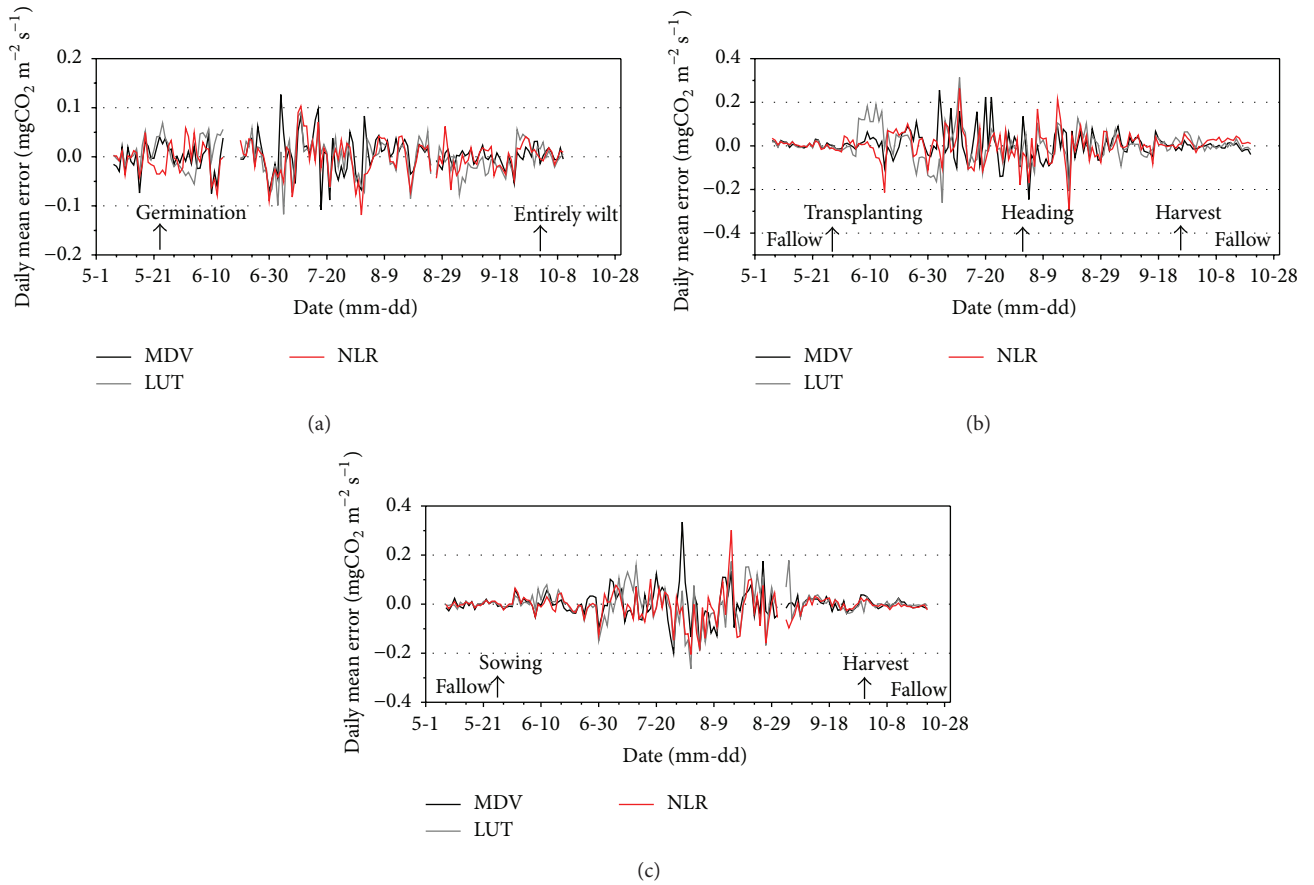


FIGURE 4: Seasonal variations of daily mean bias error (MBE) with different methods at (a) marsh, (b) rice, and (c) soybean sites.

TABLE 4: Mean bias error of half-hourly F_{NEE} and standard deviation from the mean^(a).

Flux site	Gap %	$n^{(b)}$	Day time			$n^{(b)}$	Night time (u^* corrected)		
			MDV	LUT	NLR		MDV	LUT	NLR
			mgCO ₂ m ⁻² s ⁻¹						
Marsh site	35	763	-2.51 (79.04)	-0.75 (88.05)	-4.36 (73.46)	na ^(c)	na	na	na
	45	1220	3.42 (73.26)	-0.14 (78.84)	0.66 (69.65)	161	2.21 (47.18)	1.19 (34.85)	0.73 (35.65)
	55	1677	4.27 (78.65)	3.09 (90.18)	2.00 (78.88)	359	-1.26 (47.56)	2.19 (35.97)	2.16 (36.46)
	65	2136	1.66 (84.39)	-0.78 (90.66)	-3.32 (74.42)	532	4.14 (51.87)	4.95 (41.49)	5.49 (41.24)
Rice site	35	1084	-0.10 (144.58)	-4.59 (154.58)	-7.17 (123.62)	175	3.89 (53.96)	2.52 (47.19)	2.16 (46.24)
	45	1565	-0.17 (152.18)	1.79 (165.22)	3.5 (124.08)	366	3.56 (54.27)	-2.04 (48.94)	1.60 (42.13)
	55	2045	-1.14 (145.34)	-2.69 (168.33)	-5.33 (126.43)	564	-5.22 (58.38)	-1.27 (48.69)	0.55 (40.58)
	65	2525	2.76 (149.03)	9.68 (160.66)	11.25 (123.96)	797	-0.59 (57.99)	1.11 (48.94)	0.06 (41.25)
Soybean site	35	964	-2.17 (115.52)	1.64 (134.87)	-6.9 (114.04)	136	-21.8 (93.51)	-9.42 (44.1)	-8.8 (33.09)
	45	1445	-1.88 (114.98)	1.81 (136.21)	-2.27 (113.32)	345	1.91 (74.24)	4.96 (46.71)	3.57 (44.11)
	55	1929	-5.21 (112.73)	-3.2 (132.46)	-9.41 (110.09)	569	1.72 (69.91)	0.19 (45.55)	1.19 (41.73)
	65	2411	-1.7 (112.09)	-2.05 (134.55)	-10.97 (109.28)	732	-3.26 (74.96)	0.30 (47.45)	-2.59 (41.61)

^(a) Values in parentheses are standard deviation.^(b) Number of the artificial gaps.^(c) No measurements were available due to large gaps.

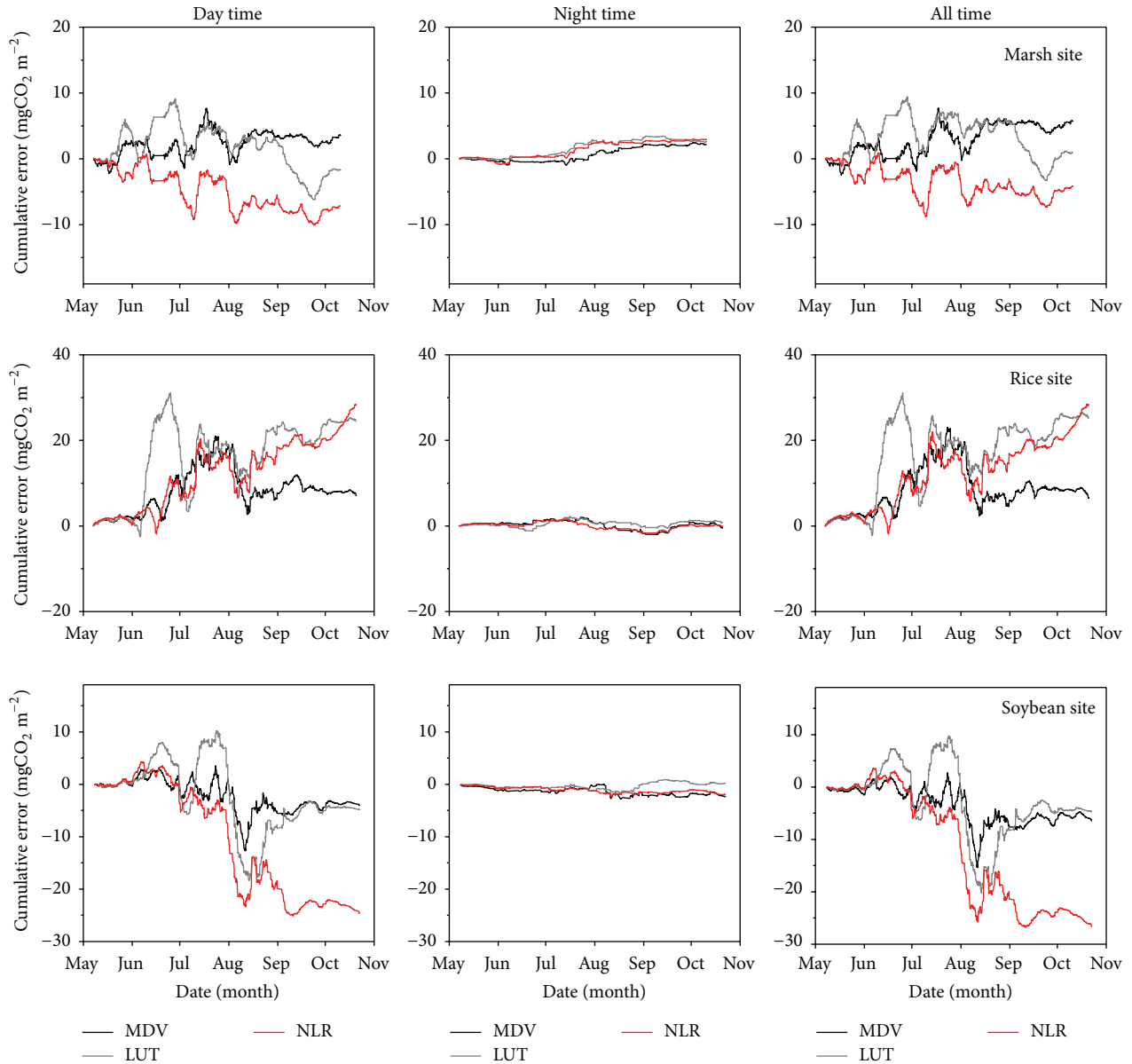


FIGURE 5: Cumulative error in gap-filled NEE from May to October, separated in daytime, nighttime, and all time contribution, at marsh, rice, and soybean sites.

LUT and NLR methods represented well at daytime over the marsh site. The majority of SRE ranged from -10 to 10 during whole day, except for 55% and 65% artificial gaps filled by NLR method at soybean site, this caused by huge bias after August (showed in Figure 5).

3.4. Error Analysis in Gap Size Class. Gap size and distribution were produced in random, whereas those greatly impacted performance of gap filling methods. The colored surface plots are depicted in Figure 6, 65% gaps were taken as an example, which provide a visual means of qualitatively assessing the impact of gap length on NEE uncertainty. For short vegetation, small MAE was expressed in dormant season (early spring and late autumn), regardless of methods and gap length. This was related to the fact that measured

fluxes at this stage tended to be smaller. Large errors for three methods were concentrated to the zone of gaps of less than 5 in growing season, especially in stage of growth rapidly of plants. Among the methods, LUT method resulted in the largest error ranging from short to long gaps and then MDV and NLR methods. Though the patterns did not find that MAE for all methods increased with gap length increasing, long gaps added appreciably to the uncertainty of gap-filling (results were not shown).

3.5. Optimum Gap Filling Method for Short Vegetation. Selection of methods was based on the most stable performance and smallest errors; however, according to the above analysis, no one method was perfect during the measuring stage. To reduce sum bias in maximum, combined gap-filling method

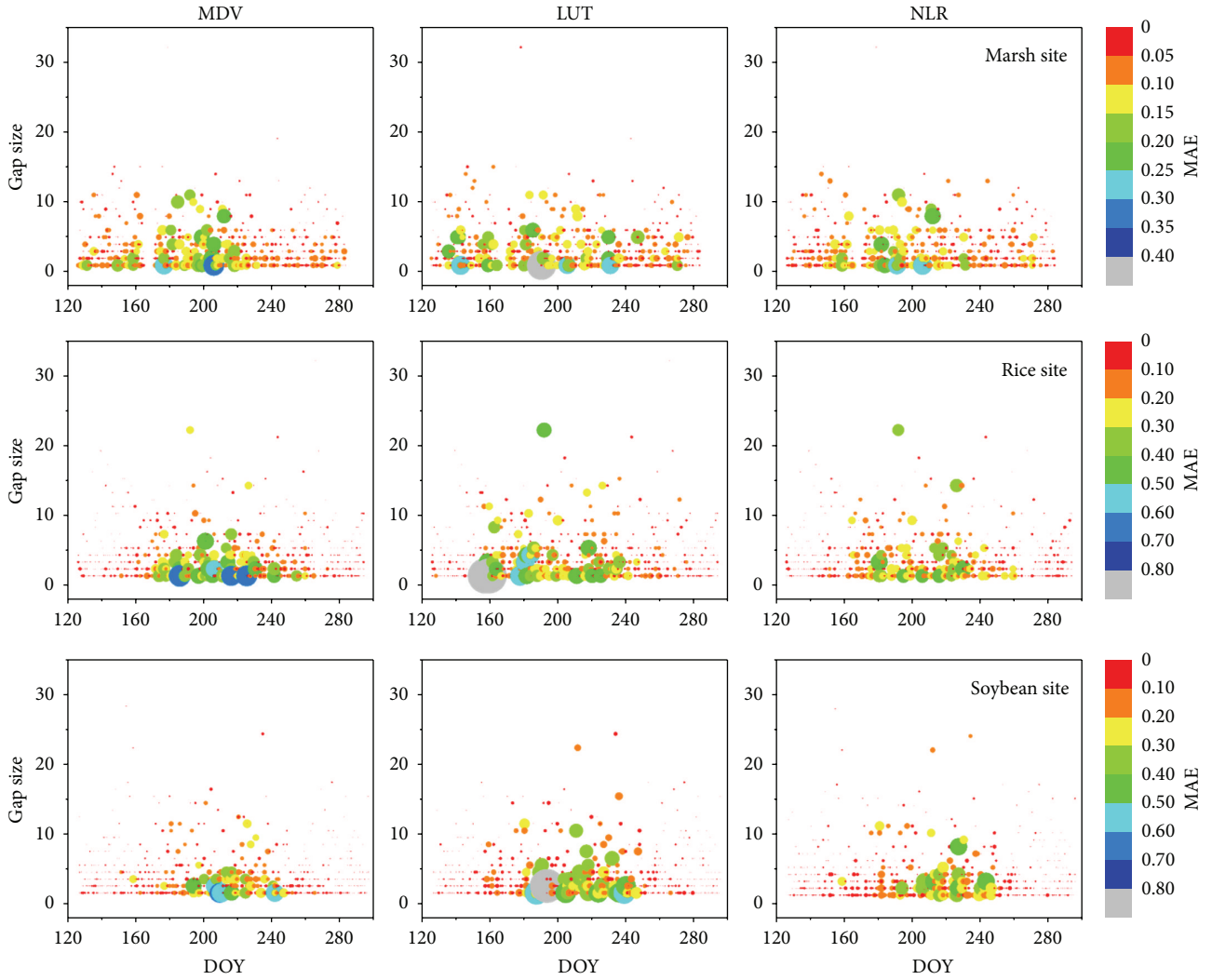


FIGURE 6: Two-dimensional plots illustrating mean absolute error (MAE) in gap-filled NEE, expressed as MAE, varied as a function of day of year (*x axis*) and gap length (*y axis*). Plots in row were shown for marsh, rice, and soybean sites, and plots in column were shown for MDV, LUT, and NLR methods. The different size and color of the circle refer to magnitude of MAE, and unit is $\text{mgCO}_2 \text{ m}^{-2} \text{ s}^{-1}$.

TABLE 5: The sum relative error (SRE) for NEE in different gap levels, at marsh, rice, and soybean site.

	Gap %	Daytime			Nighttime (u^* corrected)			All time		
		MDV %	LUT %	NLR %	MDV %	LUT %	NLR %	MDV %	LUT %	NLR %
Marsh site	35	2.83	0.85	4.92	na ^(a)	na	na	2.83	0.85	4.92
	45	-3.61	0.15	-0.70	2.51	1.36	0.83	-4.46	-0.02	-0.92
	55	-4.98	-3.60	-2.33	-1.46	2.54	2.49	-5.93	-5.23	-3.67
	65	-1.74	0.82	3.48	4.60	5.50	6.11	-3.67	-0.61	2.66
Rice site	35	0.05	3.37	2.28	4.38	2.84	2.43	-0.28	3.41	2.27
	45	0.08	-0.81	-1.59	3.97	-2.27	1.79	-0.33	-0.66	-1.94
	55	0.58	1.38	2.73	-5.67	-1.38	0.60	1.52	1.79	3.05
	65	-1.40	-4.89	-5.68	-0.69	1.29	0.08	-1.51	-5.86	-6.59
Soybean site	35	2.21	-1.67	7.01	-22.99	-9.94	-9.28	5.16	-0.37	9.58
	45	1.82	-1.75	2.20	1.57	4.09	2.94	1.92	-4.04	1.91
	55	5.80	3.56	10.48	1.47	0.16	1.02	8.49	5.67	16.36
	65	1.74	1.97	10.11	-2.88	0.27	-2.29	4.93	3.6	20.28

^(a)No measurements were available due to large gaps.

TABLE 6: Gap filling strategies at short vegetation ecosystems.

Ecosystem	Method of gap filling		
	NLR	LUT	MDV
Marshland	Early Jun to mid Sept		Other time from May to Oct
Rice paddy	Mid Jun to mid Aug		Other time from May to Oct
Soybean		Early Jul to early Sept	Other time from May to Oct

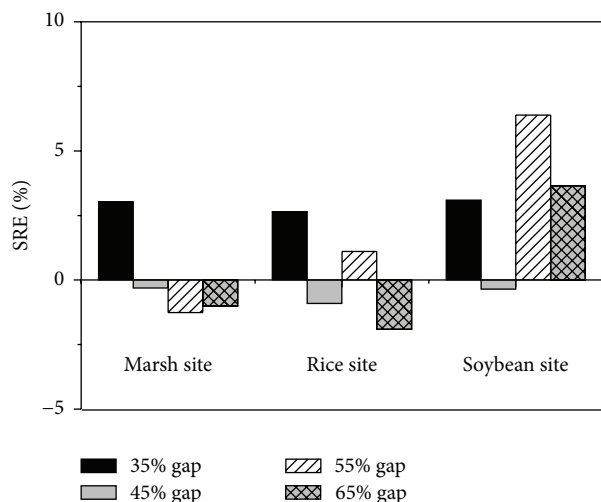


FIGURE 7: The sum relative error (SRE) of optimum gap-filling method for four-gap level at three sites.

was selected for short vegetation. NLR or LUT method was used after plant rapidly growing in spring and after end of plant growth, and MDV method was used to the other stage. In this case, based on the growth stage of different vegetation, the gap filling strategies at three ecosystems were showed in Table 6. The SRE of optimum method reduced to the range of -2 and $+4\%$ for four-gap level at three sites (Figure 7), except for 55% gaps at soybean site. The optimum method also reduced standard deviation of error that was around 0.07, 0.11, and 0.12 $\text{mgCO}_2 \text{ m}^{-2} \text{ s}^{-1}$ at marsh, rice, and soybean site, respectively; there were no significant different within four-gap level.

4. Discussion

4.1. The Response of Error on Environmental and Biological Factors. The performance of gap-filling methods impacted on climatic and biological variables such as PPFD and LAI [6, 23]. The LUT and NLR methods have considered the effect of PPFD, a residual error with NLR method distributed evenly around zero response of PPFD with small magnitude (Figure 8), while residual error with LUT method scattered strongly around zero. This was the reason of high standard deviation at daytime (Table 4). The residual error with MDV method caused positive bias when PPFD was less than $500 \mu\text{mol m}^{-2} \text{ s}^{-1}$.

The residual errors response of LAI with NLR method has even distribution around zero, and MDV and LUT method have more scatter; moreover, significant negative

error occurred around LAI = 1 (Figure 8). The large scatters were showed for MDV method that did not consider LAI when filling gaps. Though the LUT method filled gaps per half month, there was weak relationship between LAI and NEE, especially when LAI = 1 (Figure 8). This result must be expected from potential changes in the ecosystem properties, particularly as related to canopy development and senescence [6, 25].

4.2. The Selection of Gap-Filling Methods for Short Vegetations.

In this study for short vegetations, error introduced by gap-filling differed between methods at different gap levels (Table 4). The choice of a technique should be based on the application, Moffat et al. [9] considered NLR method can serve well for an annual sum estimate, but an artificial neural network will best reproduce the half-hourly profile of the flux. Falge et al. [3] also commented on semiempirical methods because they preserve the response of NEE to main meteorological conditions. However, the NLR method in our study has good performance in variation of daily NEE (Figure 4) and caused huge bias in cumulative NEE, especially for high gap level (Figure 5), which can explain that great uncertainty was introduced, because little data was available to simulating nonlinear function.

The MDV method had large error in half-hourly NEE (Figure 4) but consistent performance and reliability in sum NEE (Figure 5). For MDV, the method does not make use of the ancillary meteorological data and can be expected to have additional problems filling gaps of more than 3–7 days in length, as synoptic changes in weather are strongly linked to changes in diurnal cycles of photosynthesis and respiration [1, 9]. So, to reduce error in half-hourly and annual NEE, the combined method of MDV and NLR was selected in our study (Figure 7) and performed well for short vegetation.

The methods caused large bias during periods of active change in ecosystem properties (Figure 4), because when the flux data are missing, it is impossible to know the timing of magnitude of the change [3, 15]. The magnitudes of NEE for short vegetation, that is, marsh or cropland, and so forth, were smaller than forests; especially for soybean cropland, high GPP and high Re caused low NEE during the growing season. So little error may cause large bias of cumulative NEE, and underestimating NEE or overestimating Re may change carbon sink to carbon source. In this study, the optimum gap-filling method can resolve partly this problem.

5. Conclusion

The three major gap-filling methods (mean diurnal variation, look-up table and nonlinear regression) for estimating net

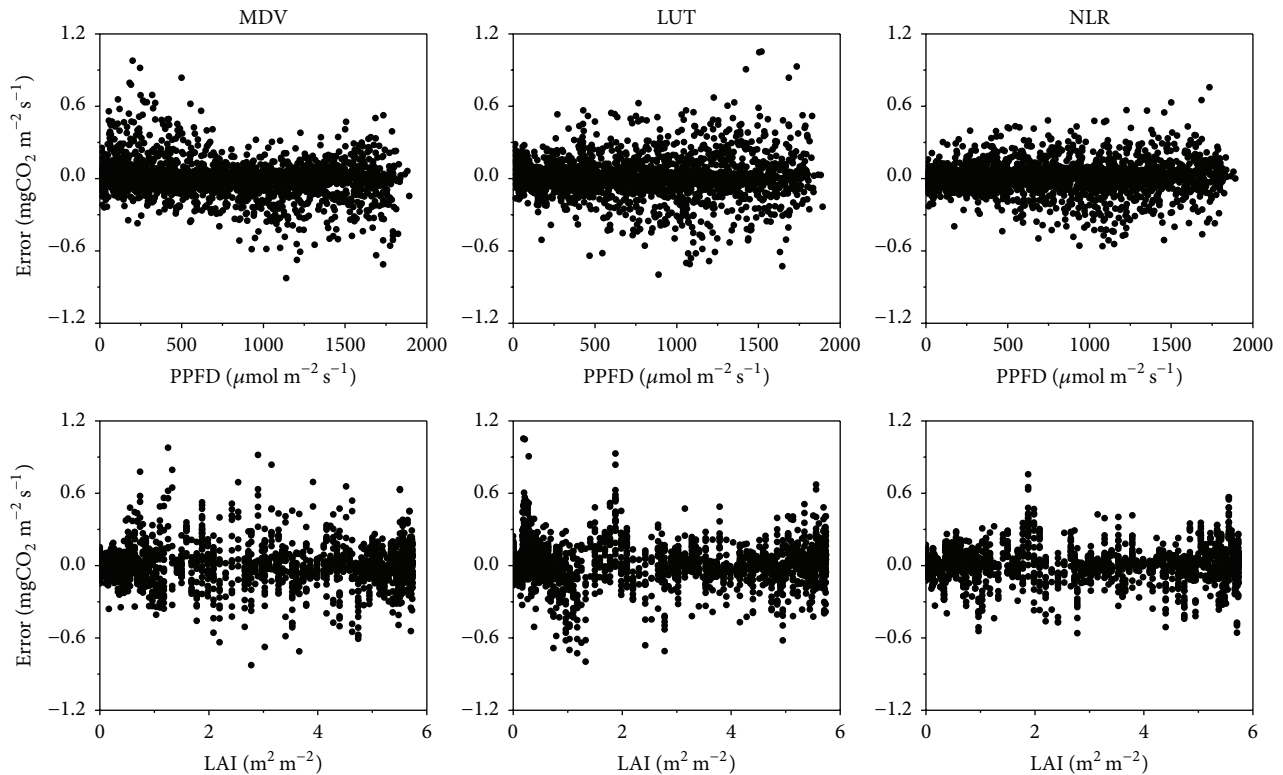


FIGURE 8: The relationship between bias error and PPFD and LAI in day time, taking 65% gaps at rice site as an example.

carbon fluxes (NEE) were reviewed and their gap-filling performance was evaluated based on a set of datasets from three short vegetations (marsh, rice, and soybean sites). The performance of the filling techniques depended on the time scale, gap length, and time of day (day or night). In half-hourly scale, standard deviation for NLR method was the smallest among three methods for each gap level. The MDV method has good performance in seasonal scale, especially before germination or sowing and after entirely wilting or harvesting. Though LUT and NLR methods showed small error for daily mean error during the peak of growing season, the huge bias was observed in cumulative NEE for two methods. The combined gap-filling methods were used for short vegetation, which showed NLR or LUT method was selected after plant rapidly increasing in spring and before end of plant growth and MDV method was used to the other stage. This combined method distinctly reduced sum bias and deviation for gap-filled NEE.

Conflict of Interests

The authors declare that there is no conflict of interests regarding the publication of this paper.

Acknowledgment

This work was supported by the National Natural Science Foundation of China (no. 41471022).

References

- [1] D. Baldocchi, E. Falge, L. Gu et al., "FLUXNET: A New Tool to Study the Temporal and Spatial Variability of Ecosystem-Scale Carbon Dioxide, Water Vapor, and Energy Flux Densities," *Bulletin of the American Meteorological Society*, vol. 82, no. 11, pp. 2415–2434, 2001.
- [2] D. Papale, M. Reichstein, M. Aubinet et al., "Towards a standardized processing of Net Ecosystem Exchange measured with eddy covariance technique: algorithms and uncertainty estimation," *Biogeosciences*, vol. 3, no. 4, pp. 571–583, 2006.
- [3] E. Falge, D. Baldocchi, R. Olson et al., "Gap filling strategies for defensible annual sums of net ecosystem exchange," *Agricultural and Forest Meteorology*, vol. 107, no. 1, pp. 43–69, 2001.
- [4] A. R. Desai, P. V. Bolstad, B. D. Cook, K. J. Davis, and E. V. Carey, "Comparing net ecosystem exchange of carbon dioxide between an old-growth and mature forest in the upper Midwest, USA," *Agricultural and Forest Meteorology*, vol. 128, no. 1-2, pp. 33–55, 2005.
- [5] A. Noormets, J. Chen, and T. R. Crow, "Age-dependent changes in ecosystem carbon fluxes in managed forests in northern Wisconsin, USA," *Ecosystems*, vol. 10, no. 2, pp. 187–203, 2007.
- [6] M. Reichstein, E. Falge, D. Baldocchi et al., "On the separation of net ecosystem exchange into assimilation and ecosystem respiration: review and improved algorithm," *Global Change Biology*, vol. 11, no. 9, pp. 1424–1439, 2005.
- [7] D. Hui, S. Wan, B. Su, G. Katul, R. Monson, and Y. Luo, "Gap-filling missing data in eddy covariance measurements using multiple imputation (MI) for annual estimations," *Agricultural and Forest Meteorology*, vol. 121, no. 1-2, pp. 93–111, 2004.

- [8] B. H. Braswell, W. J. Sacks, E. Linder, and D. S. Schimel, "Estimating diurnal to annual ecosystem parameters by synthesis of a carbon flux model with eddy covariance net ecosystem exchange observations," *Global Change Biology*, vol. 11, no. 2, pp. 335–355, 2005.
- [9] A. M. Moffat, D. Papale, M. Reichstein et al., "Comprehensive comparison of gap-filling techniques for eddy covariance net carbon fluxes," *Agricultural and Forest Meteorology*, vol. 147, no. 3–4, pp. 209–232, 2007.
- [10] D. Papale and R. Valentini, "A new assessment of European forests carbon exchanges by eddy fluxes and artificial neural network spatialization," *Global Change Biology*, vol. 9, no. 4, pp. 525–535, 2003.
- [11] A. Schmidt, T. Wrzesinsky, and O. Klemm, "Gap filling and quality assessment of CO₂ and water vapour fluxes above an urban area with radial basis function neural networks," *Boundary-Layer Meteorology*, vol. 126, no. 3, pp. 389–413, 2008.
- [12] W. Knorr and J. Kattge, "Inversion of terrestrial ecosystem model parameter values against eddy covariance measurements by Monte Carlo sampling," *Global Change Biology*, vol. 11, no. 8, pp. 1333–1351, 2005.
- [13] K. Morgenstern, T. A. Black, E. R. Humphreys et al., "Sensitivity and uncertainty of the carbon balance of a Pacific Northwest Douglas-fir forest during an El Niño/La Niña cycle," *Agricultural and Forest Meteorology*, vol. 123, no. 3–4, pp. 201–219, 2004.
- [14] Y.-Y. Chen, C.-R. Chu, and M.-H. Li, "A gap-filling model for eddy covariance latent heat flux: estimating evapotranspiration of a subtropical seasonal evergreen broad-leaved forest as an example," *Journal of Hydrology*, vol. 468, pp. 101–110, 2012.
- [15] A. D. Richardson and D. Y. Hollinger, "A method to estimate the additional uncertainty in gap-filled NEE resulting from long gaps in the CO₂ flux record," *Agricultural and Forest Meteorology*, vol. 147, no. 3–4, pp. 199–208, 2007.
- [16] X. Zhao, Y. Huang, Z. Jia et al., "Effects of the conversion of marshland to cropland on water and energy exchanges in northeastern China," *Journal of Hydrology*, vol. 355, no. 1–, pp. 181–191, 2008.
- [17] W. J. Massman and X. Lee, "Eddy covariance flux corrections and uncertainties in long-term studies of carbon and energy exchanges," *Agricultural and Forest Meteorology*, vol. 113, no. 1–4, pp. 121–144, 2002.
- [18] A. I. J. M. van Dijk and A. J. Dolman, "Estimates of CO₂ uptake and release among European forests based on eddy covariance data," *Global Change Biology*, vol. 10, no. 9, pp. 1445–1459, 2004.
- [19] J. M. Wilczak, S. P. Oncley, and S. A. Stage, "Sonic anemometer tilt correction algorithms," *Boundary-Layer Meteorology*, vol. 99, no. 1, pp. 127–150, 2001.
- [20] E. K. Webb, G. I. Pearman, and R. Leuning, "Correction of flux measurements for density effects due to heat and water vapour transfer," *Quarterly Journal Royal Meteorological Society*, vol. 106, no. 447, pp. 85–100, 1980.
- [21] P. D. Blanken, T. A. Black, H. H. Neumann et al., "Turbulent flux measurements above and below the overstory of a boreal aspen forest," *Boundary-Layer Meteorology*, vol. 89, no. 1, pp. 109–140, 1998.
- [22] L. Gu, E. M. Falge, T. Boden et al., "Objective threshold determination for nighttime eddy flux filtering," *Agricultural and Forest Meteorology*, vol. 128, no. 3–4, pp. 179–197, 2005.
- [23] D. Y. Hollinger, J. Aber, B. Dail et al., "Spatial and temporal variability in forest—atmosphere CO₂ exchange," *Global Change Biology*, vol. 10, no. 10, pp. 1689–1706, 2004.
- [24] G. Wohlfahrt, C. Anfang, M. Bahn et al., "Quantifying nighttime ecosystem respiration of a meadow using eddy covariance, chambers and modelling," *Agricultural and Forest Meteorology*, vol. 128, no. 3–4, pp. 141–162, 2005.
- [25] V. J. Stauch and A. J. Jarvis, "A semi-parametric gap-filling model for eddy covariance CO₂ flux time series data," *Global Change Biology*, vol. 12, no. 9, pp. 1707–1716, 2006.

Research Article

Flooding Regime Impacts on Radiation, Evapotranspiration, and Latent Energy Fluxes over Groundwater-Dependent Riparian Cottonwood and Saltcedar Forests

James Cleverly,^{1,2} James R. Thibault,¹ Stephen B. Teet,^{1,3} Paul Tashjian,⁴
Lawrence E. Hipps,⁵ Clifford N. Dahm,¹ and Derek Eamus^{2,6}

¹Department of Biology, University of New Mexico, Albuquerque, NM 87131, USA

²Australian SuperSite Network and Terrestrial Ecohydrology Research Group, School of Life Sciences, University of Technology Sydney, P.O. Box 123, Broadway, NSW 2007, Australia

³USDA Agricultural Research Service, Grazinglands Research Laboratory, 7207 West Cheyenne Street, El Reno, OK 73036, USA

⁴U.S. Fish and Wildlife Service, National Wildlife Refuge System, Division of Water Resources, 500 Gold SW, Albuquerque, NM 87102, USA

⁵Department of Plants, Soils and Biometeorology, Utah State University, Logan, UT 84322, USA

⁶National Centre for Groundwater Research and Training, University of Technology Sydney, P.O. Box 123, Broadway, NSW 2007, Australia

Correspondence should be addressed to James Cleverly; james.cleverly@uts.edu.au

Received 2 March 2015; Accepted 19 April 2015

Academic Editor: Marcos Heil Costa

Copyright © 2015 James Cleverly et al. This is an open access article distributed under the Creative Commons Attribution License, which permits unrestricted use, distribution, and reproduction in any medium, provided the original work is properly cited.

Radiation and energy balances are key drivers of ecosystem water and carbon cycling. This study reports on ten years of eddy covariance measurements over groundwater-dependent ecosystems (GDEs) in New Mexico, USA, to compare the role of drought and flooding on radiation, water, and energy budgets of forests differing in species composition (native cottonwood *versus* nonnative saltcedar) and flooding regime. After net radiation ($700\text{--}800\text{ W m}^{-2}$), latent heat flux was the largest energy flux, with annual values of evapotranspiration exceeding annual precipitation by 250–600%. Evaporative cooling dominated the energy fluxes of both forest types, although cottonwood generated much lower daily values of sensible heat flux ($< -5\text{ MJ m}^{-2}\text{ d}^{-1}$). Drought caused a reduction in evaporative cooling, especially in the saltcedar sites where evapotranspiration was also reduced, but without a substantial decline in depth-to-groundwater. Our findings have broad implications on water security and the management of native and nonnative vegetation within semiarid southwestern North America. Specifically, consideration of the energy budgets of GDEs as they respond to fluctuations in climatic conditions can inform the management options for reducing evapotranspiration and maintaining in-stream flow, which is legally mandated as part of interstate and international water resources agreements.

1. Introduction

Partitioning of surface energy fluxes is a robust method for estimating landscape evapotranspiration (ET). It is only with widespread use of eddy covariance (EC) techniques in the last few decades that all primary fluxes can be directly measured [1, 2]. Although some of the largest rates of ET in arid and semiarid landscapes originate from riparian groundwater-dependent ecosystems (GDEs) [3, 4], measurements of energy fluxes using EC techniques in riparian ecosystems are

rare because of their narrow fetch (i.e., the upwind distance of homogenous vegetation required for flux measurements) and stable conditions under advection [5, 6]. Rivers also have an important effect on local surface energy fluxes within narrow riparian forests by increasing surface turbulence, augmenting surface fluxes, and controlling the direction of surface energy fluxes [4].

Energy is transported via three mechanisms: radiation, conduction, and convection [7]. In terrestrial ecosystems, these processes are represented by the flux of net radiation

(Q^*), the flux of heat with the ground via conduction (Q_G), and turbulent transport, which includes the fluxes of sensible (Q_H) and latent heat (Q_E) [8]. Q^* is determined as the difference between downwelling and upwelling radiation in the short (visible and solar) and long (infrared and thermal) wavelengths. Q_G can be highly variable at a given location, especially across habitats (e.g., from under shrub to bare soil) in semiarid regions [9] or in response to flooding [10]. However, Q_G tends to be small under the shade of a deep canopy [11] and when averaged over a day [12].

Observations of energy fluxes contribute to our understanding of world climate and also to our understanding of the behaviour of different forest types. Wilson et al. [2], for example, compare partitioning between Q_H and Q_E over a number of different vegetated surfaces in the Ameriflux data set. By comparing Bowen ratios (β : the ratio of sensible to latent energy fluxes; $\beta = Q_H/Q_E$), distinctions were demonstrated between vegetation type and climate, with the smallest β in agricultural and deciduous forest ecosystems and largest in coniferous and grassland ecosystems with a distinct dry climate [2]. Arid sites typically have larger β than mesic sites, except when under irrigation [13], and β can exceed four (i.e., Q_H is four times larger than Q_E) over an arid, bare soil clay pan [14]. Energy partitioning is also valuable for observing changes in response to invasion by nonnative species [15].

Water resources in the Rio Grande are governed by an interstate compact between Colorado, New Mexico, and Texas and by a treaty between the USA and Mexico [11, 16, 17]. Demand for water is larger than the allocations dictated in the compact and treaty, but adjudication of water rights is ongoing and mostly incomplete. As an initial step, a water budget was compiled to assist with enforcing legal obligations and to design and implement sustainable water policy [18]. Open water evaporation and ET from groundwater-dependent vegetation (i.e., plants that have their roots in contact with groundwater; phreatophytes) and agriculture dominate the water budget of the Middle Rio Grande [19]. Given the importance of in-stream flow and ET in the water budget, a better understanding of the energetic constraints on these ecosystems will provide improved water security during times of both scarcity and abundance. The two key aims of the work described herein are to (1) provide an analysis of the energy budget of two forest types along the Rio Grande (dominated by either a native or introduced species) and (2) examine the impacts of drought and floods on the energy budgets of these sites. Such studies will improve our ability to manage water resources sustainably across this extensive catchment and to determine strategies to achieve desired outcomes from managed changes in land use.

Increased vegetation density and cover along the Rio Grande over the past century or more has generated riparian forests with extensive fetch [11, 20, 21]. Forests extend for several kilometers parallel to the river's general north-south axis and for hundreds of meters perpendicular to the river. This paper takes a meteorological perspective to present analyses of water and energy fluxes over riparian GDEs situated along the Middle Rio Grande of central New Mexico, USA [3, 11]. Surface energy fluxes on cloud-free days were compared above native (cottonwood) and nonnative (saltcedar)

vegetation. Changes in energy balance in response to flooding and drought were evaluated. We hypothesized that (1) annual rates of ET differ across the two forest types; (2) advection and evaporative cooling, identified by Q_H directed toward the surface (i.e., $Q_H < 0$), would be common during wet periods; (3) Q_H would increase at the expense of Q_E during drought; and (4) Q_G would be insignificant under vegetated canopies [11] except during inundation, which would largely affect Q_G . For convenience, a list of symbols and abbreviations is provided in the Symbols and Abbreviations section.

2. Methods

2.1. Site Network. This study focused upon four sites in the riparian corridor along the Middle Rio Grande, New Mexico (Table 1). The shallow slope of the central valley promotes expansion of the riparian corridor, which reaches to over a kilometre in width [3]. Two of these sites host forests dominated by a mature cottonwood canopy (native, *Populus deltoides* ssp. *wislizeni*); the other two sites contain stands dominated by saltcedar (nonnative, *Tamarix chinensis*). One each of the cottonwood and saltcedar forests received regular flooding with a two- to three-year recurrence interval, whilst the complementary pair of sites have not flooded in the last 20 years or more (Table 1). Reference to each site will be made by its dominant species (i.e., cottonwood, saltcedar) and inter-flood interval (IFI), for example, cottonwood long-IFI or cottonwood short-IFI (Table 1).

Eddy covariance systems were mounted from towers in the saltcedar sites beginning in 1999 and in the cottonwood sites during 2000 [3, 19]. The tower at the cottonwood short-IFI site was destroyed by vandalism during spring 2004, at which time the site was abandoned and the data record concluded in 2003 (Table 1). At the cottonwood long-IFI site, the understory vegetation was mechanically removed in 2003 [22]. Then, in 2007, a fire burned a substantial portion of the cottonwood canopy at the long-IFI site, after which a crown fell on the tower in 2008, thereby toppling it. The cottonwood long-IFI site was subsequently abandoned that year.

Towers in the cottonwood forests were 25 m tall. Towers in the saltcedar forest were either 15 m (short-interval flooding) or 10 m (long-interval flooding) tall. Footprints of upwind measurements are about 50 m over saltcedar stands and up to 200 m over cottonwood stands [11].

2.2. Instruments and Measurements. Radiative, conductive, and turbulent energy fluxes were measured at each of these four riparian sites. Initially, three-dimensional sonic eddy covariance (3SEC) systems consisting of a CSAT3 sonic anemometer to measure wind speed in each of three dimensions (u , v , and w), a KH20 Krypton Hygrometer to measure humidity, and a CR23X (Campbell Scientific, Inc., Logan, UT) datalogger to run the system and collect 30 min flux and meteorological data were installed at all sites [11, 19]. As funds became available, most systems were upgraded (1) to replace the KH20 with a fast response, open-path infrared gas analyzer (IRGA, LI-7500, LiCor, Inc., Lincoln, NE) measuring carbon and water vapour density and (2) to

TABLE 1: Flux sites operating in the Middle Rio Grande valley node of NM-EPSCoR Fluxnet.

Code	Location	Years	IFI ^a	h_c (m)	$z - d$ (m)	ρ_d (g cm ⁻³)
CW	34.96°N, 106.68°W, 1497 m asl (Albuquerque, NM)	2000–2007	Long	23.5	9.9	1.033
CW	34.59°N, 106.75°W, 1459 m asl (Belen, NM)	2000–2003	Short	25.1	10.5	0.957
SC	34.27°N, 106.87°W, 1427 m asl (Sevilleta NWR)	1999–2010	Long	5.2	3.4	1.280
SC	33.78°N, 106.88°W, 1375 m asl (Bosque del Apache NWR)	1999–2010	Short	6.2	4.1	1.140

^aShort: 2–3 years; long: >20 years.

replace the CR23X with a CR5000 that is capable of storing 10 Hz measurements along with the 30 min flux data. A 3SEC system was mounted on the south face of each tower, 2–2.5 m above the canopy [3, 11, 19]. KH20s were mounted side-normal to prevent accumulation of water ponding on the mirror following precipitation. IRGAs were rotated 15° to the north of vertical to avoid solar reflection spikes [23].

In addition to the 3SEC systems, a suite of instruments for measuring energy balance and micrometeorology were mounted upon or near each tower. Temperature (T) and relative humidity were measured at the modal canopy height (HMP45C; Campbell Scientific, Inc., Logan, UT). Precipitation, ground heat flux in two locations beneath the canopy, spatially averaged soil temperature, and soil water content were also measured on a 30-minute basis (TE525, HFT3, TCAV, and CS616, resp.; Campbell Scientific, Inc., Logan, UT). Each system included two atmospheric pressure (P) sensors. TE525s were mounted near the top of the towers. Soil instruments were placed at standard depths: HFT3s 8 cm below surface, TCAVs 2 cm and 6 cm, and CS616 inserted horizontally at a depth of 2.5 cm.

The soil dielectric constant as measured by the CS616 is a function of soil water content (Θ), salinity, temperature, texture, and compaction [24, 25]. Thus, accurate measurement of Θ requires sensor calibration to local soil conditions. Measurements on a volumetric basis (Θ_v) were corrected using an empirical calibration curve against soil water content of samples collected *in situ*. The upper value of Θ_v measured under flooding conditions was assumed to equal porosity by discounting unmeasured changes due to deflocculation of clay during wetting. Measurements of Θ_v were converted to Θ_g (mass-basis) to match units for determination of soil heat storage. During periods when Θ_g was unavailable, Θ_g was assumed to be equal to long-term average values during periods of comparable wetness at the same site, defined as periods with similar drought index values.

Average Q_G at the surface from the two sensors was computed to account for soil heat storage above the sensors utilizing the soil water content (Θ_g) and the change in soil temperature [26]. Assuming that floodwater was in thermal equilibrium with the soil below, heat storage in floodwater was added to soil heat storage:

$$Q_G = Q_{G_{8\text{cm}}} + (\rho_b (C_s + C_w \Theta_g) dz_G + \rho_w C_w dz_{\text{flood}}) \frac{dT_s}{dt}, \quad (1)$$

where ρ_b is the site-specific soil bulk density, ρ_w is the density of water, C_s (840 J kg⁻¹ K⁻¹) and C_w (4180 J kg⁻¹ K⁻¹) are the

soil and water heat capacities, respectively, and dT_s/dt is the change in soil temperature with respect to measurement period. Heat storage is scaled by depth of ground heat flux plates ($dz_G = 0.08$ m) and floodwater depth (dz_{flood}).

Initially, Q^* was measured well above the canopy with a vented and cross-calibrated net radiometer (REBS-Q7.1, Radiation and Energy Balance, Inc., Seattle, WA). As with the 3SEC systems, radiometry measurements were upgraded as funding became available. First, a CM3 pyranometer measuring downwelling shortwave radiation (Q_s) was added until net radiometers could be replaced. Both saltcedar sites were upgraded with CNR1 component radiometric sensors, measuring both incoming and outgoing radiative fluxes in the shortwave and thermal ranges (Kipp & Zonen B.V., Delft, Netherlands). The lighter and less expensive CNR2 model, which measures net shortwave and net long wave radiative fluxes, replaced the Q7.1 at the cottonwood long-IFI site just weeks before a burned cottonwood crown toppled the tower. All radiometers were placed near the top of the tower to minimize shading effects.

2.3. Flux Data Processing

2.3.1. QA/QC. Prior to and following application of standard flux corrections, nonphysical observations were flagged for removal from analysis (e.g., relative humidity measurements of less than zero or products of overrotation). Out-of-range measurements were also discarded (e.g., $|Q_E| > 1000$). Data from periods of low turbulence, particularly at night when the friction coefficient (u^*) was less than 0.25 m s^{-1} [27], were retained but flagged for later analysis.

2.3.2. Turbulent Fluxes and Corrections. Vertical Q_E and virtual heat flux (Q_{H_v}) were calculated as the 30 min covariance between 10 Hz measurements of deviations from mean of vertical wind speed (w') and specific humidity (q'), or virtual (potential) temperature (T_v), respectively [11]. Positive values were indicative of fluxes leaving the surface for Q_G , Q_H , and Q_E . Q^* was positive when downward radiative fluxes were larger than upward fluxes (i.e., Q^* was positive toward the surface).

T_v is the temperature at which dry air has the same density as moist air, and it is always larger than the temperature of unsaturated moist air (T). To obtain accurate measurements of Q_H in moist air, T_v or Q_{H_v} must be converted to T or Q_H , respectively [28]. Because 10 Hz observations were not available from systems utilizing CR23X dataloggers, correction of T_v' was not practical. Using an independent

measure of T , Q_H was computed from Q_{Hv} following the Campbell Scientific, Inc., open path eddy covariance manual:

$$Q_H = \left(\frac{\bar{T}}{\bar{T}_v} \right) \left(Q_{Hv} - \frac{0.51 \cdot C_p \cdot \rho_m \cdot \mathfrak{R}_m \cdot \bar{T}^2}{P \cdot \lambda} \right), \quad (2)$$

where the overbars represent 30 min averages, C_p [$\text{J kg}^{-1} \text{K}^{-1}$] is the specific heat capacity of moist air, ρ_m [kg m^{-3}] is the density of moist air, \mathfrak{R}_m [$\text{kPa m}^3 \text{K}^{-1} \text{kg}^{-1}$] is the gas constant for moist air, and λ [J kg^{-1}] is the latent heat of vaporization ($2.501 - 0.00237T$ [$^{\circ}\text{C}$]). Each of C_p , ρ_m , and \mathfrak{R}_m were determined from the associated constants for dry air: $C_p = C_{pd}(1 + 0.84q)$, $\rho_m = P/(\mathfrak{R}_m T)$, and $\mathfrak{R}_m = \mathfrak{R}(1 + 0.608q)$ where $C_{pd} = 1004.67$ [$\text{J kg}^{-1} \text{K}^{-1}$] and $\mathfrak{R} = 0.287$ [$\text{kPa m}^3 \text{K}^{-1} \text{kg}^{-1}$]. Both T and T_v are in [K] except where otherwise noted, and q is in [g g^{-1}].

Corrections for top-of-canopy conditions were applied using the preceding constants for moist air. The first correction was performed for KH20 systems. The KH20 correction was a two-step process: (1) the oxygen correction to discount the absorption of oxygen by the krypton beam and (2) a second-order polynomial correction for the effect of atmospheric humidity on the calibration coefficient k_w . The remaining corrections were performed on data from all systems.

Two-dimensional rotation to natural wind coordinates was performed upon each 30 min observation to force stationarity in vertical wind speed (i.e., $\bar{w} = 0$), in cross-wind speed (i.e., $\bar{v} = 0$), and in the covariance between streamwise and cross-stream wind speeds (i.e., $\overline{u'v'} = 0$) [29]. Observations were considered overrotated and removed from analysis when $Q_E < -100$ or $Q_H < -300 \text{ W m}^{-2}$. Frequency response corrections were performed using the spectral transfer function of Massman and Clement [30]. Atmospheric stability was determined as $\zeta = (z-d)/L$, where z is the sensor height, d is the zero plane displacement, L is the Obukhov length, and d is assumed to be two-thirds of the canopy height h_c [31]. Data were then corrected for the effect of heat and water fluxes on atmospheric density measurements [32].

2.4. Energy Fluxes and ET. Cloud-free and gap-free days were identified for drought index comparisons to avoid the confounding effects of cloud properties on fluxes. Single representative 24-hour periods were chosen in which 30 min observations of Q^* , Q_E , Q_H , and Q_G were evaluated. In multiyear comparisons, dates were chosen that were within the same 7–10-day period, with a preference for the same day of the year when possible. Responses of Q_E to Q^* , representing the evaporative fraction (EF), were evaluated using 60 min average fluxes during and including all daytime observations between July 17 and August 16. Data gaps were not filled to avoid autocorrelation with model training data.

To compare ET amongst sites Q_E was accumulated on each day that did not contain data gaps. Next, a higher-order polynomial was fit each year to daily ET, which averaged ET

across intraseasonal variations and clusters of data gaps [11]. Total annual ET was determined as the cumulative fitted ET.

2.5. Hydroclimate and Statistical Analyses. The state of the hydroclimate, from extremely dry to extremely wet, was determined from the Palmer hydrologic drought index (PHDI, <http://www.ncdc.noaa.gov>). As these sites are located within GDEs, which obtain their water from snowmelt and rainfall in the upper catchments, both local (central valley New Mexico) and regional (central valley, central highlands, and northern mountains in New Mexico and the Colorado headwaters) PHDI values were used. PHDI represents an approximate balance between moisture supply (precipitation and run-on) and demand (ET and runoff). Neutral conditions are defined as $-2 < \text{PHDI} < 2$. Moderately dry conditions are indicated at or below -2 ; they become severe drought at -3 , and extreme drought begins at PHDI values below -4 . Wet conditions are similarly scaled in positive values (moderately wet, very wet, and extremely wet). PHDI commonly varies between both extremes in semiarid environments (e.g., Figure 1).

Drought and wet conditions were compared during years when local or regional PHDI was at least moderate (Figure 1). Thus, these comparisons were performed in June 2001 (wet) and June 2003 (dry) (Table 2). All drought comparisons were made within one month of the summer solstice when Q_s was maximal. The regressions between Q_E and Q^* (EF) and between Q^* and Q_s were compared across sites and climatic conditions using analysis of covariance (Matlab r2009, Mathworks, Natick, Massachusetts, USA). Analysis of variance was used to compare annual totals of ET amongst the four sites. A significance level of 0.05 was chosen for all statistical inferences.

3. Results

3.1. Water Budgets for the Four Sites. Annual rainfall ranged from 200 to 270 mm y^{-1} across all four sites (Figure 2). Mean ecosystem ET was much larger than average rainfall (by a factor of 2.5 to 6) across all four sites and in all years. Mean annual ecosystem ET was significantly smaller in the saltcedar long-IFI forest than the saltcedar short-IFI and cottonwood long-IFI forests (site $F = 24.7$; $\text{df} = 7$ and 40 ; $p < 0.0001$; Figure 2). The small number of years that the tower operated in the cottonwood short-IFI forest (Table 1) reduced the statistical power of the comparison; thus mean annual ET of the cottonwood short-IFI site was not statistically different from any of the other three sites (Figure 2).

Monthly ET was large at mid-year, reaching between 100 and 300 mm month^{-1} (Figure 3) and often exceeded annual rainfall at some sites (e.g., the saltcedar short-IFI site; Figure 3). However, differences in mean annual ET across all years (Figure 2) were reflected in differences amongst the peak values of monthly ET across the four sites (Figure 3). Amongst the cottonwood forests, peak monthly ET varied more across years at the short-IFI site than in the forest with a long IFI (Figure 3). At the cottonwood long-IFI site, ET during the growing season was constant or slightly declining until 2007, after the fire on June 16, 2006, that reduced

TABLE 2: Surface conditions on representative cloud-free days.

Condition	Site	Date	PHDI ^a	β^b	DGW ^c (cm)	Θ_m^d	ET (mm)
Wet	CW—long-IFI	03-Jun-01	3.44	-0.36	146	n.o.	7.2
Dry	CW—long-IFI	06-Jun-03	-1.34	0.08	170	0.23	6.8
Wet	CW—short-IFI	05-Jun-01	3.44	-0.26	89	n.o.	7.1
Dry	CW—short-IFI	14-Jun-03	-1.34	-0.28	140	0.30	6.2
Wet	SC—long-IFI	04-Jun-01	3.44	0.51	190	n.o.	4.4
Dry	SC—long-IFI	12-Jun-03	-1.34	0.71	210	0.05	4.3
Wet	SC—short-IFI	02-Jun-01	3.44	-0.10	187	n.o.	8.5
Dry	SC—short-IFI	10-Jun-03	-1.34	0.27	180	0.07	7.3
Flooded	SC—short-IFI	07-Jun-05	5.84	0.18	-53	0.57	9.1

^a0 = normal, -2 = moderate drought, 3 = very wet.

^b β : daily average.

^cNegative values represent flood water depth.

^dMeasured at the surface (0–10 cm).

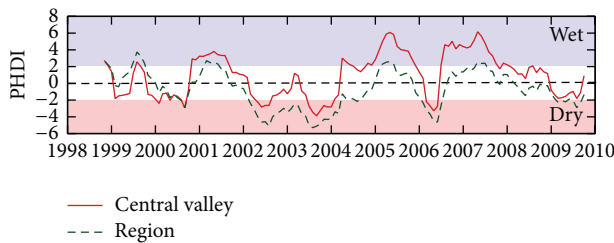


FIGURE 1: Monthly Palmer hydrologic drought index (PHDI) values averaged across the study area (central valley, solid line) and averaged across the central valley and upstream catchment (region, broken line).

the surface area of green, transpiring leaves. By contrast, monthly ET increased annually between 2003 and 2008 at both saltcedar sites, although that trend reversed in 2009 (Figure 3).

The maximum of daily ET was 9.5 mm d^{-1} in cottonwood forests and 12.5 mm d^{-1} at saltcedar-dominated sites. ET from the cottonwood short-IFI forest was substantially smaller than in the cottonwood long-IFI forest in three out of the four years that measurements overlapped (2000, 2002, and 2003), although individual days occurred in which large ET fluxes were released from the cottonwood short-IFI forest ($>9 \text{ mm d}^{-1}$, Figure 3).

3.2. Radiation: Solar and Q^* . At all sites, Q^* was strongly related to solar radiation (Q_s) (Table 3). With only one exception, all slopes and intercepts of the relationship between Q^* and Q_s were significantly different from the global values (site $\times Q_s$; $F = 8297$; $df = 11$ and $125,175$; $p < 0.0001$). These slopes were larger in short-IFI sites (0.80 to 0.83) than long (0.73 to 0.79) (Table 3). Daily peak Q^* at all sites was between 700 and 800 W m^{-2} , with little interannual variation in peak Q^* regardless of drought or flood condition (Figures 4 and 5).

When averaged across all years, total daily Q^* was largest in the summer and smallest in the winter (Figure 6). Maximal annual Q^* exceeded $20 \text{ MJ m}^{-2} \text{ day}^{-1}$ at two sites: saltcedar

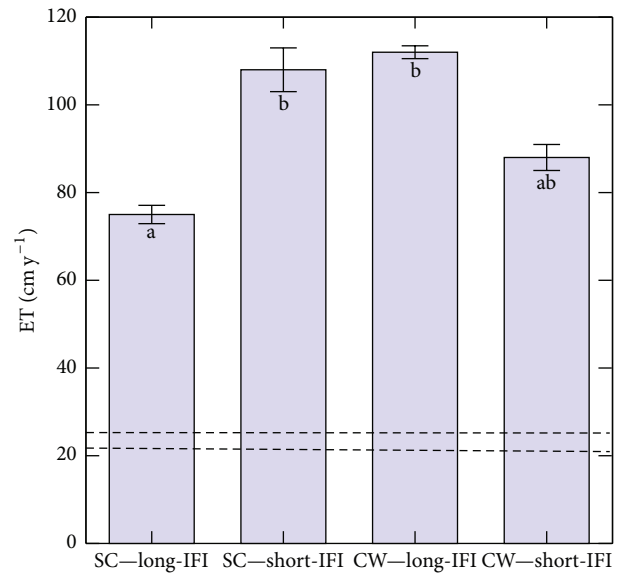


FIGURE 2: Annual evapotranspiration (ET) \pm standard error. Values with the same letter are not significantly different ($p < 0.05$). The two horizontal dashed lines represent the range in annual average rainfall in the central valley of the Middle Rio Grande [3].

short-IFI ($20.3 \text{ MJ m}^{-2} \text{ d}^{-1}$) and cottonwood short-IFI ($20.2 \text{ MJ m}^{-2} \text{ d}^{-1}$; Figure 6). During winter (November–February), Q^* was typically low but highly variable at all sites (Figure 6). At the cottonwood long-IFI site, winter Q^* was large (up to $16.6 \text{ MJ m}^{-2} \text{ d}^{-1}$) and highly variable (Figure 6).

3.3. Convection: Turbulent Latent and Sensible Heat Fluxes. The magnitude of Q_E exceeded Q_H ($-1 < \beta < 1$) at all sites (Table 2). Evaporative cooling, indicated when Q_H was directed toward the surface (i.e., $\beta < 0$), was common in these riparian GDEs during extremely wet periods, except at the saltcedar long-IFI site where β was 0.5 (Table 2). As these riparian sites dried, β increased except at the short-IFI site dominated by cottonwood, where β remained negative (Table 2). At the cottonwood (dry) and saltcedar short-IFI

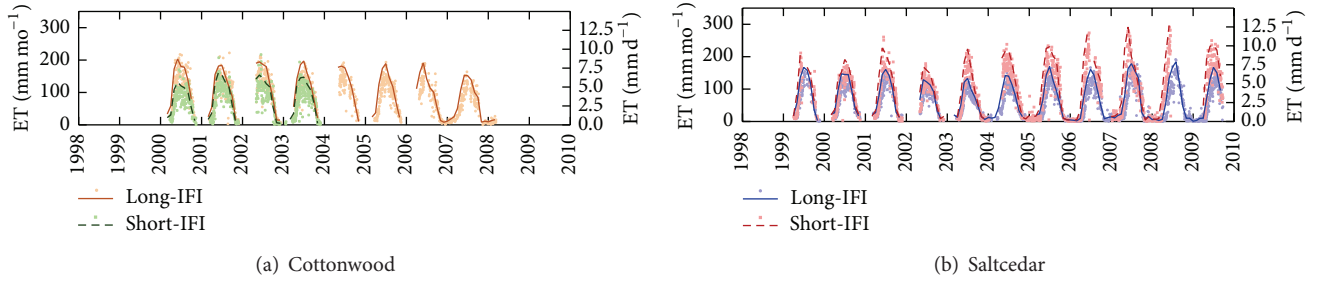


FIGURE 3: Total monthly (lines) and daily (symbols) ET at cottonwood (a) and saltcedar (b) sites. Long IFI is indicated by the solid line and small circles. Sites with a short IFI are indicated by the broken line and small squares. The first day of each year is indicated along the x -axis.

TABLE 3: Least squares regression model coefficients between 30 min observations of solar (Q_s) and net radiation (Q^*), $Q^* = mQ_s + b$. Slopes (m) marked by an asterisk are not significantly different ($p < 0.05$).

Site	Date range ^a	r^2	m	b	α^b
CW—long-IFI	26-Apr–30-Sep-2006 ^c	0.990	0.728*	-76.6	n.o.
	1-May–31-Dec-2007	0.991	0.726*	-48.3	n.o.
SC—long-IFI	1-May–30-Sep-2006	0.992	0.770	-37.0	n.o.
	2007	0.989	0.766	-48.8	n.o.
	2008	0.985	0.789	-63.5	0.11
	1-Jan–24-Sep-2009	0.988	0.796	-63.9	0.10
SC—short-IFI	2007	0.993	0.832	-44.7	n.o.
	9-Apr–24-Sep-2009	0.990	0.823	-57.4	0.12

^aSingle year range: the entire year's data collection fit the same line.

^b α : midday (10.00–14.00 LST) average albedo. n.o.: no observations.

^cData from 15-June-2006 to 18-June-2006 removed following fire; postfire $Q_{\min}^* = -321 \text{ W m}^{-2}$.

(wet) sites, positive Q_H at midday balanced negative Q_H during the evening and early nighttime ($\beta = 0.08$ and -0.1 , resp.; Table 2). In contrast, average daily Q_H was positive at the saltcedar short-IFI site ($\beta = 0.27$ and 0.18 in dry and flooded conditions, resp.; Table 2).

Large positive Q_H occurred at midday in the cottonwood long-IFI (dry), saltcedar long-IFI (wet and dry), and saltcedar short-IFI (dry and flooded) sites (Figures 4 and 5). Peak Q_E was lower during drought than during wet conditions at short-IFI sites, whether dominated by cottonwood or saltcedar (Table 2, Figure 4). At the cottonwood and saltcedar long-IFI sites, Q_E was the same during drought and wet conditions and was equal to or lower than Q_E at the companion short-IFI site during wet conditions (Figure 4). At the saltcedar long-IFI site, Q_E and Q_H were nearly equal at each about 50% of Q^* (Figure 4). When averaged across years, growing season Q_H was negative at both cottonwood sites and at the saltcedar short-IFI site during springtime (Figure 6). Over the course of the year, Q_E was balanced by Q_H : increases in Q_E were reflected by decreases in Q_H (Figure 5). The saltcedar short-IFI site began the growing seasons as a strong

Q_H sink (i.e., $Q_H < 0$) but was at near neutral thermal stratification (i.e., $Q_H \approx 0$) by August (Figure 5). Despite failing to account for canopy storage and inverted fluxes (e.g., $Q_H < 0$), net energy balance (i.e., $\{Q_H + Q_E\}/\{Q^* - Q_G\}$) was 78% in the saltcedar ecosystems and 64% in the cottonwood long-IFI forest.

Daily Q_E was closest to Q^* at the saltcedar short-IFI site (Figure 6). Figure 7 illustrates conversion of Q^* into Q_E at each of the sites during drought and wet conditions. The slope of the Q^* versus Q_E relationship represents the average evaporative fraction (EF). Significant differences in EF were found across sites and conditions (site \times condition \times Q^* ; $F = 72.45$; $df = 11$ and $3,752$; $p < 0.0001$). EF was significantly smaller during drought than wet conditions except at the cottonwood long-IFI site (Table 4). The saltcedar short-IFI site had the largest EF during wet conditions (Table 4).

3.4. Conduction: Q_G and Flood Water Heat Flux. Negligible Q_G was observed at the saltcedar short-IFI site under dry conditions (Figure 4). Instantaneous Q_G at all of the remaining sites in the drought comparison were small but nonnegligible (Figure 4). Small Q_G fluxes were observed under the shade of groundwater-dependent vegetation at all four sites. No relationships were identified between Q_G and depth-to-groundwater (DGW) or Θ_g (Table 2).

Except when the site was flooded, Q_G followed a similar pattern at all sites: Q_G was negligible at night, directed into the soil (i.e., positive Q_G) predominantly in the afternoon and early evening, and then back out of the soil in the morning (Figure 4). The presence of floodwater had its largest effect on Q_G , which showed its largest range under flooded conditions (Figure 5). When floodwaters were present, Q_G was shifted to positive values from midnight to noon and negative for the remainder of the day. Although the magnitude of heat fluxes through floodwater was larger than through dry soil, daily average Q_G was negligible at all sites and across all seasons (Figure 6).

3.5. Impacts of Flooding on Ecohydrology and Forest Water-Use. Peak midday Q^* was slightly larger during inundation than noninundated times. At the flooded saltcedar site, Q^* peaked at 845 W m^{-2} (Figure 5), and this value was the largest observed in the Middle Rio Grande. Heat storage in the soil surface and water column contributed to a daily range in

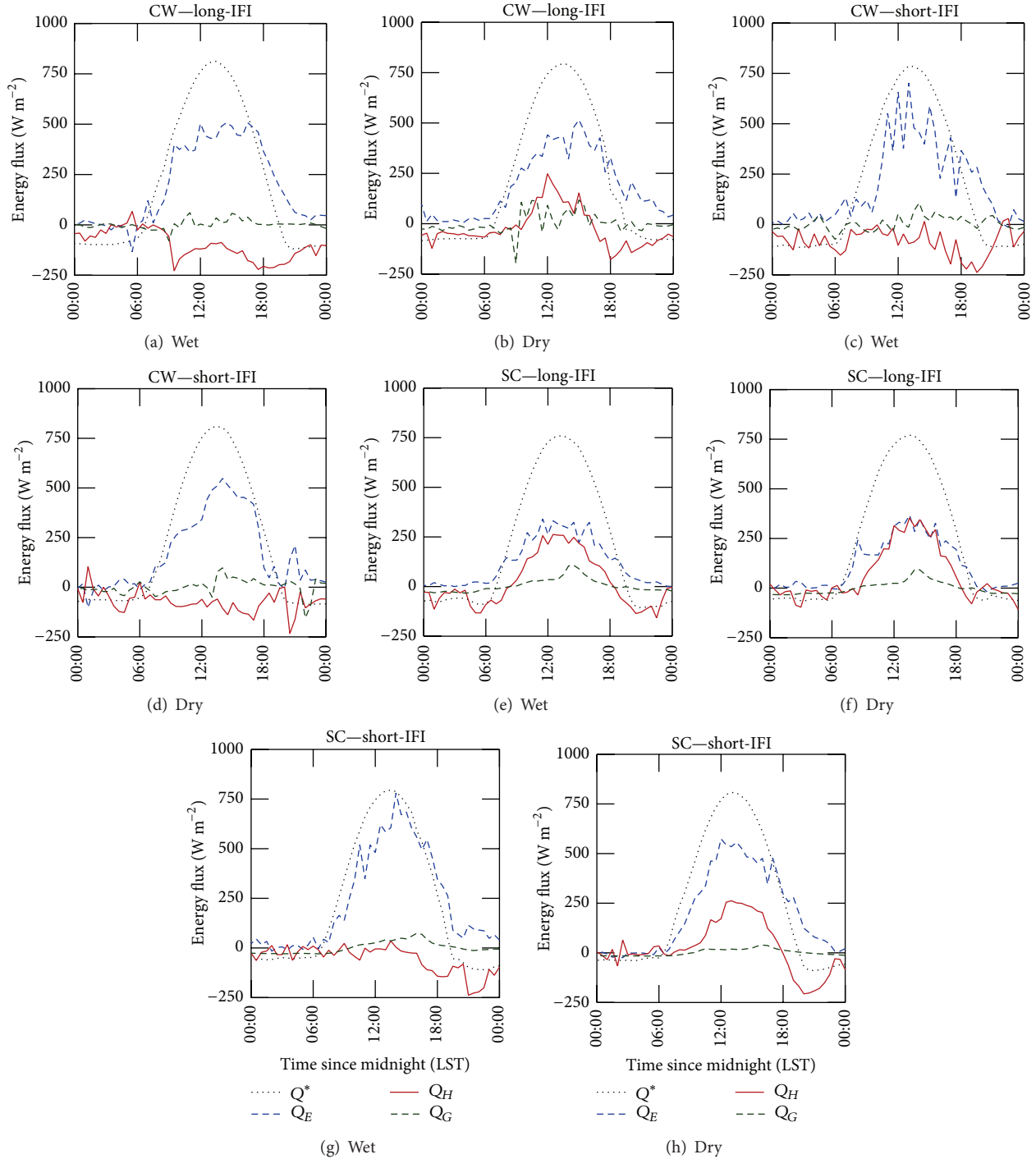


FIGURE 4: Half-hourly average energy fluxes at the four sites (Table 1) under clear sky conditions and wet *versus* dry conditions (Table 2). Energy fluxes are net radiation (Q^* , dotted line), latent heat flux (Q_E , blue dashed line), sensible heat flux (Q_H , red solid line), and ground heat flux (Q_G , green dashed line). CW: cottonwood; SC: saltcedar; IFI: interflood interval.

instantaneous rates of Q_G of -110 to 86 W m^{-2} at the flooded saltcedar site (Figure 5). Nocturnal Q_E was larger during flooding than when the saltcedar short-IFI site was wet or dry (Figures 4 and 5). Total daily Q_E (ET) at the saltcedar site was larger when flooded (9.1 mm d^{-1}) than when wet but not inundated (8.5 mm d^{-1} , Table 2).

4. Discussion

4.1. Characteristics of GDEs: ET and Management. Riparian ecosystems in semiarid regions are sites of large rates of primary production and ET, in contrast to nonriparian, semiarid ecosystems [33, 34], reflecting the influence of an additional

TABLE 4: Analysis of covariance comparing evaporative fraction between sites and drought condition. None of the intercepts \pm standard error are significantly different ($p < 0.05$) from the single line intercept (59.4 ± 2.4). Slopes \pm s.e. with the same letter are not significantly different.

Condition	Site	r^2	Intercept	Slope
Wet	CW—long-IFI	0.60	56.0 ± 7.3	$0.515^{ab} \pm 0.014$
Dry	CW—long-IFI	0.72	50.4 ± 7.6	$0.543^{bc} \pm 0.015$
Wet	CW—short-IFI	0.69	47.3 ± 7.2	$0.478^{ac} \pm 0.016$
Dry	CW—short-IFI	0.66	74.1 ± 7.9	$0.381^d \pm 0.016$
Wet	SC—long-IFI	0.80	70.3 ± 8.5	$0.449^{ad} \pm 0.018$
Dry	SC—long-IFI	0.66	64.1 ± 7.7	$0.280^f \pm 0.016$
Wet	SC—short-IFI	0.76	54.1 ± 7.5	$0.679^e \pm 0.016$
Dry	SC—short-IFI	0.82	60.2 ± 7.5	$0.581^b \pm 0.015$

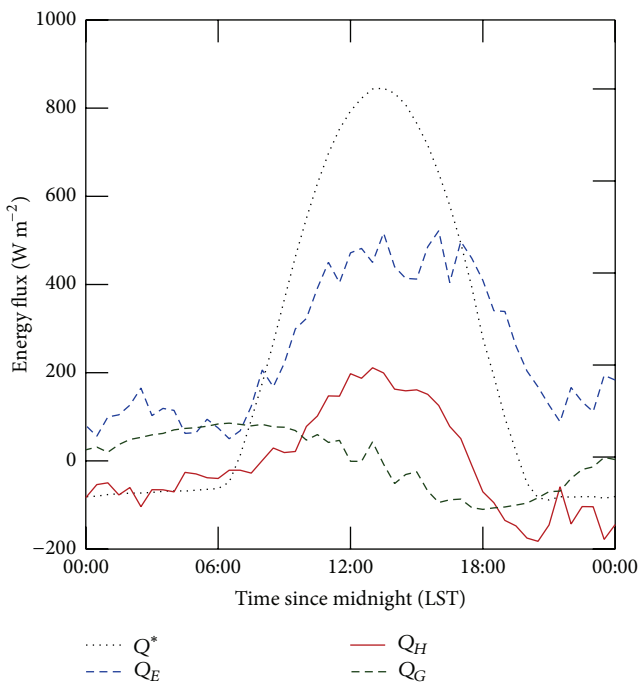


FIGURE 5: Half-hourly average energy fluxes at the inundated saltcedar site (SC—short IFI).

source of water on the ability to fix carbon. However, identification of groundwater-dependent ecosystems (GDEs) in the field is not trivial and typically requires an understanding of the ecohydrology of groundwater-dependent vegetation [35]. One of the key characteristics of GDEs is that ET consistently exceeds annual average precipitation [36]. In the present study, ET from both types of GDEs (cottonwood and saltcedar) was three to six times larger than the annual average precipitation of 200–250 mm (Figure 2), indicating that both types of forests were groundwater-dependent.

We found large differences in ET between the two forest types and flooding regimes, supporting our first hypothesis. Interestingly, ET in the two forest types did not respond to flooding regime in the same way: ET was larger in the saltcedar site with a short IFI, whereas ET tended to be

larger in the cottonwood site with a long IFI. There are two explanations for these divergent responses: (1) saltcedar abundance is favoured by deep groundwater and intermittent flooding [37], while (2) cottonwood ET can be limited by hypoxia and restricted rooting volume during flooding [11]. There are important implications of this finding related to the management of nonnative vegetation for the purposes of water salvage [38]. First, the choice of restoration site for management of nonnative vegetation can be informed by observations of the energy budget, particularly to identify evaporative cooling. Saltcedar sites undergoing evaporative cooling are likely to also have ET rates near the theoretical maximum (12.5 mm d^{-1}), which make these forests a priority candidate for management [39]. Second, evaporative cooling can be maintained through management of native cottonwood forests, and this provides an important ecosystem service in populated areas. For example, conversion of saltcedar capable of large ET rates to sparse cottonwood with an understory of upland vegetation can contribute to reduced ET [38, 40], while maintaining evaporative cooling on a small scale, regardless of climatic conditions.

Water management in the Rio Grande depends upon knowledge of the patterns of ET in the vegetation of riparian GDEs. Cottonwood trees can maintain maximal ET rates if depth-to-groundwater does not exceed about three metres [41]. As long as water supply to the Middle Rio Grande can maintain the riparian aquifer and barring burning of the forests, cottonwood forests will continue to support large daily and monthly rates of ET (Figure 3). By contrast, the hydraulic architecture of saltcedar is highly resistant to drought stress [42]. This promotes survival through dry years, albeit with smaller ET rates, but with increasing ET during subsequent wet years (Figure 3). However, groundwater resources are expected to decline with declining regional snowpack; thus the preferential survival of saltcedar could result in continued strain on the water budget, while native trees would tend to die back due to hydraulic failure [43–45]. The magnitude of ET from saltcedar and its effect on the water budget depend upon the pattern of water supply (drought to deluge) and distribution of short-IFI and long-IFI sites [3]. ET from saltcedar can equal or exceed available energy [46], or ET can equal half of that [19]. Regardless, saltcedar has a more detrimental effect on water budgets than the native xeric vegetation that dominated the Middle Rio Grande riparian corridor over a century ago, before nonnative species invaded and when cottonwood trees were far less prevalent [21, 38].

4.2. Evaporative Cooling. Rates of midday net radiation flux (Q^*) observed in the present study ($750\text{--}825 \text{ W m}^{-2}$) represent some of the largest rates published for vegetated land surfaces (cf. [1, 10, 14, 47–50]). This is partially attributed to the fact that semiarid regions have a preponderance of cloud-free days. Furthermore, our study sites were located in a region with moderate to large radiation and a high temperature regime, which favours large rates of Q^* . However, the groundwater dependency evident for all four sites also contributes to these large values of Q^* because of the reduction of *radiative* cooling that occurs so frequently for

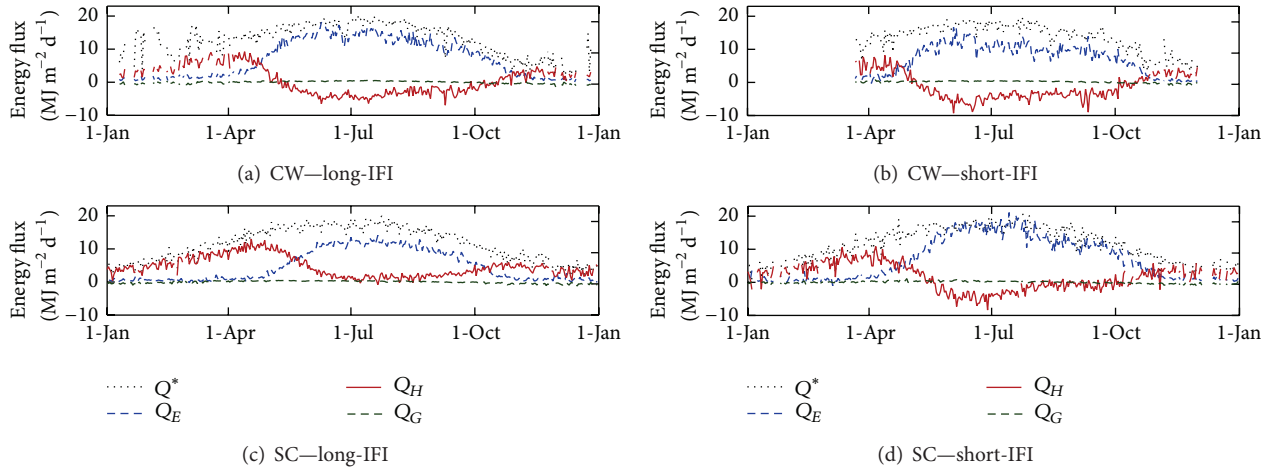


FIGURE 6: Daily total energy fluxes, averaged across all years.

vegetation accessing groundwater on a daily basis. Another characteristic of GDEs is that energy partitioning results in a Bowen ratio that is higher than -1 but less than zero [2]. Thus, we conclude that patterns of ecosystem energy fluxes can be used to differentiate between adjacent GDE and non-GDE systems.

With abundant available moisture and sunlight, *evaporative* cooling of GDE canopies can dominate the energy balance [4, 51–54], consistent with our second hypothesis. The relatively large cottonwood leaves are most likely to establish counter-gradient fluxes of large Q_E and negative Q_H during daytime hours (i.e., evaporative cooling; Figure 4), although Q_H can be a source of available energy in three of the four GDE sites (the exception being the driest saltcedar site, Figure 4). Because of the coupling between Q_E and Q_H in riparian GDEs, evaporative cooling facilitates remote and energy balance-based methodologies to estimate ET [3, 46, 55]. Estimates of ET are urgently required to select sites best suited for restoration and to choose the species composition that will attain the goal of minimizing ET and thereby enhancing water availability in-stream [38, 39] as a matter of securing water resources in the region, which is discussed in detail in the following section.

As leaf temperature and leaf water potential tend to be lower in *Tamarix* than cooccurring native species [56], evaporative cooling at the saltcedar short-IFI site represents cooling of the within-canopy air spaces rather than cooling of individual leaves. Evaporative cooling was restricted in the morning and early afternoon at the cottonwood long-IFI and saltcedar short-IFI sites when exposed to drought (Figure 4), although there was no corresponding decrease in ET in the cottonwood forest. Evaporative cooling was maintained at the cottonwood long-IFI site even though Q_E and ET declined during drought (Table 2 and Figure 4), implying that (i) understory development below the cottonwood canopy was restricted during drought and therefore did not contribute to ET or (ii) cottonwood transpiration during a wet year exceeded the rates required to cool the canopy. Because the latter is unlikely given the year-round proximity of

groundwater at both cottonwood sites, the drought-related decline in ET at the cottonwood short-IFI site was most likely the effect of understory dormancy during drought.

4.3. Hydroclimate and Water Security. Historically, cycles of drought and flooding had a large and recurrent effect on riparian vegetation structure and hydrology. With only one exception (cottonwood long-IFI), ET was lower during drought (Figure 7). Reduced ET indicates that the importance of Q_H increased relative to Q_E in response to drought, as predicted by our third hypothesis, and signified an increase in vegetation stress as ET became insufficient to moderate leaf or canopy temperature (Table 1). In saltcedar forests, seasonal average ET and LAI are strongly coupled to vapour pressure deficit (VPD; [11]), even though saltcedar extracts groundwater from depths of more than 10 m to 25 m to avoid moisture stress. In the present study, drought had a substantial effect on ET only at the saltcedar short-IFI site (Figure 3). In contrast, the proximity of groundwater at the cottonwood sites greatly ameliorated the impact of drought and consequently high ET was maintained throughout extreme drought.

Drought has very important impacts on energy and water budgets; thus drought can detrimentally impact the security of water resources, depending upon vegetation and land use responses to drought [57, 58]. Extended droughts (megadroughts) recur regularly on a 20–70-year cycle throughout southwestern North America due to the climatic influences of the Pacific decadal oscillation (PDO) and Atlantic multi-decadal oscillation (AMO) [59] and at their extremes have resulted in violent conflict (e.g., expulsion of the Spanish by the indigenous Pueblo people during the megadrought of the 1680s; [21]). Current law requires the delivery of a proportional amount of annual streamflow as in-stream deliveries between Colorado, USA, New Mexico, USA, Texas, USA, and Chihuahua, Mexico [17]. Meeting these compact and treaty obligations under current and future hydroclimate might require careful management of native and nonnative vegetation to minimize ET and vegetation density at the expense of reducing evaporative cooling.

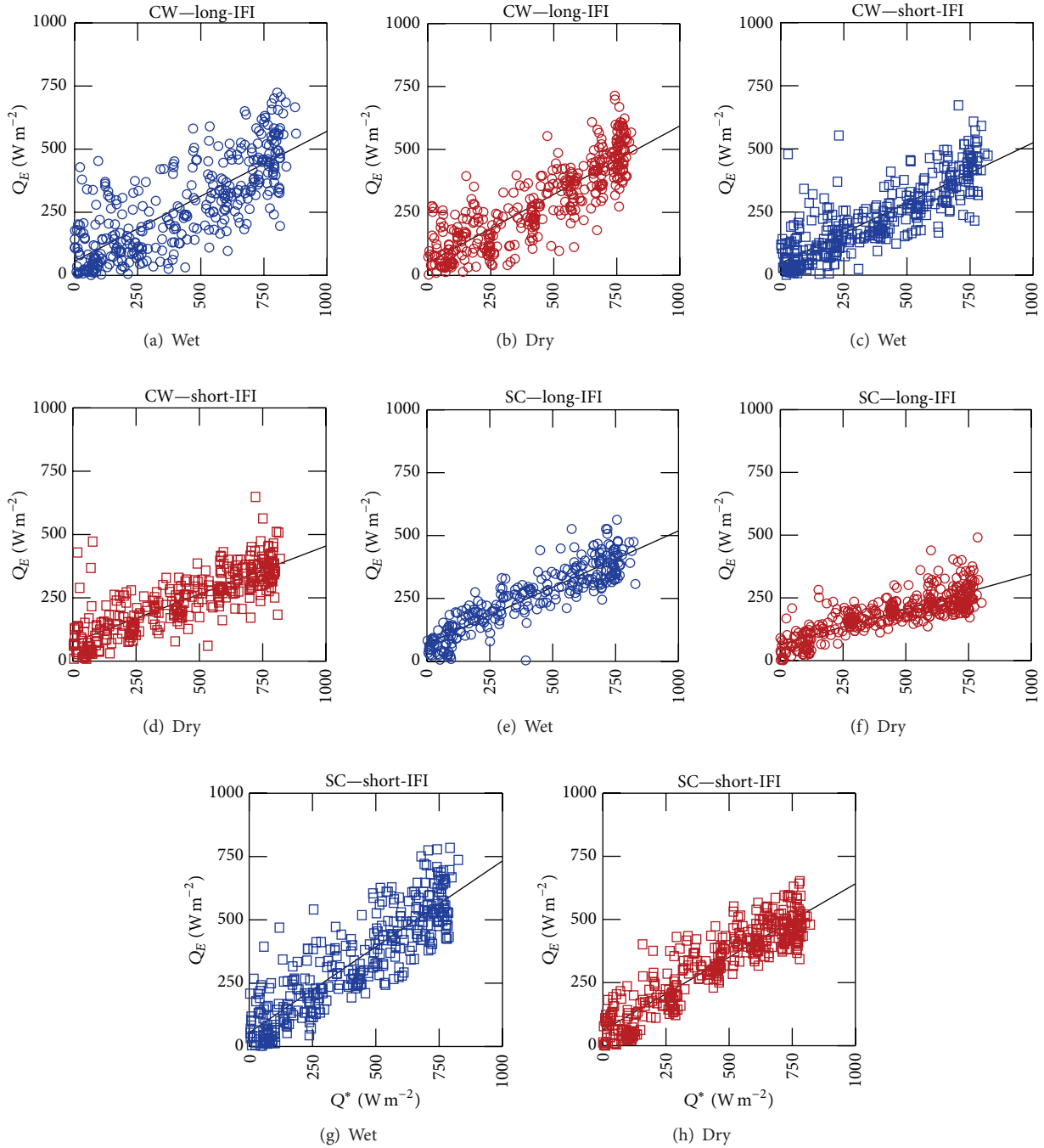


FIGURE 7: Evaporative fraction and the linear relationships between latent heat flux (Q_E) and net radiation (Q^*).

Lastly, we predicted that Q_G would be negligible except under flooded conditions. Indeed, Q_G was negligible on a daily average under all conditions, including flooding, and tended to be small on a diel basis, except under flooding. Flooding resulted in increased evaporation and vegetation stress such that Q_H , Q_G , and nightly Q_E were increased but daytime Q_E was reduced (Figure 5). The amount of energy absorbed by floodwater (i.e., the magnitude of Q_G) in the saltcedar forest was similar to bare soil (data not shown)

because leaf-out was delayed and the amount of radiation intercepted by the canopy was minimized. The combination of delayed leaf-burst, reduced transpiration and growth of adventitious roots contributed to avoiding flooding stress in saltcedar at these sites. In contrast, cottonwood had achieved full LAI development during spring flooding, thereby suppressing evaporation from the floodwaters by intercepting a larger fraction of Q_s [11]. The effects of flooding on the water budget of saltcedar were short-lived because physiological

and ET responses of saltcedar to drought were temporary, whilst ET continued to follow a 4-5-year increasing trend [39].

5. Conclusions

GDEs in semiarid regions are characterised by abundant access to sunlight and water and are distributed as ribbons of enhanced water and energy fluxes. We found that sites dominated by cottonwood or saltcedar exhibited rates of ET that exceeded rainfall by 250% to 600%, strongly supporting the conclusion that these sites were groundwater-dependent. Differences in ET amongst cottonwood and saltcedar forests were related to patterns of energy fluxes (e.g., the efficiency of the conversion of Q^* to Q_E , EF) induced by differences in flooding regime and vegetation stress responses to atmospheric VPD. Consequently, the hydrology of riparian GDEs depends upon the feedback between water and energy fluxes in combination with the spatial distribution of native and nonnative groundwater-dependent vegetation.

Controlling the expansion of high water-using saltcedar forests is key for management of water resources and for maintaining small refugia for parklands of sparse cottonwood and an understory of xeric shrubs and grasses. In this way, the benefits of evaporative cooling can be partially decoupled from an excessive load on the water budget. Excessive ET, especially at the higher end, impacts energy exchange through evaporative cooling, which is diagnosed when the Bowen ratio (i.e., ratio of sensible and latent heat fluxes, Q_H/Q_E) is between negative one and zero (i.e., $-1 < \beta < 0$). Evaporative cooling of the canopy alleviates stress due to high air temperature (1) through direct reduction of leaf temperature in cottonwood or (2) indirectly through reduction of canopy air temperature in saltcedar, which is microphyllous (i.e., has small leaves) such that each individual leaf has a negligible boundary layer and is thus in thermal equilibrium with canopy airspaces. Low leaf temperature limits radiative cooling, which contributes to particularly high values of net radiation (Q^*).

Patterns of energy fluxes amongst GDEs provided a valuable diagnostic tool for evaluating ecosystem stress and hydrological processes. With only one exception, imposition of hydrologic drought reduced evaporative fraction (EF) in these sites (Table 4). With the shallow water tables of the northern and central Middle Rio Grande, native cottonwood maintained high ET and canopy cooling, thereby avoiding imposition of atmospheric heat stress. In the nonnative vegetation (saltcedar), no midday reduction in latent heat flux (Q_E) was observed during drought, whilst reductions of ET and evaporative cooling were temporary, which minimised differences in the water budget between the native and nonnative riparian forests over the long term (Figure 2). Likewise, flooding had large but transient effects on water and energy fluxes. Flooding caused reduced transpiration and shutdown of evaporative cooling and increased evaporation.

Symbols and Abbreviations

R_m : Gas constant for moist air [$\text{kPa kg}^{-1} \text{K}^{-1}$]

α :	Solar albedo [—]
β :	Bowen ratio [—]
ζ :	Stability coefficient [—]
Θ :	Soil moisture content [—]
Θ_g :	Gravimetric soil moisture [$\text{kg H}_2\text{O kg}^{-1}$ soil]
Θ_v :	Volumetric soil moisture [$\text{m}^3 \text{H}_2\text{O m}^{-3}$ soil]
λ :	Latent heat of vaporisation [J kg^{-1}]
ρ_d :	Soil bulk density [g cm^{-3}]
ρ_w :	Density of water [g cm^{-3}]
ρ_m :	Density of moist air [kg m^{-3}]
C_p :	Heat capacity of moist air [$\text{J kg}^{-1} \text{K}^{-1}$]
C_s :	Heat capacity of mineral soil [$\text{J kg}^{-1} \text{K}^{-1}$]
C_w :	Heat capacity of water [$\text{J kg}^{-1} \text{K}^{-1}$]
CW:	Cottonwood, <i>Populus deltoides</i>
d :	Zero-plane displacement height [m]
DGW:	Groundwater depth [cm]
EC:	Eddy covariance
EF:	Evaporative fraction [—]
ET:	Evapotranspiration [mm d^{-1} , cm y^{-1}]
GDE:	Groundwater-dependent ecosystem
h_c :	Canopy height [m]
IFI:	Interflood interval
IRGA:	Infrared gas analyser
k_w :	KH20 calibration coefficient [$\text{m}^3 \text{g}^{-1} \text{cm}^{-1}$]
L :	Obukhov length [m]
non-GDE:	Ecosystem that is not groundwater-dependent
P :	Barometric pressure [kPa]
PHDI:	Palmer hydrological drought index [—]
q :	Specific humidity [g g^{-1}]
Q^* :	Net radiation flux [W m^{-2} , $\text{MJ m}^{-2} \text{d}^{-1}$]
Q_E :	Flux of latent heat [W m^{-2} , $\text{MJ m}^{-2} \text{d}^{-1}$]
Q_G :	Flux of heat conducted into the ground [W m^{-2} , $\text{MJ m}^{-2} \text{d}^{-1}$]
Q_H :	Flux of sensible heat [W m^{-2} , $\text{MJ m}^{-2} \text{d}^{-1}$]
Q_{Hv} :	Flux of virtual sensible heat [W m^{-2}]
Q_s :	Flux of incident shortwave radiation [W m^{-2}]
SC:	Saltcedar, <i>Tamarix chinensis</i>
T :	Temperature [$^{\circ}\text{C}$, K]
T_s :	Soil temperature [$^{\circ}\text{C}$, K]
T_v :	Virtual temperature [$^{\circ}\text{C}$, K]
u :	Horizontal streamwise wind speed [m s^{-1}]
u^* :	Friction coefficient [m s^{-1}]
v :	Horizontal crosswind speed [m s^{-1}]
VPD:	Vapour pressure deficit [kPa]
w :	Vertical wind speed [m s^{-1}]
z :	Height or depth [m].

Conflict of Interests

The authors declare that there is no conflict of interests regarding the publication of this paper.

Acknowledgments

The authors would like to thank Steve Bowser, Daniel Cooper, John Prueger, William Eichinger, David Gutzler,

Salim Bawazir, Manuel Molles, Jennifer Schuetz, Clifford Crawford, and Jennifer Shah for their invaluable assistance. In addition, they would like to thank the anonymous reviewer for comments that were helpful in improving this paper. They would like to further thank the following agencies for granting permission to establish these sites: The City of Albuquerque Open Spaces Division, the New Mexico State Land Office, the Middle Rio Grande Conservancy District, New Mexico State Game and Fish, the Sevilleta NWR, and Bosque del Apache NWR. Further appreciation is offered to the Sevilleta Long-Term Ecological Research program, the Bosque Hydrology Group, and the interagency ET workgroup for their ongoing interest and collaboration. This research was funded by NASA award NAG5-6999, the US FWS Bosque Initiative, a US BoR Endangered Species Act research grant, the State of New Mexico Interstate Stream Commission, and an NSF-EPSCoR Research Infrastructure Improvement Award, and NSF DEB#0080529/DEB#0217774 to the Sevilleta Long-Term Ecological Research program (SEV717).

References

- [1] D. D. Baldocchi and C. A. Vogel, "Energy and CO₂ flux densities above and below a temperate broad-leaved forest and a boreal pine forest," *Tree Physiology*, vol. 16, no. 1-2, pp. 5–16, 1996.
- [2] K. Wilson, D. Baldocchi, M. Aubinet et al., "Energy partitioning between latent and sensible heat flux during the warm season at FLUXNET sites," *Water Resources Research*, vol. 38, p. 1294, 2002.
- [3] C. N. Dahm, J. R. Cleverly, J. E. A. Coonrod, J. R. Thibault, D. E. McDonnell, and D. J. Gilroy, "Evapotranspiration at the land/water interface in a semi-arid drainage basin," *Freshwater Biology*, vol. 47, no. 4, pp. 831–843, 2002.
- [4] O. C. Acevedo, O. L. L. Moraes, R. da Silva et al., "Surface-to-atmosphere exchange in a river valley environment," *Journal of Applied Meteorology and Climatology*, vol. 46, no. 8, pp. 1169–1181, 2007.
- [5] D. I. Cooper, W. E. Eichinger, J. Archuleta et al., "Spatial source-area analysis of three-dimensional moisture fields from lidar, eddy covariance, and a footprint model," *Agricultural and Forest Meteorology*, vol. 114, no. 3-4, pp. 213–234, 2003.
- [6] D. I. Cooper, W. E. Eichinger, J. Kao et al., "Spatial and temporal properties of water vapor and latent energy flux over a riparian canopy," *Agricultural and Forest Meteorology*, vol. 105, no. 1-3, pp. 161–183, 2000.
- [7] F. Kreith and M. S. Bohn, *Principles of Heat Transfer*, West Publishing Company, Saint Paul, Minn, USA, 5th edition, 1993.
- [8] T. Foken, "The energy balance closure problem: an overview," *Ecological Applications*, vol. 18, no. 6, pp. 1351–1367, 2008.
- [9] W. P. Kustas, J. H. Prueger, J. L. Hatfield, K. Ramalingam, and L. E. Hipps, "Variability in soil heat flux from a mesquite dune site," *Agricultural and Forest Meteorology*, vol. 103, no. 3, pp. 249–264, 2000.
- [10] G. G. Burba, S. B. Verma, and J. Kim, "Surface energy fluxes of *Phragmites australis* in a prairie wetland," *Agricultural and Forest Meteorology*, vol. 94, no. 1, pp. 31–51, 1999.
- [11] J. R. Cleverly, C. N. Dahm, J. R. Thibault, D. E. McDonnell, and J. E. A. Coonrod, "Riparian ecohydrology: regulation of water flux from the ground to the atmosphere in the Middle Rio Grande, New Mexico," *Hydrological Processes*, vol. 20, no. 15, pp. 3207–3225, 2006.
- [12] R. Leuning, E. van Gorsel, W. J. Massman, and P. R. Isaac, "Reflections on the surface energy imbalance problem," *Agricultural and Forest Meteorology*, vol. 156, pp. 65–74, 2012.
- [13] N. Kalthoff, M. Fiebig-Wittmaack, C. Meißner et al., "The energy balance, evapo-transpiration and nocturnal dew deposition of an arid valley in the Andes," *Journal of Arid Environments*, vol. 65, no. 3, pp. 420–443, 2006.
- [14] A. P. Sturman and H. A. McGowan, "Observations of dry season surface energy exchanges over a desert clay pan, Queensland, Australia," *Journal of Arid Environments*, vol. 73, no. 1, pp. 74–81, 2009.
- [15] M. R. Prater and E. H. DeLucia, "Non-native grasses alter evapotranspiration and energy balance in Great Basin sagebrush communities," *Agricultural and Forest Meteorology*, vol. 139, no. 1-2, pp. 154–163, 2006.
- [16] B. J. Creel, *The Rio Grande Compact: It's the Law!*, Water Resources Research Institute, Las Cruces, NM, USA, 1999.
- [17] S. Kelly, I. Augusten, J. Mann, and L. Katz, "History of the Rio Grande reservoirs in New Mexico: legislation and litigation," *Natural Resources Journal*, vol. 47, no. 3, pp. 525–613, 2007.
- [18] R. B. Jackson, S. R. Carpenter, C. N. Dahm et al., "Water in a changing world," *Ecological Applications*, vol. 11, no. 4, pp. 1027–1045, 2001.
- [19] J. R. Cleverly, C. N. Dahm, J. R. Thibault, D. J. Gilroy, and J. E. A. Coonrod, "Seasonal estimates of actual evapo-transpiration from *Tamarix ramosissima* stands using three-dimensional eddy covariance," *Journal of Arid Environments*, vol. 52, no. 2, pp. 181–197, 2002.
- [20] C. J. Campbell and W. A. Dick-Peddie, "Comparison of phreatophyte communities on the Rio Grande in New Mexico," *Ecology*, vol. 45, no. 3, pp. 492–502, 1964.
- [21] D. Scurlock, "From the Rio to the Sierra: an environmental history of the Middle Rio Grande Basin," General Technical Report RMRS-GTR-5, USDA Forest Service, Rocky Mountain Research Station, Fort Collins, Colo, USA, 1998.
- [22] M. C. Martinet, E. R. Vivoni, J. R. Cleverly, J. R. Thibault, J. F. Schuetz, and C. N. Dahm, "On groundwater fluctuations, evapotranspiration, and understory removal in riparian corridors," *Water Resources Research*, vol. 45, no. 5, Article ID W05425, 2009.
- [23] R. L. Scott, E. A. Edwards, W. J. Shuttleworth, T. E. Huxman, C. Watts, and D. C. Goodrich, "Interannual and seasonal variation in fluxes of water and carbon dioxide from a riparian woodland ecosystem," *Agricultural and Forest Meteorology*, vol. 122, no. 1-2, pp. 65–84, 2004.
- [24] G. C. Topp, J. L. Davis, and A. P. Annan, "Electromagnetic determination of soil water content: measurements in coaxial transmission lines," *Water Resources Research*, vol. 16, no. 3, pp. 574–582, 1980.
- [25] S. J. Zegelin, I. White, and D. R. Jenkins, "Improved field probes for soil water content and electrical conductivity measurement using time domain reflectometry," *Water Resources Research*, vol. 25, no. 11, pp. 2367–2376, 1989.

- [26] E. Malek and G. E. Bingham, "Partitioning of radiation and energy balance components in an inhomogeneous desert valley," *Journal of Arid Environments*, vol. 37, no. 2, pp. 193–207, 1997.
- [27] G. W. Moore, J. R. Cleverly, and M. K. Owens, "Nocturnal transpiration in riparian *Tamarix* thickets authenticated by sap flux, eddy covariance and leaf gas exchange measurements," *Tree Physiology*, vol. 28, no. 4, pp. 521–528, 2008.
- [28] P. Schotanus, F. T. M. Nieuwstadt, and H. A. R. De Bruin, "Temperature measurement with a sonic anemometer and its application to heat and moisture fluxes," *Boundary-Layer Meteorology*, vol. 26, no. 1, pp. 81–93, 1983.
- [29] M. L. Wesely, *Eddy correlation measurements in the atmospheric surface layer over agricultural crops [Ph.D. thesis]*, University of Wisconsin, Madison, Wis, USA, 1970.
- [30] W. Massman and R. Clement, "Uncertainty in eddy covariance flux estimates resulting from spectral attenuation," in *Handbook of Micrometeorology: A Guide for Surface Flux Measurement and Analysis*, X. Lee, W. Massman, and B. Law, Eds., pp. 67–100, Kluwer Academic Publishers, Dordrecht, The Netherlands, 2004.
- [31] M. E. Jensen, R. D. Burman, and R. G. Allen, Eds., *Evapotranspiration and Irrigation Water Requirements*, American Society of Civil Engineers, New York, NY, USA, 1990.
- [32] E. K. Webb, G. I. Pearman, and R. Leuning, "Correction of flux measurements for density effects due to heat and water vapour transfer," *Quarterly Journal Royal Meteorological Society*, vol. 106, no. 447, pp. 85–100, 1980.
- [33] G. P. Malanson, *Riparian Landscapes*, Cambridge University Press, New York, NY, USA, 1993.
- [34] S. D. Smith, R. K. Monson, and J. E. Anderson, *Physiological Ecology of North American Desert Plants*, Springer, Heidelberg, Germany, 1997.
- [35] D. Eamus, R. Froend, R. Loomes, G. Hose, and B. Murray, "A functional methodology for determining the groundwater regime needed to maintain the health of groundwater-dependent vegetation," *Australian Journal of Botany*, vol. 54, no. 2, pp. 97–114, 2006.
- [36] J. Kochendorfer, E. G. Castillo, E. Haas, W. C. Oechel, and U. K. T. Paw, "Net ecosystem exchange, evapotranspiration and canopy conductance in a riparian forest," *Agricultural and Forest Meteorology*, vol. 151, no. 5, pp. 544–553, 2011.
- [37] J. C. Stromberg, S. J. Lite, R. Marler et al., "Altered stream-flow regimes and invasive plant species: the *Tamarix* case," *Global Ecology and Biogeography*, vol. 16, no. 3, pp. 381–393, 2007.
- [38] P. B. Shafroth, J. R. Cleverly, T. L. Dudley et al., "Control of *Tamarix* in the western United States: implications for water salvage, wildlife use, and riparian restoration," *Environmental Management*, vol. 35, no. 3, pp. 231–246, 2005.
- [39] J. Cleverly, "Water use by *Tamarix*," in *Tamarix. A Case Study of Ecological Change in the American West*, A. Sher and M. F. Quigley, Eds., pp. 85–98, Oxford University Press, New York, NY, USA, 2013.
- [40] J. R. Cleverly and G. D. Russo, "Salt cedar control: exotic species in the San Acacia reach," in *Water Resources of the Middle Rio Grande*, L. G. Price, P. S. Johnson, and D. Bland, Eds., pp. 76–79, New Mexico Bureau of Geology and Mineral Resources, Socorro, NM, USA, 2007.
- [41] J. L. Horton, T. E. Kolb, and S. C. Hart, "Physiological response to groundwater depth varies among species and with river flow regulation," *Ecological Applications*, vol. 11, no. 4, pp. 1046–1059, 2001.
- [42] W. T. Pockman and J. S. Sperry, "Vulnerability to xylem cavitation and the distribution of Sonoran desert vegetation," *The American Journal of Botany*, vol. 87, no. 9, pp. 1287–1299, 2000.
- [43] J. L. Horton, T. E. Kolb, and S. C. Hart, "Responses of riparian trees to interannual variation in ground water depth in a semi-arid river basin," *Plant, Cell and Environment*, vol. 24, no. 3, pp. 293–304, 2001.
- [44] S. B. Rood, S. Patiño, K. Coombs, and M. T. Tyree, "Branch sacrifice: cavitation-associated drought adaptation of riparian cottonwoods," *Trees: Structure and Function*, vol. 14, no. 5, pp. 248–257, 2000.
- [45] M. L. Scott, P. B. Shafroth, and G. T. Auble, "Responses of riparian cottonwoods to alluvial water table declines," *Environmental Management*, vol. 23, no. 3, pp. 347–358, 1999.
- [46] D. A. Devitt, A. Sala, S. D. Smith, J. Cleverly, L. K. Shaulis, and R. Hammett, "Bowen ratio estimates of evapotranspiration for *Tamarix ramosissima* stands on the Virgin River in southern Nevada," *Water Resources Research*, vol. 34, no. 9, pp. 2407–2414, 1998.
- [47] S. W. Admiral, P. M. Lafleur, and N. T. Roulet, "Controls on latent heat flux and energy partitioning at a peat bog in eastern Canada," *Agricultural and Forest Meteorology*, vol. 140, no. 1–4, pp. 308–321, 2006.
- [48] A. A. Balogun, J. O. Adegoke, S. Vezhapparambu, M. Mauder, J. P. McFadden, and K. Gallo, "Surface energy balance measurements above an exurban residential neighbourhood of Kansas City, Missouri," *Boundary-Layer Meteorology*, vol. 133, no. 3, pp. 299–321, 2009.
- [49] J. Beringer and N. J. Tapper, "The influence of subtropical cold fronts on the surface energy balance of a semi-arid site," *Journal of Arid Environments*, vol. 44, no. 4, pp. 437–450, 2000.
- [50] G. N. Flerchinger, C. L. Hanson, and J. R. Wight, "Modeling evapotranspiration and surface energy budgets across a watershed," *Water Resources Research*, vol. 32, no. 8, pp. 2539–2548, 1996.
- [51] B. Han, S. H. Lu, and Y. H. Ao, "Analysis on the interaction between turbulence and secondary circulation of the surface layer at Jinta oasis in summer," *Advances in Atmospheric Sciences*, vol. 27, no. 3, pp. 605–620, 2010.
- [52] T. W. Brakke, S. B. Verma, and N. J. Rosenberg, "Local and regional components of sensible heat advection," *Journal of Applied Meteorology*, vol. 17, no. 7, pp. 955–963, 1978.
- [53] S. B. Verma, N. J. Rosenberg, and B. L. Blad, "Turbulent exchange coefficients for sensible heat and water vapor under advective conditions," *Journal of Applied Meteorology*, vol. 17, no. 3, pp. 330–338, 1978.
- [54] F. Qi, M. C. Zhuo, and H. Y. Xi, "Analysis of an oasis microclimate in China's hyperarid zone," *Environmental Geology*, vol. 58, no. 5, pp. 963–972, 2009.
- [55] P. L. Nagler, R. L. Scott, C. Westenburg, J. R. Cleverly, E. P. Glenn, and A. R. Huete, "Evapotranspiration on western U.S. rivers estimated using the Enhanced Vegetation Index from MODIS and data from eddy covariance and Bowen ratio flux

- towers,” *Remote Sensing of Environment*, vol. 97, no. 3, pp. 337–351, 2005.
- [56] J. R. Cleverly, S. D. Smith, A. Sala, and D. A. Devitt, “Invasive capacity of *Tamarix ramosissima* in a Mojave Desert floodplain: the role of drought,” *Oecologia*, vol. 111, no. 1, pp. 12–18, 1997.
- [57] C.-H. Cheng, F. Nnadi, and Y.-A. Liou, “Energy budget on various land use areas using reanalysis data in Florida,” *Advances in Meteorology*, vol. 2014, Article ID 232457, 13 pages, 2014.
- [58] S. Chen, J. Chen, G. Lin et al., “Energy balance and partition in Inner Mongolia steppe ecosystems with different land use types,” *Agricultural and Forest Meteorology*, vol. 149, no. 11, pp. 1800–1809, 2009.
- [59] S. J. Gray, J. L. Betancourt, C. L. Fastie, and S. T. Jackson, “Patterns and sources of multidecadal oscillations in drought-sensitive tree-ring records from the Central and Southern Rocky Mountains,” *Geophysical Research Letters*, vol. 30, no. 6, article 1316, 2003.

Research Article

The Effects of Climate Change on Variability of the Growing Seasons in the Elbe River Lowland, Czech Republic

Vera Potopová,¹ Pavel Zahradníček,² Luboš Türkott,¹ Petr Štěpánek,³ and Josef Soukup¹

¹Department of Agroecology and Biometeorology, Faculty of Agrobiological, Food and Natural Resources, Czech University of Life Sciences Prague, Kamýcka 129, Prague 6-Suchbát, 165 21 Prague, Czech Republic

²Global Change Research Centre AS CR, Bělidla 986/4a, 603 00 Brno, Czech Republic

³Czech Hydrometeorological Institute, Kroftova 43, 616 00 Brno, Czech Republic

Correspondence should be addressed to Vera Potopová; potop@af.czu.cz

Received 9 January 2015; Accepted 10 February 2015

Academic Editor: Marcos Heil Costa

Copyright © 2015 Vera Potopová et al. This is an open access article distributed under the Creative Commons Attribution License, which permits unrestricted use, distribution, and reproduction in any medium, provided the original work is properly cited.

This research aimed to identify an approach for adaptation of agriculture to increased climate variability and projected changes, taking into account regional specificity of climate change. Changes in the timing of growing season (GS) parameters for both observation and models data were computed using daily mean temperatures for three thresholds that correspond to the physiological requirements of the vegetable types. This research included a new assessment of the potential impacts of climate change on the GS of vegetables grown in the Elbe River lowland, one of the largest farmed vegetable regions in Central Europe. To accomplish this, a comprehensive analysis was conducted of the spatiotemporal variability of the date of the beginning of the growing season (BGS), the date of the end of the growing season (EGS), and the length of the growing season (GSL) for the period 1961–2011. In addition, an assessment was made of the potential changes in the dates of the BGS, EGS, and GSL for the Elbe River lowland, simulated using the regional climate models. Prospective areas for growing thermophilic vegetables in the study region were also determined.

1. Introduction

The agricultural sector is increasingly exposed to risks, both environmental and economic, due to the phenomenon of climate change and climate variability. In this context, the identification of the best adaptation options is one of the major challenges to improve the risk management tools in agricultural sector at regional and local levels. The Summary for Policymakers of the Working Group I contribution to the IPCC Fifth Assessment Report shows that the risk of extreme events is growing due to global warming [1]. Climate change is likely to affect agricultural systems very differently in various parts of Europe [2]. In northern areas, climate change may have primarily positive effects through increases in productivity and in the range of varieties grown, while in southern areas the disadvantages of climate change will predominate, with lower harvestable yields, higher yield variability, and a reduction in suitable areas for traditional crops. The results of studies performed in Europe in recent

years have shown consistent increases in temperature and various patterns of precipitation, with widespread increases in northern Europe and rather small decreases in southern Europe [3, 4]. These changes in climate patterns are expected to affect all components of Europe's agricultural ecosystems (e.g., crop suitability, yields, and crop protection). Thus, adaptation strategies should be introduced to reduce the negative effects and exploit the possible positive effects of climate change (e.g., changes in crop species, cultivars, and sowing dates).

Future climate change is projected to increase the length of the growing season [3, 5]. An increase in the length of the growing season, together with warmer climate during the growing season, may increase the potential for growing thermophilic vegetables in open fields in lowland areas in Central Europe and increase the potential number of harvests. For spring crops, climate warming will allow earlier planting or sowing than at present. Earlier planting in spring increases the length of the growing season; thus, earlier planting

using long-season cultivars will increase yield potential if soil moisture is adequate and the risk of heat stress is low [6]. All the reported studies concern Europe, where recent warming has clearly advanced a significant part of the agricultural calendar. Increased temperatures, associated with earlier late spring frost dates and delayed autumn frost dates, are clearly apparent in temperate regions of Europe [3, 7–9]. Advances in production due to earlier springs have been documented for several types of crops [5, 10], and the benefits to viticulture of longer growing seasons have been established [11, 12]. For example, according to [5], the growth stages of wild plants and fruit trees as perennial crops have advanced significantly since the beginning of the 1980s and were, together with true agricultural phases, occurring 1 to 2 weeks earlier by the 2000s. European viticulture has experienced direct effects of climate changes, mainly in terms of shifts in grapevine phenological events and stages. Reference [12], exploring viticulture and climate change relationships in Greece, noted a systematic shift in grape harvest dates (earlier harvests). Similar trends have been observed in Italy. Grape maturity dates have gradually shifted 19 d earlier over the period 1961–2009 for numerous varieties [11].

According to [13], the combination of increased air temperature and changes in the amount and annual cycle of precipitation will lead to further shifts in the area and location of individual agroclimatic zones in Central Europe. It is worth noting that, due to climate change, the breeding of new and improved vegetable crop varieties can lead to an extension of the border areas suitable for the profitable cultivation of vegetables. Some thermophilic vegetables that currently grow mostly in southern Europe (e.g., melons, eggplants, tomatoes, and peppers) can become more suitable for cultivation in lowland areas in Central Europe. The two important field vegetable regions in the Czech Republic are South Moravia and the Elbe River lowlands, in which partially different assortments of vegetables are grown. The Elbe River lowland has traditionally been a region of cultivation of brassica vegetables (kohlrabi, Savoy cabbage, white-headed cabbage, and cauliflower), while South Moravia is a profitable region for thermophilic vegetables (e.g., tomatoes and peppers). These differences in the assortments of cultivated vegetables grown in the two regions are mainly due to differences in the temperature conditions of these regions. In the warmest parts of the Elbe River lowland, growing thermophilic vegetables such as tomatoes (*Solanum lycopersicum* L.) and cucumbers (*Cucumis sativus* L.) are profitable only in warmer years. Based on our previous studies [9, 14], we note that the combination of changes in European agricultural commodities and ongoing climate changes (increases in temperatures) can lead to higher costs for vegetable imports and stricter requirements for the maturity and quality of yields. In addition, favourable national agricultural policies could extend the areas suitable for thermophilic field vegetables from the hottest regions of South Moravia to the Elbe region. In addition to the current assortment of vegetables grown, nontraditional vegetables such as melons (*Cucumis melo* L.) and eggplants (*Solanum melongena* L.) could also be grown.

Vegetable crops are most sensitive to the timing of cold events at the beginning and end of the growing season.

Damage caused by late frosts in the spring or early frosts in the fall is a limiting factor, particularly for vegetables grown in Central Europe. In previous study [9], we examined the variations in the last spring frost, the first fall frost, and the length of the frost-free period for the Elbe River lowland in the Czech Republic as indicators of climate variations in this region. Our results demonstrated shifts toward earlier last spring frosts, later first fall frosts, and longer frost-free periods in the Elbe River lowland. Longer frost-free periods can be particularly beneficial for thermophilic vegetables in lowlands. In terms of the growth of field vegetables, however, a late spring frost remains a risk factor, although the degree of risk has decreased [9].

Despite the observed regional trends in agroclimatic characteristics [9, 14] and the importance of the horticultural sector to the economy of the Czech Republic, there is an utter lack of research on the impacts of climate variability on the assortment of field vegetables grown in the Elbe River lowland. This subject continues to be of interest to agroclimatologists, although the range and yield of vegetable crops grown in Central Europe are primarily controlled by temperature. Therefore, the primary objective of this study was to evaluate the long-term changes in the timing of the growing season (GS) parameters over the Elbe River lowland for 1961–2011 at a high horizontal resolution using daily mean temperatures for three thresholds ($T_{\text{mean}} \geq 5, 10, \text{ and } 15^\circ\text{C}$) that correspond to the physiological requirements of the vegetable types. To provide more information on the potential for extension of the range of vegetables grown, the specific objectives of the present study were (i) to conduct a comprehensive analysis of the spatiotemporal variability of the dates of the beginning (BGS) and end (EGS) of the growing season and the length of the growing season (GSL) for three threshold temperatures for the period 1961–2011; (ii) to assess potential changes in the BGS, EGS, and GSL for three threshold temperatures in the Elbe River lowland as simulated using the regional climate models (ALADIN-Climate/CZ and RegCM) under the A1B SRES scenario (for the periods 2021–2050 and 2071–2100); and (iii) to determine prospective areas for growth of thermophilic vegetables in the study region based on projected climatic data provided by regional climate models.

2. Data and Methods

2.1. Gridded Datasets and Quality Control. The Elbe River lowland is one of the largest and most productive suppliers of vegetables in the Czech Republic (Figure 1). The study was based on gridded 116 grid points' daily series of mean air temperature (T_{mean}) data at a 10 km horizontal resolution for observed (1961–2011) and future (2021–2050 and 2071–2100) climate conditions. A regular gridded network (CZGRIDS, ALADIN-Climate/CZ) established by the Czech Hydrometeorological Institute (CHMI) was applied (Figure 1). High-density gridded datasets allow very precise and detailed delimitation of areas with advanced and/or delayed growing seasons compared with station network datasets. The gridded network was created using the technical series from 268 climatological stations and 774 rain gauge stations in the

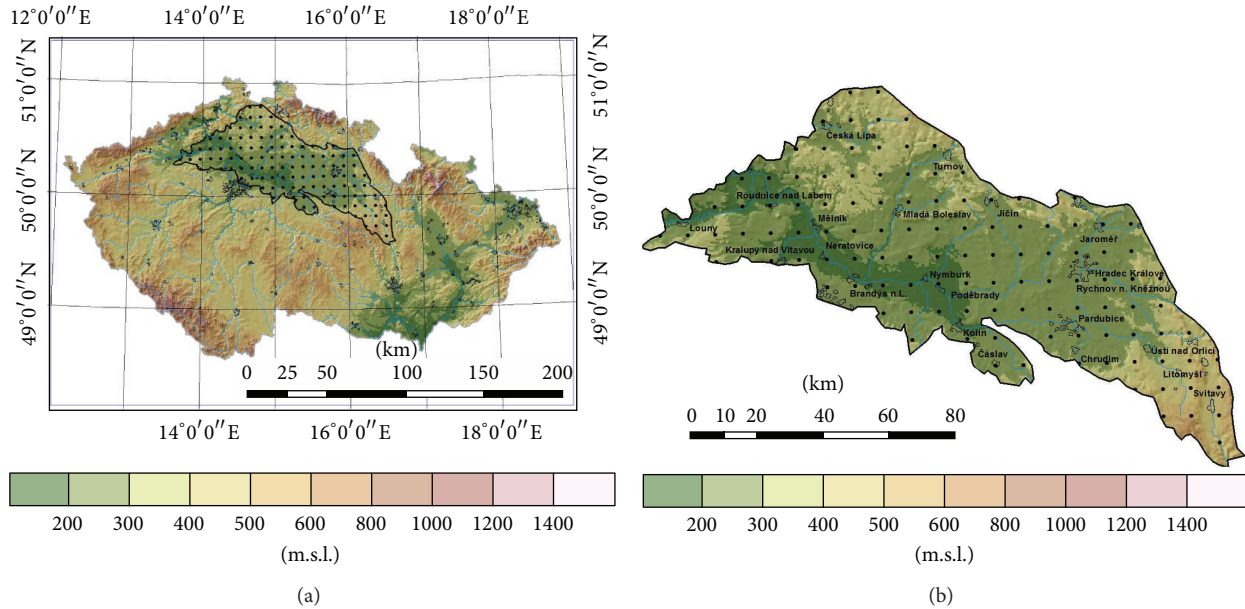


FIGURE 1: The boundaries of Elbe River lowland in the Czech Republic and location of the 116 grid points and their elevation (m a.s.l.) in the Elbe River lowland (a) and the relief map of Elbe River lowland (b).

CHMI network (series after quality control, homogenization, and filling of all missing values in the period 1961–2011). New values for the regular 10×10 km grid network were interpolated from these technical series [15]. The gridding and all data processing, including the analyses described in this paper, were performed using the ProClimDB database software for climatological dataset processing.

A remarkable aspect of vegetable production is that plants function within quite narrow temperature limits. The extreme temperature range is between the killing frost temperature of 0°C and death by heat and desiccation at 40°C [16]. The wide range of vegetables grown in the studied region can be divided into three basic types according to their sensitivity to low temperatures at the onset of the growing season: *thermophilic vegetables* (e.g., tomato, pepper, pumpkins, and cucumber), *cold-resistant vegetables* (e.g., early kohlrabi, summer savoy cabbage, late cauliflower, late cabbage, late carrots, and celeriac), and *frost-resistant vegetables* (e.g., onion and root parsley). From an agronomic point of view, thermophilic vegetables should be planted after 15 May to minimise the risk of frost damage [9]. The critical temperature for thermophilic vegetables after May 15 is $T_{\min} \leq -0.1^{\circ}\text{C}$ [17–19]. A severe last spring frost after April 15 has occurred every second year during the sowing/planting of cold-resistant vegetables at higher altitudes. Typically, the date of planting/sowing of frost-resistant vegetables in the Czech Republic is at the end of March, and a gradual shift occurs from the hottest regions of South Moravia towards the Elbe region.

2.2. Regional Climate Models and Data Postprocessing. Additionally, the ALADIN-Climate/CZ and RegCM regional climate models (RCMs) were adopted to calculate possible shifts in the start, end, and length of the climatological growing season under the SRES A1B scenario for two future periods

(2021–2050 and 2071–2100) over the Elbe lowland. SRES scenario A1B is a baseline scenario referred to in [19]. We used two different RCMs, which were driven by two different global circulation models (GCM), namely, ARPÉGE-Climate [20] and ECHAM5 [21].

The RegCM model was originally developed [22] and then augmented and used in various reference and scenario simulations [23, 24]. RegCM family using RegCM transient ENSEMBLES run for whole Europe currently in 25 km resolution driven by transient run of ECHAM5, but within CECILIA-FP6 Project (Central and Eastern Europe Climate Change Impact and Vulnerability Assessment) was developed RegCM in 10 km resolution, because is important for impact studies in regional scale [25].

ALADIN-Climate/CZ performs quite well in comparison to the other RCMs in impact studies [26, 27]. The model is able to capture the main features of the present climate of the Czech Republic and works well over smaller areas with rather complex orography (tablelands, valley, and hills), such as the Elbe River lowland. However, it should be always kept in mind that model simulations of future climate conditions involve many uncertainties, and it is necessary to apply some type of postprocessing of model outputs from the RCM simulation before using the results in other applications. Therefore, the observed daily temperature data were first transferred onto a regular grid of the RegCM and ALADIN-Climate/CZ models. Prior to the calculation of the start, end, and length of the climatological growing season for the RegCM simulations forced with the ECHAM5 GCM and ALADIN-Climate/CZ run forced by ARPÉGE-Climate GCM, the daily temperature for each grid point has been bias corrected against the systematic errors induced by the GCM. The bias correction was applied to the scenario runs. The bias correction method is based on variable correction using

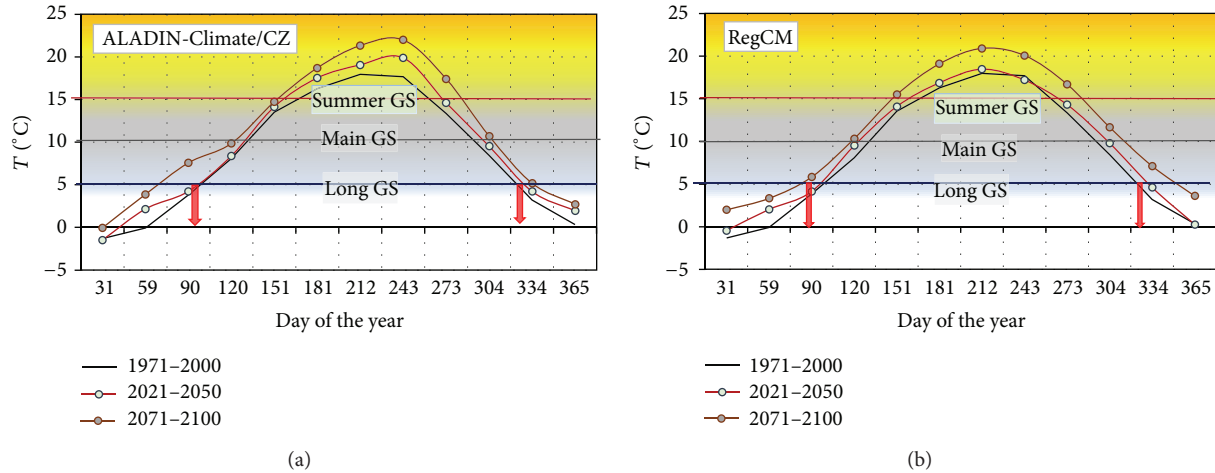


FIGURE 2: Daily temperatures for observed gridded dataset (1971–2000) and ALADIN-Climate/CZ and RegCM simulation values after bias correction for A1B scenario runs (2021–2050 and 2071–2100) for Elbe River lowland. Schematic delimitation of the long growing season ($T_{\text{mean}} \geq 5^\circ\text{C}$), the main growing season ($T_{\text{mean}} \geq 10^\circ\text{C}$), and the summer growing season ($T_{\text{mean}} \geq 15^\circ\text{C}$) is included.

individual percentiles whose relationships are derived from observations and a control RCMs simulation [28]. After the correction, the model outputs (for 2021–2050 and 2071–2100) were fully compatible with the gridded observation dataset (1971–2000). Figure 2 shows the annual variation of bias corrected daily temperature means calculated for 30 years, corresponding to the RegCM (forced by ECHAM5) and ALADIN-Climate/CZ (forced by ARPÉGE-Climate) in the A1B scenario runs (2021–2050 and 2071–2100), respectively. The results show that the projected temperature means for all months in the A1B scenario runs will increase compared to the current climate (1971–2000).

For the Czech Republic as a whole, ALADIN-Climate/CZ and RegCM simulated increases in temperature, especially in the summer and winter. Over the Elbe lowland region, the temperatures are projected to increase by the end of the 21st century compared to the mid-21st century and the reference period 1971–2000. The 30-year annual temperature means for the Elbe lowland are 8.4°C for the current climate (1971–2000) and 9.6°C for 2021–2050 and 11.4°C for 2071–2100. The mean summer temperature increases over all models are projected to be 1.7°C and 4.0°C in 2021–2050 and 2071–2100, respectively, relative to 1971–2000. The projected increases in the spring and autumn temperature means under the A1B scenario are 0.5°C and 2.3°C , respectively, in 2021–2050 and 1.1°C and 2.8°C , respectively, in 2071–2100. Overall, these projections suggest increase in the GSL in 2071–2100 relative to the present climate. Both RCMs simulations for the A1B SRES scenario reveal that the summer temperature, which has an important influence on the beginning and end of the $\text{GS} \geq 15^\circ\text{C}$ in hilly areas, will increase by the end of the 21st century. Increasing temperatures can lead to earlier harvests of thermophilic vegetables. However, responses to temperature changes may differ among vegetable varieties, mainly in terms of their temperature thresholds for optimum ripening [16].

2.3. Determination of BGS, EGS, and GSL. The effect of climate change on the GS of agricultural crops can be determined through phenological observations, the normalised difference vegetation index from satellite data, and surface air temperatures [7, 29–36]. Definitions of the growing season using surface air temperatures may be considered valid in areas where the GS is largely limited by temperature. In our study, we used threshold temperatures for a predefined number of days to start and end the climatological GS, which has good spatial coverage over the regular grid network. However, there is no universal definition of the climatological GS depending on the geographic position and associated climate regimes, and there may be large disagreement in GSL changes depending on the definition used [34]. The climatological GS can be defined as the entire period in which growth can theoretically take place [31]. In an attempt to provide a common benchmark for investigators, [32] selected the 5°C threshold to standardise the definition of the GS as the period when daily temperatures remain above 5°C for more than 5 days. Reference [31] defined the start of the GS as $>5^\circ\text{C}$ for ≥ 5 days and the end as a 10-day period of mean daily temperatures below 5°C . In the Greater Baltic Area, [34] defined the start of the growing season as the last day of the first six-day period with daily mean temperatures above 5°C after the last winter/spring frost. In our study, the GS parameters were defined with respect to the physiological requirements of the vegetable types and the classification system of the *Climate Atlas of Czechia* [37] (the large growing season ($T_{\text{mean}} \geq 5^\circ\text{C}$), the main growing season ($T_{\text{mean}} \geq 10^\circ\text{C}$), and the summer growing season ($T_{\text{mean}} \geq 15^\circ\text{C}$)).

The sowing/planting period differs among field vegetable types; therefore, we defined the BGS as the first five consecutive days during which the daily mean temperature equals or exceeds 5, 10, or 15°C and, subsequently, does not drop below T_{mean} 5, 10, or 15°C for five days or more. The EGS is defined as the first day of the first 5-day period with a T_{mean} below 5,

TABLE 1: Statistical characteristics of the area-averaged growing season parameters of the studied area for 1961–2011.

	$T_{\text{mean}} \geq 5^\circ\text{C}$			$T_{\text{mean}} \geq 10^\circ\text{C}$			$T_{\text{mean}} \geq 15^\circ\text{C}$		
	Start	End	Length	Start	End	Length	Start	End	Length
Median	26 Mar.	4 Nov.	223	21 Apr.	7 Oct.	169	21 May	7 Sep.	109
STDev	10.1	12.9	15.7	10.4	9.7	14.3	15.2	11.0	18.0
Earliest/shortest	4 Mar. (1990)	12 Oct. (1994)	188 (1997)	30 Mar. (1998)	16 Sep. (1972)	136 (1972)	21 Apr. (1962)	19 Aug. (1978)	67 (1965)
Latest/longest	16 Apr. (1997)	8 Dec. (2006)	256 (2006)	22 May (1980)	28 Oct. (2000)	195 (2000)	26 Jun. (1974)	30 Sep. (1966)	151 (2000)

10, or 15°C . The GSL is the number of days between the BGS and EGS for the three threshold temperatures. Using the three thresholds of daily T_{mean} is justified because they correspond to the vegetation period of the majority of field vegetables. BGS $\geq 5^\circ\text{C}$ represents the average date of the sowing period of the majority of field frost-resistant vegetables, whereas the start of BGS ≥ 10 and 15°C corresponds to the sowing/planting periods of field cold-resistant and thermophilic vegetables, respectively, in the studied region. The EGS corresponds to the harvest period of different types of vegetable crops. The GSL is the time from sowing to harvest or the time from planting to harvest.

Using these definitions, we produced time series of the start, end, and length of the growing season for 116 grid points for both the observations and the model datasets. Furthermore, we created and statistically processed two datasets. First, to characterise the spatial patterns of the GS parameters, the annual BGS, EGS, and GSL series for the three thresholds were averaged at each grid point for the current climate (1961–2011) and two future climates (2021–2050 and 2071–2100). Second, to examine temporal variations in the GS parameters over the Elbe River lowland as a whole, the BGS, EGS, and GSL for the three thresholds were arithmetically averaged over all 116 grid points to obtain a time series for the current climate (1961–2011) and the two future climates (2021–2050 and 2071–2100). Then, projected changes in the dates of the start and end and the length of the growing season are analyzed by comparing the model simulations for the periods 2021–2050 and 2071–2100 with the reference period 1971–2000.

To investigate changes in the timing of the observed GS parameters, regional anomalies in the start, end, and length of the growing season for the three thresholds over the Elbe River lowland from 1961 to 2011 were calculated. Positive anomalies indicate dates later in the year (fall and spring occurrences) or a greater number of days (length). We then classified anomalies in the growing season onset, end, and length into two categories: (1) years with advances and/or increases in the growing seasons and (2) years with delays and/or decreases in the growing seasons. We also calculated linear trends and analysed the regression slopes of the GS parameters and assessed their significance using Student's one-tailed t -test. Finally, to identify prospective areas for growing thermophilic vegetables, kriging interpolation tools in ArcGIS software were used to create maps of the spatial distributions of the GS parameters for the current and future

climate conditions. Interpolation, where needed, is based on local linear regression (dependence of given meteorological element on altitude) and universal kriging interpolation method. To generate the maps at regional scale we used CLIDATA GIS environment and CLIDATA DEM (digital elevation model) method with a horizontal resolution of 500 m and 40 km radius of regression.

3. Results and Discussion

3.1. Climatology of the Beginning, End, and Length of Growing Seasons

3.1.1. *The Long Growing Season: $T_{\text{mean}} \geq 5^\circ\text{C}$.* The analysis domain was averaged to evaluate interannual variations in the start, end, and length of the growing season for the three thresholds ($T_{\text{mean}} \geq 5, 10, \text{ and } 15^\circ\text{C}$) over the Elbe River lowland as a whole. The beginning of field sowing for the majority of frost-resistant vegetables corresponds to the transition of the average daily temperature through 5°C . The long-term average (1961–2011) starts and ends of the growing season for $T_{\text{mean}} \geq 5^\circ\text{C}$ range from March 26 to November 4, and the growing season lasts 223 days on median (Table 1). A shortening of the growing season by 35 days compared with the long-term average occurred in 1997 due to a delayed start of BGS $\geq 5^\circ\text{C}$ by 21 days. A lengthening of the growing season by 33 days compared with the long-term average occurred in 2006 due to a delayed EGS. The earliest beginning of the growing season was observed in 1990, with an onset of 22 days earlier than the regional average (4 March) (Tables 1 and 2). The onset of spring was very early in 1990 due to temperature anomalies from February to the second half of March that resulted in T_{mean} deviations from $+5.0$ to $+11.0^\circ\text{C}$. The GSL in 1990 also ranked among the four longest growing seasons between 1961 and 2011 (Table 2). In this year, the anomalies in the BGS in Central Europe (up to -27 days) were due to temperature anomalies of up to $+4.5^\circ\text{C}$ that occurred from February to April. These findings are similar to those reported by [7]. The earliest EGS $\geq 5^\circ\text{C}$ date was recorded in 1994 (October 12). In this year, the EGS was 23 days earlier, on average, throughout the Elbe lowland. A marked cooling associated with a low-pressure trough occurred in the first half of October. This low-pressure trough was associated with individual frontal systems that progressed from west to east across Europe and led to low-temperature anomalies. The latest EGS $\geq 5^\circ\text{C}$ occurred in 2006, approximately 34

TABLE 2: Area-averaged anomalies (sorted by the highest number of anomalies in days) in the start, end, and length of the growing season for the three thresholds of $T_{\text{mean}} \geq 5, 10, \text{ and } 15^\circ\text{C}$ over the Elbe River lowland for 1961–2011.

		Years	Anomalies (days)
Advance/increase of growing season			
BGS $\geq 5^\circ\text{C}$	Early start	1990, 1981, 1961, 1991, 2007, 2011	-22, -18, -17, -17, -14, -14
EGS $\geq 5^\circ\text{C}$	Late end	2006, 2000, 1963, 1969, 2008, 1987, 1996, 2010	+34, +28, +20, +18, +17, +16, +15, +12
GSL $\geq 5^\circ\text{C}$	Longer	2006, 2000, 1961, 1990, 2008, 2010, 2011	+33, +29, +23, +22, +22, +19, +18
Delay/decrease of growing season			
BGS $\geq 5^\circ\text{C}$	Late start	1997, 1970, 1962, 1975, 1996, 1969	+21, +18, +17, +15, +13, +12
EGS $\geq 5^\circ\text{C}$	Early end	1994, 2009, 1965, 1991, 1997	-23, -21, -18, -15, -15
GSL $\geq 5^\circ\text{C}$	Shorter	1997, 1962, 1975, 1965, 1973, 1979, 1980	-35, -30, -25, -23, -17, -17, -13
Advance/increase of growing season			
BGS $\geq 10^\circ\text{C}$	Early start	1998, 1974, 2009, 1981, 1961	-22, -20, -19, -17, -15, -8
EGS $\geq 10^\circ\text{C}$	Late end	2000, 2001, 1988, 1967, 1984, 1983, 1991	+21, +18, +13, +12, +12, +10, +10
GSL $\geq 10^\circ\text{C}$	Longer	2000, 2009, 1981, 1961, 1998	+26, +22, +19, +17, +15
Delay/decrease of growing season			
BGS $\geq 10^\circ\text{C}$	Late start	1980, 1982, 1965, 1970, 1972, 1984, 1987, 1997	+31, +22, +21, +13, +13, +11, +11, +10
EGS $\geq 10^\circ\text{C}$	Early end	1977, 1972, 1971, 1996, 1970	-22, -21, -16, -15, -14
GSL $\geq 10^\circ\text{C}$	Shorter	1972, 1980, 1970, 1977, 1987, 1965, 1971	-33, -31, -27, -26, -22, -21, -20
Advance/increase of growing season			
BGS $\geq 15^\circ\text{C}$	Early start	1962, 1993, 2000, 1968, 2001, 1986, 1998, 2003	-30, -28, -28, -22, -21, -20, -19, -16
EGS $\geq 15^\circ\text{C}$	Late end	1966, 1975, 1989, 2006, 1999, 2003, 2000	+23, +22, +18, +17, +17, +14, +13
GSL $\geq 15^\circ\text{C}$	Longer	2000, 1966, 1993, 2003	+41, +32, +31, +30
Delay/decrease of growing season			
BGS $\geq 15^\circ\text{C}$	Late start	1974, 1965, 1972, 1980, 1975	+36, +28, +24, +21, +20
EGS $\geq 15^\circ\text{C}$	Early end	1978, 1986, 1965, 1970, 1971	-19, -19, -14, -13, -12
GSL $\geq 15^\circ\text{C}$	Shorter	1965, 1974, 1980, 1978, 2010, 1972, 1970	-42, -30, -30, -26, -26, -23, -22

days later compared with the long-term mean, as a result of the strong positive T_{mean} anomalies that occurred from September to October. The year 2006 had also the longest GSL $\geq 5^\circ\text{C}$.

3.1.2. The Main Growing Season: $T_{\text{mean}} \geq 10^\circ\text{C}$. The beginning of active growth and development of the main field vegetables is considered to correspond to the stable transition of the average daily air temperature through 10°C . The mean dates of the start and end of the growing season throughout the Elbe lowland for $T_{\text{mean}} \geq 10^\circ\text{C}$ are April 21 and October 7, respectively, and the mean growing season length is 169 days (Table 1). The earliest date of BGS $\geq 10^\circ\text{C}$ was observed in 1998 (30 March), an advance of 22 days caused by strong positive temperature anomalies (up to $+6.0^\circ\text{C}$). The onset of spring was also very early this year throughout Central Europe [7]. The reverse was observed in 1980, with the latest date of BGS $\geq 10^\circ\text{C}$ observed (May 22, +31 days compared with the long-term average). Moreover, an early end of the growing season in the fall of 1980 resulted in extreme reductions in the GSL $\geq 5^\circ\text{C}$ (-13 days), GSL $\geq 10^\circ\text{C}$ (-31 days), and GSL $\geq 15^\circ\text{C}$ (-30 days) compared with the long-term average (Table 2). The length of the growing season significantly affects the vegetable sector. Its extension in the spring allows for early sowing/planting of crops, and its extension in the fall has a positive effect on the production quality, allowing a gradual harvest. The earliest date of EGS $\geq 10^\circ\text{C}$ occurred in 1972

(September 16), and the latest date occurred in 2000 (October 28). Consequently, the longest and shortest growing seasons occurred in 2000 (195 days) and 1972 (136 days), respectively.

3.1.3. The Summer Growing Season: $T_{\text{mean}} \geq 15^\circ\text{C}$. The period of $T_{\text{mean}} \geq 15^\circ\text{C}$ corresponds to the beginning of the transplanting of thermophilic vegetables. The mean dates of the start and end of the growing season for $T_{\text{mean}} \geq 15^\circ\text{C}$ are May 21 to September 7, and the mean length of the growing season is 109 days. The earliest date for BGS $\geq 15^\circ\text{C}$ occurred in 1962 (21 April), and the latest date occurred in 1974 (26 June). The earliest end of the growing season occurred in 1978 and 1986 (19 August), earlier than the average by -19 days (Tables 1 and 2). The latest end occurred in 1966 (30 September), later than the average by +23 days. The greatest lengthening of the growing season, +42 days compared with the long-term mean, occurred in 2000, and the greatest shortening of the growing season, -42 days compared with the long-term mean, occurred in the cool year of 1965. In 2000, strong positive temperature anomalies of 3.5°C to 5.0°C in the daily mean temperatures in April led to an advance in BGS $\geq 15^\circ\text{C}$ of 28 days. In the same year, a significantly longer growing season was recorded, not only in terms of GSL $\geq 15^\circ\text{C}$ but also in terms of GSL $\geq 5^\circ\text{C}$ (+22 d) and GSL $\geq 10^\circ\text{C}$ (+26 d). The growing season was extremely long that year throughout Europe [7, 29].

3.2. Temporal Variability of the Beginning, End, and Length of Climatological Growing Seasons

3.2.1. Anomalies in the Start, End, and Length of the Growing Season. Regional anomalies in the start, end, and length of the growing season for the three threshold temperatures in the Elbe River lowland for 1961–2011 are shown in Table 2. Growing seasons with stronger negative and positive anomalies were classified into two categories: (1) years with advances and/or increases in the growing season (i.e., an early start and/or late end) and (2) years with delays and/or decreases in the growing season (i.e., a later start and/or early end). During the second half of the 20th century and the first decade of the 21st century, the years with the largest anomalies in terms of an early start of the growing season ($BGS \geq 5^\circ\text{C}$) were 1990 (–22 d), 1981 (–18 d), 1961 (–17 d), 1991 (–17 d), 2007 (–14 d), and 2011 (–14 d). The years with the largest anomalies in terms of a later end of the growing season, $EGS \geq 5^\circ\text{C}$, were 2006 (+34 d), 2000 (+28 d), 1963 (+20 d), 1969 (+18 d), 2008 (+17 d), 1987 (+16 d), 1996 (+15 d), and 2010 (+12 d). Thus, an earlier start of $BGS \geq 5^\circ\text{C}$ and a later end of $EGS \geq 5^\circ\text{C}$, together with a late end of the growing season, occurred in 1961, 1990, and 2011 (Table 2). However, the years 2010 and 2011 had early fall frosts that occurred during the harvest period for root vegetables (e.g., *Apium graveolens*). The years with delayed and/or decreased $GS \geq 5^\circ\text{C}$ were 1997 (–35 d), 1962 (–30 d), 1975 (–25 d), 1965 (–23 d), 1973 (–17 d), and 1979 (–17 d). All these years also had a later end of spring and an early beginning of fall frosts [9].

Based on the same selection criteria, the years with advanced and/or increased $GS \geq 10^\circ\text{C}$ were 2000 (+26 d), 2009 (+22 d), 1981 (+19 d), 1961 (+17 d), and 1998 (+15 d). The years with delayed and/or decreased $GS \geq 10^\circ\text{C}$ were 1972 (–33 d), 1980 (–31 d), 1970 (–27 d), 1977 (–26 d), 1987 (–22 d), 1965 (–21), and 1971 (–20 d). The majority of these years appear to be associated with temperature anomalies in Central Europe [7, 8, 29]. Our results are in line with these findings and offer additional insights into the complexity of these phenomena on a regional scale. Although the growing seasons have ended later, the BGS has made a greater contribution to the increase in GSL (1961, 1981, 1998, and 2009) (Table 2). A later start, early end, and shorter GSL occurred in 1970 and 1972. A shortening of the growing season occurred in 1971 and is attributed to an early end of $EGS \geq 10^\circ\text{C}$, whereas the shortening of the GS that occurred in 1965 and 1987 is attributed to a later onset of the growing season in those years.

The variability in strong anomalies in the start, end, and length of the growing season for $T_{\text{mean}} \geq 15^\circ\text{C}$ is similar to that for $GS \geq 5$ and 10°C (Table 2). Positive anomalies for $GSL \geq 15^\circ\text{C}$ were recorded in 2000 (+41 d), 1966 (+32 d), 1993 (+31 d), and 2003 (+30 d), while negative anomalies were recorded in 1965 (–42 d), 1974 (–30 d), 1980 (–30 d), 1978 (–26 d), 2010 (–26 d), 1972 (–23 d), and 1970 (–22 d). For field thermophilic vegetables, a shift in the beginning date of the growing season in the spring months is more advantageous than a change in the growing season length. An early start of $BGS \geq 15^\circ\text{C}$, together with a longer $GSL \geq 15^\circ\text{C}$, was recorded in 1993 (an average advance of –28 d and

a lengthening of +31 d), 2000 (–28 d and +41 d), and 2003 (–16 d and +30 d), which led to advanced dates of planting of field thermophilic vegetables in the studied region. These growing seasons appear to be associated with high positive temperature anomalies and high deficits in the water balance (i.e., exceptionally warm and dry spells) throughout the country. The year with the latest start of $BGS \geq 15^\circ\text{C}$, the earliest end of $EGS \geq 15^\circ\text{C}$, and the shortest GSL was 1965. This year has also been identified in previous study of the Czech Republic [14] as having been extremely wet and cold. Late-onset and shortened growing seasons also occurred in 1972, 1974, and 1980, while an early end and shorter $GSL \geq 15^\circ\text{C}$ occurred in 1970, 1971, and 1978.

We observed that the majority of years with delays and/or decreases in the growing seasons occurred in the cool and wet decade of 1971 to 1980, which was characterised with persistently higher than normal precipitation and the lowest negative deviations in daily mean temperatures since 1961. During this decade, the regional average of the ending of mild spring frosts occurred in the second half of May, and the years had shorter frost-free periods [9].

Figure 3 displays the interannual variations of the area-averaged BGS, EGS, and GSL for average daily temperatures of at least 5°C , 10°C , and 15°C in the Elbe River lowland during the period 1961–2011. As the left panel of Figure 3 shows, the BGS exhibited high interannual variation. Positive anomalies predominated during 1963–1973 for $BGS \geq 5$ and 10°C and during 1970–1980 for $BGS \geq 15^\circ\text{C}$, whereas negative anomalies predominated during 1989–1997 and 2000–2011. Although the annual $BGS \geq 15^\circ\text{C}$ significantly advanced during the 1990s, the signal was reduced in the 2000s. Overall, the long-term variations in BGS exhibited earlier spring features, which are consistent with the findings of other climatological research [3, 34, 36]. Moreover, the majority of phenological studies show similar trends: earlier springs and longer periods of plant growth due to greater changes in the timing of the BGS rather than in the timing of the EGS [3, 34, 36]. The annual changes in EGS also exhibit strong interannual variations (middle panel of Figure 3). In contrast to $BGS \geq 5$ and 10°C , negative anomalies were observed during 1970–1980, whereas positive anomalies were observed during the 1990s and 2000s, which indicates a delayed EGS in recent decades. Asymmetric long-term variations in BGS and EGS led to increases in the total GSL (right panel of Figure 3). With the weakening of the earlier BGS trends, greater delays in EGS clearly led to longer GSL s from 1995 through the 2000s. Conversely, in the first decade of the 21st century, the $GSL \geq 15^\circ\text{C}$ slightly shortened as a result of the delayed start of the growing season; however, the end of $EGS \geq 15^\circ\text{C}$ occurred later, which may have had a positive effect on the ripening and quality of thermophilic vegetables. A later onset of $GSL \geq 15^\circ\text{C}$ can be mitigated by agrotechnical measures. Using remote measurements of the vegetation index and daily mean temperatures, [35] found that the lengthening of the GS in Europe in the last decade could be attributed mainly to the delay in EGS rather than to the advance of BGS. Moreover, the temporal evolution of GS in different climatic regimes is characterised by large spatial differences. Climatic indicators (e.g., the frost-free period and the thermal growing season),

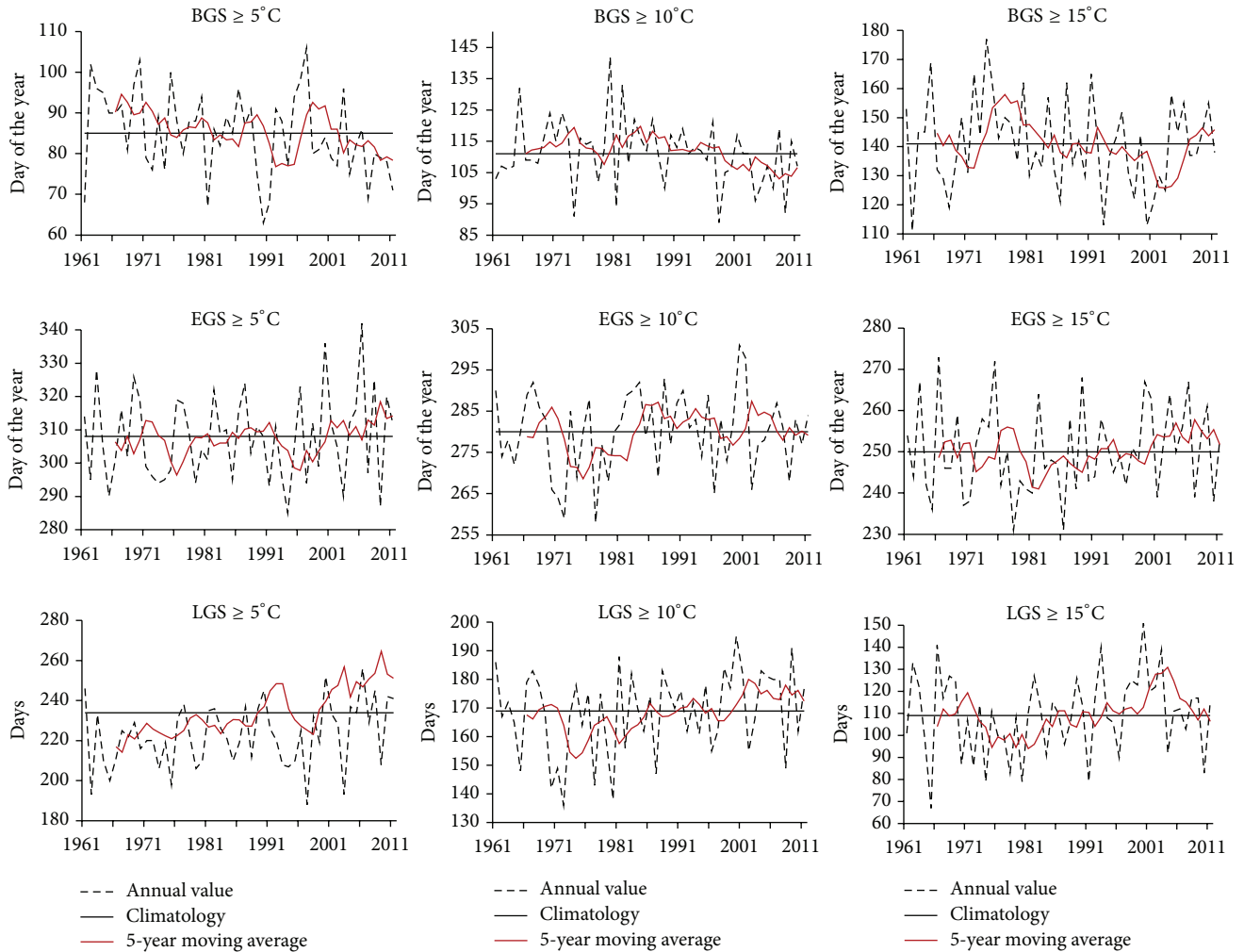


FIGURE 3: Interannual variations of area-averaged BGS (beginning of the growing season), EGS (end of the growing season), and LGS (length of the growing season) for the 5, 10, and 15°C temperature thresholds from 1961 to 2011 in the Elbe River lowland. The black line indicates the climatology of each event (average), and the grey line indicates the 5-year moving average of each parameter.

remote sensing-based indicators, and phenological studies all indicate shifts in the timing and length of the growing season [3, 5, 7, 8, 10, 31, 32, 34, 36].

3.2.2. Trends of the Growing Season. To obtain additional insights into the changes in the timing of the GS parameters in the area-averaged time series, the linear trends and regression slopes of the growing season onset, end, and length were calculated. The significance of these trends was tested using Student's one-tailed t -test at the 95% significance level. The linear trends of the beginning, end, and length of the growing season are tabulated in Table 3. Increasingly negative BGS trends and positive EGS trends led to increasing GSL trends. Over a 51-year period, the $GS \geq 5^\circ C$ started 10.7 days earlier and ended 4.6 days later, yielding an increase in the GSL of 15.3 days. The $BGS \geq 10^\circ C$ advanced by 7.6 days on average, and the $EGS \geq 10^\circ C$ was delayed by 3.6 days on average, resulting in an average lengthening of the $GSL \geq 10^\circ C$ by 11.2 days. The $GSL \geq 15^\circ C$ advanced by only 5.1 days, with smaller changes during the spring (1.0 day) than in the fall (4.1 days).

To understand the evolution of significant changes in the growing season series, the analysis period was divided into five decades (Table 3). The results suggest that the Elbe lowland has experienced the following changes in its growing season parameters over the last five decades. (1) Although advances in the BGS have been reported as the main factor in longer growing seasons, in this study, delays in the EGS were found to be a more important factor regulating GSL changes during the 1990s and 2000s at thresholds of $T_{\text{mean}} \geq 15^\circ C$. (2) We found that the $GSL \geq 5$ and $10^\circ C$ increased considerably during 1991–2000 ($>0.77 \text{ days yr}^{-1}$), but the lengthening was less pronounced during 1961–1970 and 1971–1980. (3) The largest changes in the start of $BGS \geq 5$ and $10^\circ C$ (earlier growing season starts of approximately one week) in the 2000s occurred because of warmer temperatures and earlier ends of the last frosts. (4) General trends towards later growing season ends were observed, except for 1961–1970, for which shifts of -0.7 and $-6.3 \text{ days decade}^{-1}$ towards an earlier growing season end were observed. (5) In the Elbe River lowland, BGS and EGS exhibited shifts towards earlier

TABLE 3: Observed long-term changes (days per year) in growing season parameters over the Elbe River lowland.

	$T_{\text{mean}} \geq 5^{\circ}\text{C}$			$T_{\text{mean}} \geq 10^{\circ}\text{C}$			$T_{\text{mean}} \geq 15^{\circ}\text{C}$		
	Start	End	Length	Start	End	Length	Start	End	Length
1961–1970	+0.91	−0.07	−0.98*	+0.95	−0.27	−1.22**	+0.49	−0.63	−1.12*
1971–1980	+0.80	+0.19	−0.61*	+0.90	+0.01	−0.89*	−0.06	−0.33	−0.27*
1981–1990	−0.38	+0.11	+0.49**	−0.41	+0.40	+0.81*	−0.09	+0.30	+0.39*
1991–2000	−0.76	+0.01	+0.77*	−0.82	+0.05	+0.87*	−0.10	+0.36	+0.46*
2001–2010	−0.54	+0.67	+1.21**	−0.56	+0.06	+0.62*	−0.01	+0.56	+0.57*
1961–2011	−0.21	+0.09	+0.30***	−0.15	+0.07	+0.22***	−0.02	+0.08	0.10**

*Marginally significant ($0.01 < P \leq 0.05$); **significant ($0.001 < P \leq 0.01$); ***highly significant ($P \leq 0.001$).

and later dates, respectively. However, from 1981 to 2000, the earlier BGS ≥ 5 and 10°C was more dominant than the delayed EGS ≥ 5 and 10°C , whereas from 2001 to 2010, for the growing season defined in terms of $T_{\text{mean}} \geq 15^{\circ}\text{C}$, the later EGS (5.6 days decade^{−1}) was more significant than the earlier BGS (0.1 days decade^{−1}). Similar results at the European level were reported by [35], with the delay in EGS by 8.2 days being more significant than the advance in BGS by 3.2 days during 2000–2008.

3.3. Observed Spatial Variability of Start, End, and Length of Growing Seasons. The GS parameters exhibited clear spatial variability. For clarity of presentation, the locations of specific fields and the Elbe River across the lowlands were added to the maps. Over the past 51 years, the GS $\geq 5^{\circ}\text{C}$ started between March 11 and 26, and a start before March 11 was calculated for the northeastern Prague plateau (Figure 4). Overall, this is a spatial difference of 15 days. Thus, the BGS $\geq 5^{\circ}\text{C}$ started 4 days later per 100 m of altitude. The map of BGS $\geq 5^{\circ}\text{C}$ defines two main areas with a start of the growing season before March 21. These areas can be considered climatically close to the optimum for field vegetable production. However, the occurrence of severe frosts ($T_{\text{min}} \leq -2.2^{\circ}\text{C}$) during the planting of field frost-resistant vegetables in the growing area of the Elbe lowland is, on average, 56.9% [9]. It follows that, despite the considerable resistance of these vegetables to low temperatures, it is necessary to choose planting areas with southern exposures (or cover plants with nonwoven textiles). Utilising resistant varieties and hardening seedlings before planting are advisable. Over the studied region, the GS $\geq 10^{\circ}\text{C}$ starts nearly 4 weeks after BGS $\geq 5^{\circ}\text{C}$. Geostatistical analysis indicates that the BGS $\geq 10^{\circ}\text{C}$ starts roughly 2 days later for every 100 m of elevation. Consequently, the BGS $\geq 10^{\circ}\text{C}$ starts between April 15 and 30, and a start before April 15 can be observed in the traditional vegetable-growing regions (up to 300 m). In the warmest areas of the middle Elbe lowland, the middle Poohří, and the northeast of the Prague platform, the mean date of the BGS $\geq 10^{\circ}\text{C}$ occurs between April 16 and 20. Conversely, in the hilly lands of the northern and eastern parts of the Elbe River lowland, the start of BGS $\geq 10^{\circ}\text{C}$ occurs in the end of April. In addition, most vegetables grown in the warmest areas fall within the low-risk category for severe spring frosts. It will therefore be possible to extend the areas suitable for growing cold-resistant vegetables (i.e., mostly Brassicas) towards the northeast of the middle Elbe lowland.

The BGS $\geq 15^{\circ}\text{C}$ starts between May 8 and 18, approximately 1.8 days later per 100 m of altitude. The latest beginning dates of BGS $\geq 15^{\circ}\text{C}$ after May 15 are related to high altitudes in the region (higher than 300 m) and frost hollows, whereas the earliest starts before May 8 are observed in the lower areas (lower than 250 m). The risk of frost after May 15 in the traditional vegetable-growing regions (up to 250 m) is low. At higher altitudes, areas with zero incidences of negative minimum temperatures were found, which may allow for the possible expansion of the area of thermophilic vegetable cultivation [9].

Over the Elbe River lowland, compared with the start of the growing season, the end of the growing season pattern follows the altitudinal gradient to a lesser degree. There are no large differences in the spatial distribution of the growing season end between $T_{\text{mean}} \geq 5, 10,$ and 15°C (middle panel of Figure 4). The EGS $\geq 5^{\circ}\text{C}$ dates range from 298 days (October 25) to 314 days (November 10), and their spatial distributions are inversely related to the climatology of the BGS dates. In 15% of the study area (hilly lands and frost hollows), the earliest end of the EGS $\geq 5, 10,$ and 15°C occurs before October 31, October 5, and September 5, respectively. The latest ending of EGS $\geq 5, 10,$ and 15°C (after November 6, October 11, and September 11) occurs in the northeastern Prague plateau and the middle Elbe River valley, which together cover 20% of the study area. The later end of the growing season in those regions is consistent with an observed earlier start of the growing season in the same region.

The pattern in GSL is consistent with the pattern in the onset of the growing season; GSL pattern also shows some local differences due to the heterogeneous end of the growing season pattern, especially for $T_{\text{mean}} \geq 15^{\circ}\text{C}$ (right panel of Figure 4). A total of 50% of the area of the Elbe River lowland has a GSL $\geq 5^{\circ}\text{C}$ longer than 225, which satisfies the requirements of *root* vegetables (celeriac), which have the longest growing seasons. The GSL $\geq 10^{\circ}\text{C}$ is between 150 and 180 days. 65% of the area has a growing season shorter than 170 days.

4. Projected Changes in the Dates of the Start and End and the Length of the Growing Season

An assessment was made of the potential changes in the dates of the BGS, EGS, and GSL for the three threshold

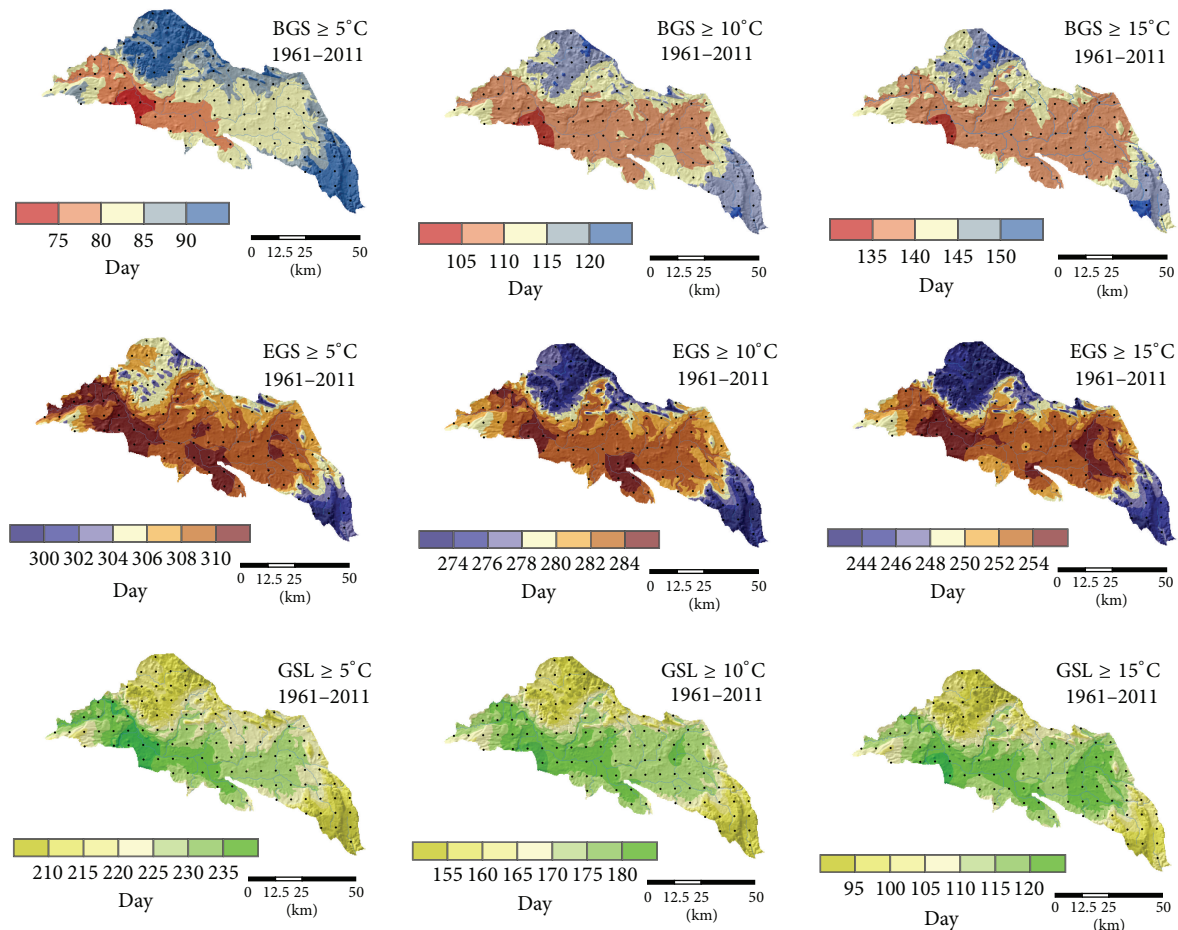


FIGURE 4: Spatial variability of the mean values of BGS, EGS, and GSL for the 5, 10, and 15°C temperature thresholds from 1961 to 2011 in the Elbe River lowland.

temperatures over the Elbe River lowland, simulated using the RCMs under the A1B SRES scenario (2021–2050 and 2071–2100). Hovmoller-type diagram displays (Figure 5) the spatiotemporal evolution of large growing season, the main growing season, and the summer growing season projected from 116 grid points over the Elbe River lowland based on ALADIN-Climate/CZ and RegCM simulations data under the A1B SRES scenario runs (2021–2050 and 2071–2100). The use of the RCMs made it possible to estimate potential changes in the GS parameters and identify prospective areas for growing thermophilic vegetables in the Elbe River basin. It is worth noting that, in addition to the types of vegetables traditionally grown in the Elbe River valley, extension of the cultivation of thermophilic varieties, especially *Cucumis melo* L., has already been observed [9]. This extension is closely linked to warming of the climate system. Consequently, the cultivation of thermophilic vegetables will complement the cultivation of traditional assortment of vegetables. Thus, a detailed evaluation of the past long-term changes in the GS parameters is essential for predicting the effect of future climate variability on the range of vegetables that can be cultivated in this region.

4.1. Temporal Variability of the Projection of BGS, EGS, and GSL. The projected dates of the start, end, and length of the growing season across the Elbe lowland as a whole for the three threshold temperatures and the two future periods considered (2021–2050 and 2071–2100) are presented in Table 4. For both RCMs the dominant dates of BGS ≥ 5 , 10 and 15°C are projected to advance significantly (i.e., occur earlier) than under the current climate conditions. According to ALADIN-Climate/CZ, in the mid-21st century period, the medians BGS ≥ 5 , 10, and 15°C are projected to advance to days 81 (22 Mar), 107 (17 Apr), and 141 (21 May), respectively. At the end of the 21st century, the medians are projected to advance significantly, to days 59 (28 Feb), 81 (22 Mar), and 133 (13 May), respectively. A similar pattern was shown by RegCM (Table 4). These shifts reflect the higher projected temperatures in the A1B scenario. The earliest and latest starts of BGS ≥ 5 , 10, and 15°C for the period 2021–2050 are projected to occur on days 51 (20 Feb.), 80 (21 Mar.), and 120 (30 Apr.), respectively, and on days 107 (17 Apr.), 123 (3 May), and 166 (15 Jun.), respectively. The earliest onset of BGS ≥ 5 is projected to shift significantly towards the winter season by the end of the 21st century (2071–2100).

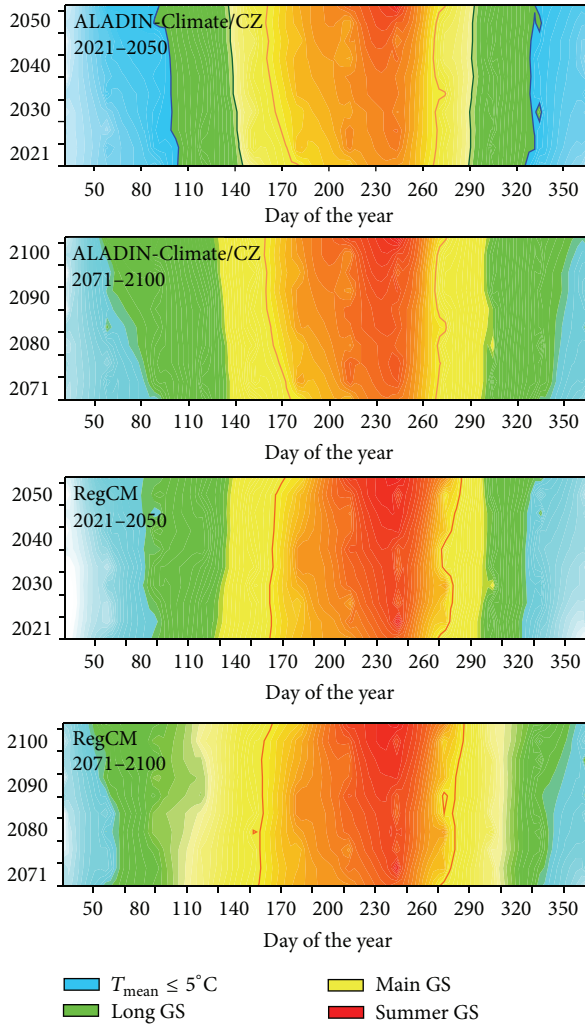


FIGURE 5: Hovmoller-type diagram of the spatiotemporal evolution of large growing season ($T_{\text{mean}} \geq 5^\circ\text{C}$), the main growing season ($T_{\text{mean}} \geq 10^\circ\text{C}$), and the summer growing season ($T_{\text{mean}} \geq 15^\circ\text{C}$) projected from 116 grid points \times 30 years \times 365 days over the Elbe River lowland based on ALADIN-Climate/CZ and RegCM simulation data under the A1B SRES scenario runs (2021–2050 and 2071–2100).

In general for both RCMs, the end of the growing season is projected to be significantly delayed (i.e., occur later) under the climate change scenario compared with the current climate. The medians of the EGS $\geq 5, 10,$ and 15°C by ALADIN-Climate/CZ are projected to occur on days 315 (11 Nov.), 284 (11 Oct.), and 255 (12 Sep.), respectively, during 2021–2050. The delay will be greatest during the period 2071–2100, when the mean dates of EGS $\geq 5, 10,$ and 15°C are projected to occur on days 318 (14 Nov.), 293 (20 Oct.), and 267 (24 Sep.), respectively. The latest dates of the end of EGS $\geq 5, 10,$ and 15°C for the period 2021–2050 are projected to occur on days 345 (11 Dec.), 302 (29 Oct.), and 273 (30 Sep.), respectively. The later end of the growing season will extend the vegetation period of field vegetables. The ALADIN-Climate/CZ and RegCM simulations project an increase in

the average growing season length; however, high interannual variability is projected, as in the current climate (Table 4). Under the A1B scenario for the period 2021–2050, the shortest and longest GSL $\geq 5^\circ\text{C}$ (GSL ≥ 10 and 15°C) vary between 182 (154 and 86 days) and 272 (207 and 140 days) days. Our regional projections for the end of the 21st century indicate that GSL $\geq 5^\circ\text{C}$ (GSL ≥ 10 and 15°C) could be significantly extended by an average of 267 days (212 and 134 days).

Table 5 displays the predicted changes in the mean start, end, and length of the GS between the reference period (1971–2000) and the two future climate periods (2021–2050 and 2071–2100) for the Elbe lowland. As expected, the magnitudes of the changes for the two future periods are different. The projections based on two different RCMs by A1B scenario suggest that, during the mid-21st century, the dates of the BGS $\geq 5, 10,$ and 15°C will be earlier (by ≥ 5 days) and those of the EGS $\geq 5, 10,$ and 15°C will be later (by ≥ 5 days) across the studied region. Consequently, the GSL $\geq 5^\circ\text{C}$ (GSL ≥ 10 and 15°C) will be increased under the A1B scenario by ≥ 11 days (≥ 13 and ≥ 11 days) compared with the current climate.

The advance of BGS $\geq 5, 10,$ and 15°C will be greater at the end of the 21st century (by ≥ 15 days). The ALADIN-Climate/CZ simulation for the period 2070–2100 projects delays in the EGS $\geq 5, 10,$ and 15°C by 12, 13, and 14 days, respectively, whilst RegCM simulation for the period 2070–2100 also projects delays in the EGS $\geq 5, 10,$ and 15°C by 12, 18, and 19 days, respectively. The ALADIN-Climate/CZ simulation for the BGS $\geq 5^\circ\text{C}$ start will be advanced by 22 days, and the EGS $\geq 5^\circ\text{C}$ end will be delayed by 12 days for the period 2071–2100. Therefore, the A1B scenario results in a projected lengthening of the GSL by 44 days on average compared with the current climate.

4.2. Spatial Distribution of BGS, EGS, and GSL Projections.

For the Czech Republic as a whole, the daily mean, maximum, and minimum temperatures simulated by ALADIN-Climate/CZ and RegCM for the A1B scenario are projected to increase more in Bohemia than in Moravia and at higher altitudes [27]. These temperature changes affect the growing season parameters, and thus, ALADIN-Climate/CZ and RegCM project greater changes in those parameters for the hilly lands of the Elbe River lowland. According to the ALADIN-Climate/CZ simulation for the period 2021–2050, at higher elevations in the Elbe lowland the GSL will correspond to that of the warmest areas in the current climate (Figures 6(a) and 6(b)). The lengthening of the growing season is most apparent for GSL ≥ 5 and 10°C . At the end of the 21st century, the GSL in the hottest areas will be significantly lengthened. Additionally, the areas with suitable conditions for growing vegetables (i.e., significant advance and delay of GS) will shift from the lowlands of the Elbe River valley to higher elevations (Figures 6(a) and 6(b)). However, profitable cultivation of vegetables in these areas is complicated by the complex sloping terrain. Therefore, the shift of areas with longer GSL from lowlands to higher elevations could lead to higher potential agroclimatic productivity, which will, however, be difficult to utilise due to the lack of water resources for irrigation and the inaccessibility of these areas to machinery.

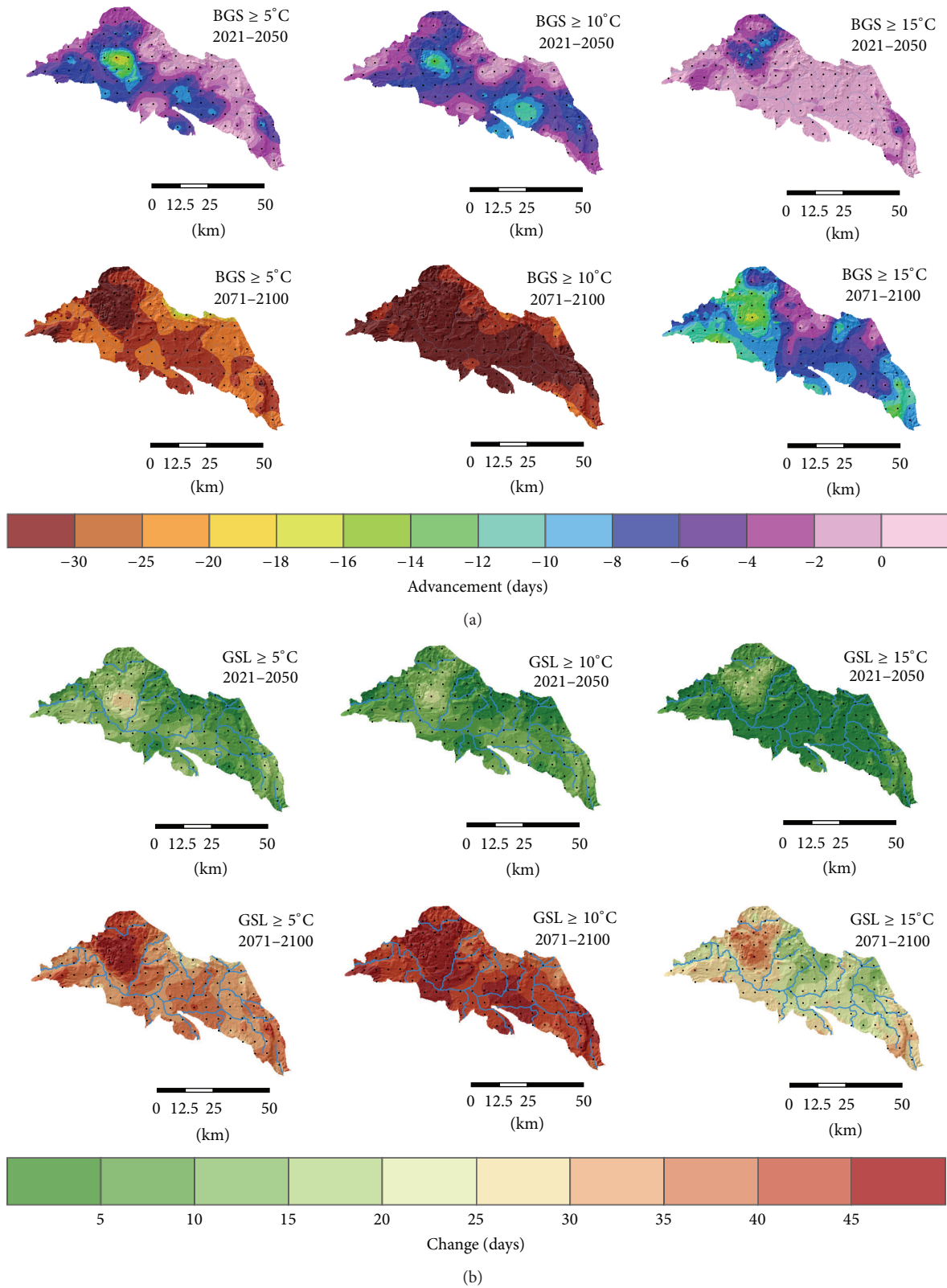


FIGURE 6: Spatial distribution of projected changes in BGS (a) and GSL (b) for the three threshold temperatures based on ALADIN-Climat/CZ simulation data under the AIB SRES scenario for two future periods, 2021–2050 and 2071–2100, over the Elbe River lowland.

TABLE 4: Projected dates of the start, end, and length of the regional growing season for two future periods (2021–2050 and 2071–2100) based on two different RCMs by A1B scenario run over the Elbe River lowland.

	$T_{\text{mean}} \geq 5^{\circ}\text{C}$			$T_{\text{mean}} \geq 10^{\circ}\text{C}$			$T_{\text{mean}} \geq 15^{\circ}\text{C}$		
	Start	End	Length	Start	End	Length	Start	End	Length
2021–2050 by ALADIN-Climate/CZ (RegCM)									
Median	81 (82)	315 (316)	234 (234)	107 (100)	284 (290)	178 (190)	141 (135)	255 (259)	114 (124)
Earliest/shortest	51 (56)	289 (289)	182 (178)	80 (81)	268 (263)	154 (165)	120 (88)	242 (233)	86 (91)
Latest/longest	107 (132)	345 (348)	272 (257)	123 (128)	302 (323)	207 (243)	166 (170)	273 (290)	140 (171)
2071–2100 by ALADIN-Climate/CZ (RegCM)									
Median	59 (60)	318 (320)	267 (260)	81 (80)	293 (298)	212 (212)	133 (128)	267 (269)	134 (141)
Earliest/shortest	28 (73)	301 (297)	225 (198)	39 (69)	281 (262)	175 (157)	84 (95)	247 (242)	93 (107)
Latest/longest	85 (116)	344 (350)	310 (259)	110 (128)	310 (322)	262 (243)	170 (153)	285 (311)	187 (185)

TABLE 5: Projected changes in the dates of the start, end, and length of the area-averaged growing season for two future periods (2021–2050 and 2071–2100) over the Elbe River lowland.

	$T_{\text{mean}} \geq 5^{\circ}\text{C}$			$T_{\text{mean}} \geq 10^{\circ}\text{C}$			$T_{\text{mean}} \geq 15^{\circ}\text{C}$		
	Start	End	Length	Start	End	Length	Start	End	Length
ALADIN-Climate/CZ by A1B scenario run									
2021–2050	Advance 10	Delay 6	Increase 16	Advance 7	Delay 6	Increase 13	Advance 6	Delay 5	Increase 11
2071–2100	Advance 22	Delay 12	Increase 44	Advance 32	Delay 13	Increase 45	Advance 15	Delay 14	Increase 29
RegCM by A1B scenario run									
2021–2050	Advance 5	Delay 7	Increase 11	Advance 11	Delay 10	Increase 21	Advance 6	Delay 9	Increase 15
2071–2100	Advance 27	Delay 12	Increase 37	Advance 31	Delay 18	Increase 49	Advance 13	Delay 19	Increase 32

Significant changes in the BGS can be expected mostly in hilly areas (Figures 6(a) and 6(b)). At the end of the 21st century, two main areas with different early growing season onsets will stand out: the area with the earliest onset of BGS, which will be located in the northwestern Elbe River lowland (i.e., in areas of frost hollows and hills), and a newly created region, which corresponds to currently peripheral areas of vegetable farmland (eastern part of Elbe River valley). The ALADIN-Climate/CZ and RegCM simulations reveal that, by the end of this century, Czech farmers could be growing their crops for up to two months longer. The Elbe River lowland can become a major producer of vegetables in the Czech Republic and significantly increase its competitiveness in the production of market vegetables.

Our results show that, under the A1B scenario for the two future climate periods considered (2021–2050 and 2071–2100), the projected increases in the growing season are due to significant projected advances of the starts of BGS ≥ 5 , 10, and 15°C . The BGS simulation data also show clear

tendencies towards an earlier start, especially for $\text{GSL} \geq 5$ and 10°C . The end of the growing season is projected to occur later on average, but these projected shifts are smaller than those for the beginning of the growing season. Based on these results, it is evident that regional climate change—specifically, increases in temperatures during the growing season—will affect Czech vegetable crops. The changes in the Elbe lowland climate are expected to significantly advance the sowing/planting dates of vegetables under current and future climate conditions. Similar findings have been reported for agricultural areas worldwide [4, 6, 11, 12, 30, 33, 35, 36, 38].

5. Summary and Concluding Remarks

In this study, a comprehensive analysis of the current climatic conditions (1961–2011) and possible changes in the climate in the near future (2021–2050) and at the end of the century (2071–2100) was undertaken using both observed gridded data and two RCMs driven by two different GCMs of the

changes in the timing of GS parameters for the Elbe River lowland for the first time. The ALADIN-Climate/CZ and RegCM models, with a high horizontal resolution of 10 km, provided the daily step temperature series to project changes in the GS parameters. The date of sowing/planting and the harvest period depend on the vegetable variety, agroclimatic conditions, commercial targets, market constraints, and horticultural practices. This is the probable reason for the absence of data on the sowing/planting and harvest dates of vegetables in the Czech Republic and in other countries. Systematically recorded information on phenology is utterly lacking for most types of vegetables at both the local and the global scales [16].

This research aimed to identify an approach to select suitable sites for extension of new thermophilic assortment of vegetables in Elbe lowland, taking into account regional specificity of climate change, and also to determine prospective areas for growing thermophilic vegetables in the study region using regional climate models. Proposed study can be crucial in development of strategies on climate change adaptation for different varieties of thermophile crops for future climate change in different regions in order to increase productivity while reducing both the cost of farmers and the water footprint of agriculture per unit product. Moreover, our study is in line with the two aims defined in the EU strategy for adaptation of agricultural production system through scientific research and other actions to advance sustainable agriculture development that benefits local, regional, and European farmers and to develop climate-informed crop. The results can be also relevant to the European policy, especially to the Common Agricultural Policy by contributing to good agricultural practices and sustaining the rural communities. The high degree of uncertainty in expected temperature and precipitation changes implies investment risks for deciding on long-term changes in farming technology such as adopting irrigation or switching to new crops, requiring new machinery, infrastructure, and agronomic and market knowledge [39]. The salient results are summarised below.

- (i) The temporal evolution of anomalies in the GS onset, end, and length displays two distinct periods: a delay in the onset in spring and a shortening of the GSL in the 1960s and an intensified lengthening of the GSL since the 1990s. The majority of years with strong delays in the onset and/or decrease in the length of the growing season occurred in the decade of 1971–1980, which was cooler and wetter than the other decades of the reference period analysed. In the last two decades of the period (1991–2011), BGS and EGS exhibited significant shifts to earlier and later dates, respectively. Consequently, the end of the 20th century and the beginning of the 21st century will be a suitable period for the extension of the cultivation of varieties of vegetables with longer growing seasons and higher temperature requirements.
- (ii) From 1961 to 2011, the Elbe River lowland experienced increasingly negative BGS and positive EGS trends that led to an increasing GSL trend. However, the roles of the changes in BGS and EGS differed depending on the time period and on the chosen temperature thresholds. The regional $GS \geq 5^{\circ}\text{C}$ (≥ 10 and 15°C) started 10.7 days (7.6 d and 3.1 d) earlier and ended 4.6 days (3.6 d and 4.1 d) later, yielding an increase in GSL of 15.3 days (11.2 d and 7.2 d) from 1961 to 2011. The delay in EGS was found to be a more important factor than the advance in BGS in regulating the GSL changes during the 1990s and 2000s at the threshold of $T_{\text{mean}} \geq 15^{\circ}\text{C}$.
- (iii) Under projected future climate conditions and temperature thresholds, the dominant dates of BGS and EGS for the entire study region are projected to be significantly advanced and delayed, respectively, compared with the current climate. A climate warming scenario suggests lengthening of the GSL in the coldest areas of the study region to the level of the warmest areas in the current climate. According to the RCMs simulation, the most significant shifts in the dates of the beginning and end of the GS are projected to occur in hilly areas; in lowland areas, these changes are not projected to be as pronounced. The lengthening of the GSL and the flat topography plateaus will create favourable conditions for the expansion of vegetables areas, mainly towards the eastern part of the Elbe River basin. The results also suggest potential for a northerly expansion of vegetables cultivation, although most of the lands to the north of the current frontier will remain only marginally suitable for growing field vegetables due to their complex terrain.

This study can be considered an initial step towards assessing the potential impacts of climate change on the types of vegetable crops grown in the Elbe River lowland. In our future work, we plan to use mechanistic crop simulation models (e.g., CROPGRO-Tomato model) and multimodel multisenario ensemble (for the new emission scenarios RCP4.5 and RCP8.5) to project potential consequences of climate change on fresh-market tomato (*Solanum lycopersicum* L.) grown under open field conditions at farm scale in the Elbe lowland.

Conflict of Interests

The authors declare that there is no conflict of interests regarding the publication of this paper.

Acknowledgments

This research was supported by Institutional Support Program for Long Term Conceptual Development of Research Institution provided by Ministry of Education, Youth and Sports of the Czech Republic and InterDrought CZ.1.07/2.3.00/20.0248. This study was also funded by the project Global and Regional Climate Model Simulations in Central Europe in the 18th–20th Centuries in Comparison with Observed and Reconstructed Climate, no. GAP209/11/0956. The authors are grateful to the associate editor (Macros Heil Costa) and two anonymous reviewers for their constructive comments and suggestions.

References

- [1] IPCC, *Working Group I Contribution to the IPCC Fifth Assessment Report Climate Change 2013: The Physical Science Basis*, 2013.
- [2] J. Alcamo, J. M. Moreno, B. Nováky et al., in *Climate Change 2007: Impacts, Adaptation and Vulnerability*, M. L. Parry, O. F. Canziani, J. P. Palutikof, P. J. van der Linden, and C. E. Hanson, Eds., Contribution of Working Group II to the Fourth Assessment Report of the Intergovernmental Panel on Climate Change, pp. 541–580, Cambridge University Press, Cambridge, UK, 2007.
- [3] C. Rosenzweig, G. Casassa, D. J. Karoly et al., “Assessment of observed changes and responses in natural and managed systems,” in *Climate Change 2007: Impacts, Adaptation and Vulnerability. Contribution of Working Group II to the Fourth Assessment Report of the Intergovernmental Panel on Climate Change*, M. L. Parry, O. F. Canziani, J. P. Palutikof, P. J. van der Linden, and C. E. Hanson, Eds., pp. 79–131, Cambridge University Press, Cambridge, UK, 2007.
- [4] M. Bindi and J. E. Olesen, “The responses of agriculture in Europe to climate change,” *Regional Environmental Change*, vol. 11, no. 1, pp. 151–158, 2011.
- [5] A. Menzel, J. von Vopelius, N. Estrella, C. Schleip, and V. Dose, “Farmers’ annual activities are not tracking speed of climate change,” *Climate Research*, vol. 32, no. 3, pp. 201–207, 2006.
- [6] F. N. Tubiello, M. Donatelli, C. Rosenzweig, and C. O. Stockle, “Effects of climate change and elevated CO₂ on cropping systems: model predictions at two Italian locations,” *European Journal of Agronomy*, vol. 13, no. 2–3, pp. 179–189, 2000.
- [7] F.-M. Chmielewski and T. Rötzer, “Annual and spatial variability of the beginning of growing season in Europe in relation to air temperature changes,” *Climate Research*, vol. 19, no. 3, pp. 257–264, 2002.
- [8] H. Scheffinger, A. Menzel, E. Koch, and C. Peter, “Trends of spring time frost events and phenological dates in Central Europe,” *Theoretical and Applied Climatology*, vol. 74, no. 1–2, pp. 41–51, 2003.
- [9] V. Potop, P. Zahradníček, L. Türkott, P. Štěpánek, and J. Soukup, “Risk occurrences of damaging frosts during the growing season of vegetables in the Elbe River lowland, the Czech Republic,” *Natural Hazards*, vol. 71, no. 1, pp. 1–19, 2014.
- [10] F.-M. Chmielewski, A. Müller, and E. Bruns, “Climate changes and trends in phenology of fruit trees and field crops in Germany, 1961–2000,” *Agricultural and Forest Meteorology*, vol. 121, no. 1–2, pp. 69–78, 2004.
- [11] D. Tomasi, G. V. Jones, M. Giust, L. Lovat, and F. Gaiotti, “Grapevine phenology and climate change: relationships and trends in the Veneto Region of Italy for 1964–2009,” *American Journal of Enology and Viticulture*, vol. 62, no. 3, pp. 329–339, 2011.
- [12] G. Koufos, T. Mavromatis, S. Koundouras, N. M. Fyllas, and G. V. Jones, “Viticulture-climate relationships in Greece: the impacts of recent climate trends on harvest date variation,” *International Journal of Climatology*, vol. 34, no. 5, pp. 1445–1459, 2014.
- [13] M. Trnka, J. Eitzinger, P. Hlavinka et al., “Climate-driven changes of production regions in Central Europe,” *Plant, Soil and Environment*, vol. 55, no. 6, pp. 257–266, 2009.
- [14] V. Potopová, P. Štěpánek, M. Možný, L. Türkott, and J. Soukup, “Performance of the standardised precipitation evapotranspiration index at various lags for agricultural drought risk assessment in the Czech Republic,” *Agricultural and Forest Meteorology*, vol. 202, pp. 26–38, 2015.
- [15] P. Štěpánek, P. Zahradníček, R. Brázdil, and R. Tolasz, *Methodology of Data Quality Control and Homogenization of Time Series in Climatology*, Český Hydrometeorologický Ústav, Prague, Czech, 2011.
- [16] WMO, “Definition of agrometeorological information required for vegetable crops,” Tech. Rep. WMO-No. 866, World Meteorological Organization, Geneva, Switzerland, 1997.
- [17] E. Pekárková, *Cultivate Tomatoes, Peppers and Other Fruit Vegetables*, Grada Publishing, 2001, (Czech).
- [18] K. Petříková and I. Malý, *Fundamentals of Growing Fruit Vegetables*, Institute of Agricultural and Food Information, Prague, Czech Republic, 2003, (Czech).
- [19] IPCC, *Climate Change 2007: The Physical Science Basis. Contribution of Working Group I to the IPCC Fourth Assessment Report*, Cambridge University Press, Cambridge, UK, 2007.
- [20] M. Déqué, C. Drevet, A. Braun, and D. Cariolle, “The ARPEGE/IFS atmosphere model: a contribution to the French community climate modelling,” *Climate Dynamics*, vol. 10, no. 4–5, pp. 249–266, 1994.
- [21] E. Roeckner, G. Bäuml, L. Bonaventura et al., “The Atmospheric General Circulation Model ECHAM 5. part I: model description,” MPI Report 349, Max Planck Institute for Meteorology, Hamburg, Germany, 2003.
- [22] F. Giorgi, M. R. Marinucci, and G. T. Bates, “Development of a second-generation regional climate model (RegCM2). Part I. Boundary-layer and radiative transfer processes,” *Monthly Weather Review*, vol. 121, no. 10, pp. 2794–2813, 1993.
- [23] F. Giorgi, X. Bi, and J. S. Pal, “Means, trends and interannual variability in a regional climate change experiment over Europe. Part I: present day climate (1961–1990),” *Climate Dynamics*, vol. 22, no. 6–7, pp. 733–756, 2004.
- [24] J. S. Pal, F. Giorgi, and X. Bi, “Consistency of recent European summer precipitation trends and extremes with future regional climate projections,” *Geophysical Research Letters*, vol. 31, no. 13, Article ID L13202, 2004.
- [25] T. Halenka, J. Kalvová, Z. Chládková, A. Demeterová, K. Zemánková, and M. Belda, “On the capability of RegCM to capture extremes in long term regional climate simulation—comparison with the observations for Czech Republic,” *Theoretical and Applied Climatology*, vol. 86, no. 1–4, pp. 125–145, 2006.
- [26] R. Huth, J. Kyselý, L. Pokorná et al., “One month-long integrations of the Aladin model in the climate mode: effect of selected parameters,” *Meteorological Bulletin*, vol. 57, pp. 41–46, 2004 (Czech).
- [27] E. Holtanová, J. Mikšovský, J. Kalvová, P. Pišoft, and M. Motl, “Performance of ENSEMBLES regional climate models over Central Europe using various metrics,” *Theoretical and Applied Climatology*, vol. 108, no. 3–4, pp. 463–470, 2012.
- [28] M. Déqué, “Frequency of precipitation and temperature extremes over France in an anthropogenic scenario: model results and statistical correction according to observed values,” *Global and Planetary Change*, vol. 57, no. 1–2, pp. 16–26, 2007.
- [29] A. Menzel, G. Jakobi, R. Ahas, H. Scheffinger, and N. Estrella, “Variations of the climatological growing season (1951–2000) in Germany compared with other countries,” *International Journal of Climatology*, vol. 23, no. 7, pp. 793–812, 2003.
- [30] M. A. White, P. E. Thornton, and S. W. Running, “A continental phenology model for monitoring vegetation responses to inter-annual climatic variability,” *Global Biogeochemical Cycles*, vol. 11, no. 2, pp. 217–234, 1997.

- [31] T. R. Carter, "Changes in the thermal growing season in Nordic countries during the past century and prospects for the future," *Agricultural and Food Science in Finland*, vol. 7, no. 2, pp. 161–179, 1998.
- [32] P. L. Frich, L. V. Alexander, P. Della-Marta et al., "Observed coherent changes in climatic extremes during the second half of the twentieth century," *Climate Research*, vol. 19, no. 3, pp. 193–212, 2002.
- [33] S. Feng and Q. Hu, "Changes in agro-meteorological indicators in the contiguous United States: 1951–2000," *Theoretical and Applied Climatology*, vol. 78, no. 4, pp. 247–264, 2004.
- [34] H. W. Linderholm, A. Walther, and D. Chen, "Twentieth-century trends in the thermal growing season in the Greater Baltic Area," *Climatic Change*, vol. 87, no. 3–4, pp. 405–419, 2008.
- [35] S. J. Jeong, C. H. Ho, H. J. Gim, and M. E. Brown, "Phenology shifts at start vs. end of growing season in temperate vegetation over the Northern Hemisphere for the period 1982–2008," *Global Change Biology*, vol. 17, no. 7, pp. 2385–2399, 2011.
- [36] X. Yang, Z. Tian, and B. Chen, "Thermal growing season trends in east China, with emphasis on urbanization effects," *International Journal of Climatology*, vol. 33, no. 10, pp. 2402–2412, 2013.
- [37] R. Tolasz, *Climate Atlas of Czechia*, ČHMÚ, Univerzita Palackého v Olomouci, Praha-Olomouc, 2007.
- [38] S. S. P. Shen, H. Yin, K. Cannon, A. Howard, S. Chetner, and T. R. Karl, "Temporal and spatial changes of the agroclimate in Alberta, Canada, from 1901 to 2002," *Journal of Applied Meteorology*, vol. 44, no. 7, pp. 1090–1105, 2005.
- [39] H. S. Lehtonen, R. P. Rotter, T. I. Palosuo et al., "A modelling framework for assessing adaptive management options of Finnish agrifood systems to climate change," *Journal of Agricultural Science*, vol. 2, no. 2, pp. 3–16, 2010.